POLITECNICO DI TORINO

M.Sc. in Biomedical Engineering

DEPARTMENT OF ELECTRONICS AND TELECOMMUNICATIONS

Design of a Near Infrared Spectroscopy Microcontroller Based Data Logger for Cerebral Autoregulation Monitoring

---

Master's candidate:

Umberto DEUT

Supervisor:

Prof. Marco KNAFLITZ

december 2018

Abstract

In the biomedical field there is the need of providing physicians with quantitative information in a fast and reliable way for patients diagnosis and follow-up, preferring real-time, non-invasive, non-ionizing, portable and low cost techniques, when possible. Near Infrared Spectroscopy (NIRS) presents all of these advantages and is mostly used to monitor cerebral autoregulation and muscle oxidative metabolism: its applications continue to broaden as multi-channel and portable devices have permitted to deepen the exploration of physiological phenomena and obtain better temporal and spatial resolution with long duration acquisitions; in the future it is expected that NIRS devices will have a key role in brain computer interfaces and diagnostic purposes. This thesis focused on designing a portable and compact NIRS data logger that exploits a low power architecture to monitor cerebral changes in oxygenated and deoxygenated haemoglobin concentrations during different conditions and tasks. The hardware is composed by two probes, one with the IR emitting LEDs and one with the receiving photodiode, and their 3D printed container, realized in flexible resin in order to adapt to the forehead surface. The firmware was developed at first in the MATLAB environment, using the NIMAX USB-6002 DAQ to generate the impulse signals to control the LEDs lighting, and to acquire the voltage signal from the photodiode, which is used to solve the modified Lambert-Beer equation. Then the ATxmega128A1U microcontroller was programmed with the aim of starting the NIRS acquisition and storing voltage data on microSD card or sending them via USB.

Both the first and the second application were tested on subjects performing apnoea and hyperventilation tasks: the MATLAB project has been useful to confirm that the current given to the LEDs was enough to have a good SNR, and to verify the expected biological response to the related stimuli. Then the microcontroller system has been used later in the same conditions comparing the results with the one obtained previously. In both cases the changes in oxygenated and deoxygenated

haemoglobin concentration were satisfying and in compliance with the results already present in the literature. The device was thought as battery-powered: at present, a prototype has been realized with the available evaluation board, but it may be easily converted into a wearable tool in the future, in order to improve its versatility.

to my family

Acknowledgements

I would first like to thank my thesis supervisor Marco Knaflitz of the department of Electronics and Telecommunications at Politecnico di Torino, he consistently assisted me during my work, always with patience, expertise and comprehension even when I faced with complications always steering me in the right direction.

I would also like to thank my project colleague and friend Stefania Massetti with whom I pursued this important objective, without her participation and support, this thesis could not have been successfully completed.

Finally, I must express my very profound gratitude to my parents, to my girlfriend Giulia and to my friends for their unfailing support and encouragement throughout my years of study and through the process of writing this thesis. This accomplishment would not have been possible without them. Thank you.

Umberto Deut

Turin, December 2018

Contents

List of Figures

List of Tables

Chapter 1

Introduction

1.1 Cerebral Physiology

The brain receives almost the 12–15% of the cardiac output in the adult in resting conditions, even though the cerebral mass represents only the 2% of the whole body mass: a continuous provision of oxygen and nutrients is in fact necessary to permit the accomplishment of the brain complex duties [34]. For maintaining a state of consciousness, a good blood perfusion and consequently an adequate oxygen and glucose delivery is fundamental, as the brain almost does not have glucose storage, but relies mostly on aerobic metabolism to produce energy. For this reason the brain is very sensitive to reduction in cerebral blood flow (CBF) and loss of consciousness occurs within seconds of ischaemia, getting permanently damaged in 3-8 min [27].

1.1.1 Cerebral blood delivery

The ensemble of arterial vessels that bring blood to the brain is called the Circle of Willis and has a configuration that permits a collateral circulation in case of flow reduction in a determinate area (figure 1.1). This circulus arteriosus is located at the base of the brain (eye level) and is created by the junction of the two internal carotid arteries with the two vertebral arteries, enabling blood diffusion in both hemispheres. The bloodstreams from these vessels come together in the posterior communicating artery, where the pressure is equal thus avoiding the mixture. The

safety function of the Circle of Willis raises in case of occlusion of the internal carotid artery or the vertebral artery, since the blood changes its way across that point, forward or backward, and this collateral circulation helps in case of reduced flow. Such a condition may happen after a stroke, which threatens blood flow to the brain [36].

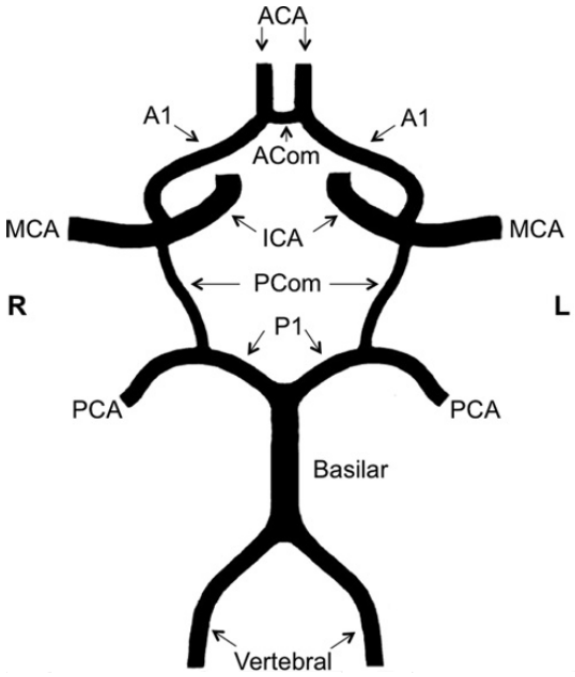

Figure 1.1: Circle of Willis: Pcom = posterior communicating artery; Acom = anterior communicating artery; ACA = anterior cerebral artery; ICA = internal carotid artery; A1 = the first segment of the ACA (between the ICA and the ACom); MCA = middle cerebral artery; PCA = posterior communicating artery; basilar = basilar artery; P1 = the first segment of the PCA (between the basilar and the PCom); vertebral = vertebral artery; L = left; R = right. [8]

The volume of blood in the whole brain is differently distributed between the gray and the white matter: the first one is mainly made by the cell bodies of the neurons, while the second one is composed by their axons. Since the most complex functions are carried out in the gray matter, the majority of the blood flow is directed there.

1.1.2 Cerebral Metabolism

The brain high needs for blood supply reflect in his metabolic consumption which represents the 20% of basal oxygen consumption (50 ml min^{-1}), at rest. Cerebral metabolic rate of oxygen can be calculated as:

$$CMRO_2 = CBF * (A - V)O_2 \tag{1.1}$$

where $(A - V)O_2$ means difference content of O_2 between cerebral arteries and veins. The gray matter, as expected, requires five times the consumption of oxygen than the white matter, and CBF is modified to meet these needs.

Physiological Parameters	Gray Matter	White Matter	Brain Average
CBV (ml/100 g)	4–6	1.5–2.5	3.5–4.5
CBF (ml/100 g/min)	100–110	20–25	45–55
CMRO2 (ml/100 g/min)	4–4.5	0.7–1.0	3–3.5
CMRglu (mg/100 g/min)	6.5–8.5	1.2–2.2	4–5

Table 1.1: Healthy subjects' mean values [34]

Glucose is a fundamental molecule for the brain since the energy produced by its conversion in ATP permits both brain activities (60% of the energy produced) and the homeostasis of the cells (40%) [20]. Under aerobic metabolism from one molecule of glucose 38 ATP are obtained with respect to two ATP molecules under anaerobic conditions; it is clear that aerobic metabolism must be re-established as soon as possible otherwise permanent damages to the cells occur. Table 1.1 shows average values of cerebral blood flow, volume and metabolic demands in adults. A number of vasoactive mediators (hydrogen ions, potassium, CO_2, adenosine, glycolytic intermediates, phospholipid metabolites and especially nitric oxide) is able to change CBF within seconds in order to face local metabolic demands, in fact higher CBF guarantees higher substrate delivery, and vice versa: the so called *flow-metabolism coupling* (figure 1.2).

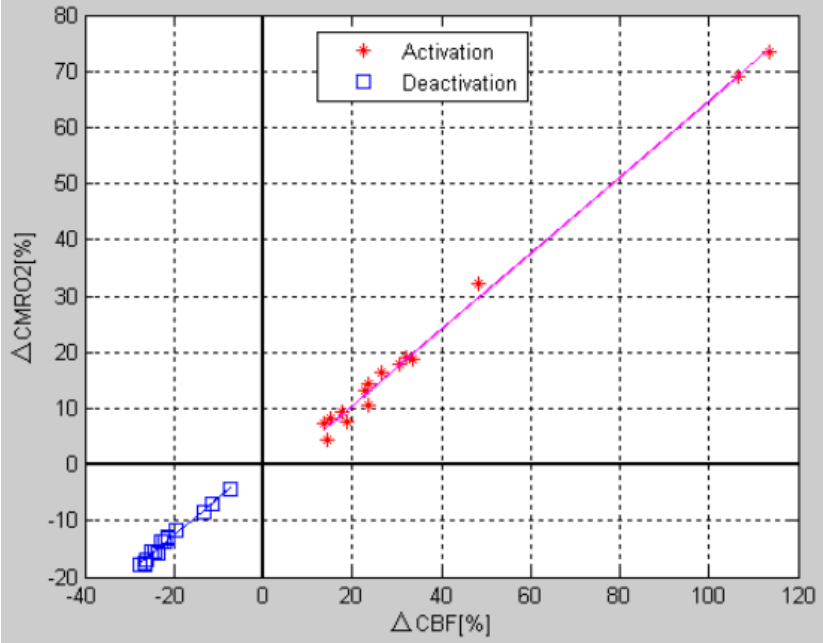

Figure 1.2: CBF coupling with $CMRO_2$: linear relationship during both activation and deactivation, with $CMRO_2$/CBF coupling ratios of 0.68 $\pm$ 0.02 for activation and 0.66 $\pm$ 0.03 for deactivation, thus not significantly different [16].

1.1.3 Cerebral blood flow

Hagen-Poiseuille equation describes the cerebral blood flow in case of laminar flow (corresponding to a non pathological condition in human body):

$$CBF = \frac{\pi \Delta P r^4}{8 \mu l} \tag{1.2}$$

where r and l are the calibre and the length of blood vessel, μ the dynamic viscosity of blood and ΔP is a pressure gradient called cerebral perfusion pressure (CPP). The radius of the vessels determines the cerebrovascular resistance, which is reduced in case of vasodilatation and increased in vasoconstriction, leading to an opposite behaviour of the CBF.

The perfusion pressure derives from the difference between arterial and venous circulatory pressure, and directs the blood to each organ; nevertheless, to define CPP, also the intracranial pressure (ICP) must be considered:

$$CPP = MAP - (CVP + ICP) \tag{1.3}$$

where MAP is the mean arterial pressure, CVP the central venous pressure. Typical values of CPP in adults ranges between 70 and 90 mmHg and CBF remains constant. CPP falls in case of blood losses, since hypotension reduces MAP and CPP: hence shocked patients show a decreased level of consciousness. An intracerebral haematoma would have the same effect as it increases ICP; when both conditions co-exist an high risk of brain ischaemia impend. An increase in CPP is usually the result of an increase in MAP, since the contribution brought by reducing ICP is minimal especially in the upright position, when CVP and ICP are negative at brain level so less relevant (see the further explanation of ICP in the section below).

Intracranial Pressure and its control

Inside the skull, pressure must be maintained almost constant to avoid brain compression: as in the hypotesis of Monro-Kellie [21] the whole volume of the brain plus the blood and the cerebrospinal fluid (CSF) [1] can not change. These three elements contributes in different ways to the total volume:

- brain volume 85%
- CSF 10% (150 ml)
- blood 5% (50–75 ml).

ICP range goes from 5 to 15 mmHg in normal conditions and supine position, decreasing in the upright one. The first consequence when ICP increases is a reduced CPP, then local compression and, in extreme conditions, herniation of brain tissues can arise [34].
The strategy to control ICP is called **volume buffering**, and consists in a fast compensation made by the blood and the CSF in case ICP increases or decreases. Blood carries out this role through a changing of vascular caliber, and this is the most effective mechanism as it is a very rapid response. For what concerns CSF, even

[1] CSF is an extracellular fluid produced mainly by the choroid plexus and re absorbed by the arachnoid granulations into the venous circulation. It is located in between the arachnoid and pia mater and also in the ventricles, with the function of providing buoyancy to the brain.

though its rate of production is constant (0.3–0.4 $mlmin^{-1}$), it can perform a spatial compensation being moved to the spinal canal when ICP increases. On the other side, if ICP decreases, hampering CSF outflow causes ICP to rise. Once the compensation mechanism reaches its limit, it can not contrast the effects of an intracranial pathology anymore: for instance, an haematoma or a brain swelling would lead to a marked increase in ICP with consequent lowering in CPP and cerebral ischaemia (figure 1.3).

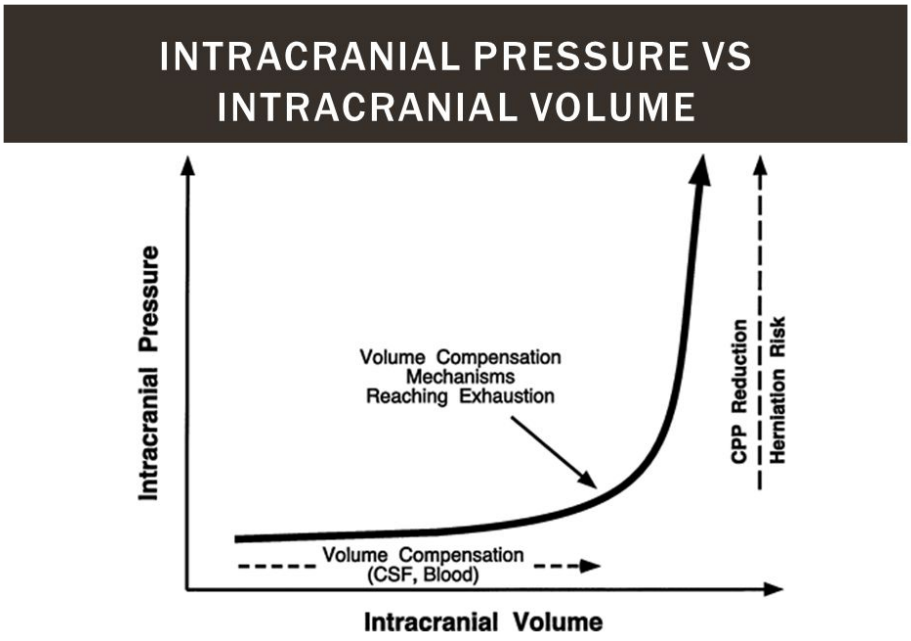

Figure 1.3: ICP volume compliance curve. ICP remains nearly constant with increase in intracranial volume (little $\Delta V/\Delta P$) until volume buffers are exhausted, then it increases rapidly with increasing intracranial volume [13].

1.1.4 Autoregulation mechanism

Autoregulation of blood flow is defined as the ability of an organ or a vascular bed to keep perfusion stable as blood pressure changes, a mechanism that can be explained as an almost instantaneous myogenic adaptation (within 1-10 s) whereby a variation in vascular resistance happens due to a changing in perfusion pressure. In a normal brain cerebral blood flow remains constant over a pressure range between 60 and

150 mmHg, above and below CBF changes directly with MAP. Autoregulation limits may be modulated by various factors like sympathetic and parasympathetic nervous activity, the vascular renin-angiotensin system and changes in arterial oxygen and carbon dioxide tension.

Neurological control of CBF is made by a chemical release of neurogenic mediators to cerebral vasculature through the postganglionic sympathetic nerve supply from the superior cervical ganglion, which contains norepinephrine and neuropeptide, and parasympathetic innervation from the sphenopalatine and the otic ganglia, containing acetylcholine and vasoactive intestinal peptide (figure 1.4). The first two factors, in case of excessive sympathetic activity, shift the $\frac{CBF}{CPP}$ curve (the green one in figure 1.5) to the right (chronic hypertensive states), while the last two, in case of excessive parasympathetic activity, lead to vasodilatation (hypotensive states). Baroreceptors located in the carotids and aortic arch are responsive to changes in MAP: for higher MAP they increase their action potential firing rate to the brain, saturating at 160 mmHg, for lower MAP they diminish this frequency until pressure goes under 60 mmHg, when they stop firing.

Baroreceptors are very sensitive to fast variations in MAP, while in case of long lasting high or low values they re-adapt the firing rate to normal values (*receptor resetting*).

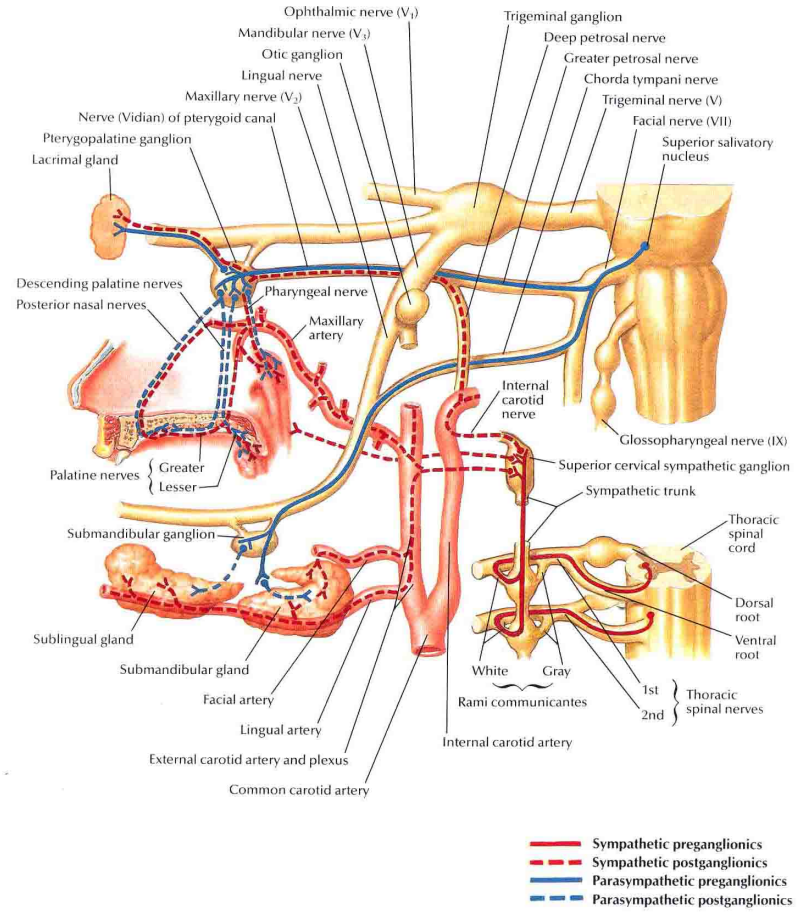

Figure 1.4: Sympathetic and Parasympathetic innervation controlling smooth vascular muscles [6].

As shown in figure 1.5, **arterial carbon dioxide tension** is related to CBF variations since it causes vasodilatation and vasoconstriction: the relationship is linear in a range between 2.7-10.5 kPa (20-80 mmHg), with a slope ΔCBF/Δ Pa_{CO2}= 11–15 ml/100 g/min/kPa. After CBF has doubled, the upper plateau is reached and arterioles can not increase anymore their radius, while after it has halved the lower plateau is reached and possible ischaemia can follow. Those reactions are very fast, arriving to the plateau phases in almost 12 min (in both directions). The gray matter is more affected by Pa_{CO2} alterations, because H^+ ions concentration is modified in the interstitial zone between the blood-brain barrier and gray matter itself, causing vessels to expand. It is remarkable that in case of hyperventilation, the decrease of Pa_{CO2} to 2.7 kPa determines a decrease in CBV of about 10 ml, which may be considered as a way to lower ICP when needed, but once again the risk of ischaemia

would be serious.

For what concerns **arterial oxygen pressure**, when Pa_{O2} goes under 6.7 kPa (50 mmHg), hypoxia is acknowledged by oxygen-sensitive ion channels and vascular smooth muscles dilate as a consequence of the action of vasoactive substances (e.g. angiotensin and vasopressin). As visible from the curve in figure 1.5, vasoconstriction at higher values of Pa_{O2} is not relevant. Chemoreceptors, also located in the carotid sinus and aortic arch as the baroreceptors (figure 1.6), respond to hypoxia and hypercapnia to activate the vessels compensation.

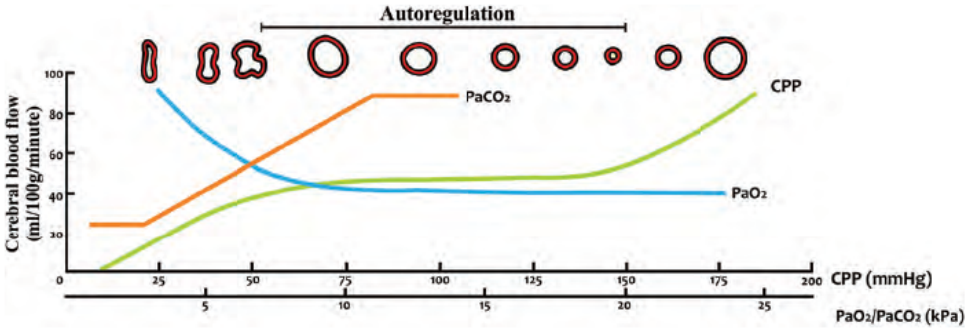

Figure 1.5: Cerebral blood flow regulation factors [31].

A number of brain disease states may impair or abolish CBF autoregulation: severe head injury or acute ischemic stroke for instance, or in neonatal brain asphyxia and infections of the central nervous system. Likewise, autoregulation may be compromised in the surroundings of a brain lesion (tumor or hematoma) and in long-term diabetes mellitus, because of diabetic microangiopathy. The necessity of quantifying cerebral hemodynamic variations with high temporal resolution paved the way to the technique called Near Infrared Spectroscopy.

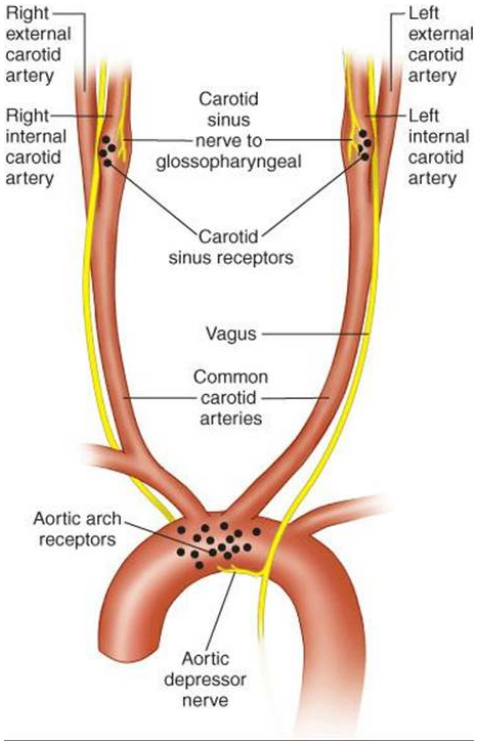

Figure 1.6: Baroreceptors and Chemoreceptors situ [7].

1.2 Thesis purpose

The aim of the thesis consisted in the design of a portable and compact NIRS data logger that exploits a low power architecture to monitor cerebral changes in oxygenated and deoxygenated haemoglobin concentrations during different conditions and tasks. At present the first steps towards the complete device have been made, realizing a prototype with the available evaluation board: in the near future it will be easily converted into a wearable tool adding a battery power supply, in order to improve its versatility. The next chapters will introduce a brief review of the NIRS state of the art, then hardware and software design will be explained and the final results obtained will be presented.

Chapter 2

Near Infrared Spectroscopy

2.1 State of the Art

Biomedical imaging techniques are an improving technology for what concerns diagnosis and follow-up of patients. Nowadays a number of techniques have been developed to be real-time but also non-invasive, non-ionizing, portable and low cost, providing physicians with quantitative information in a fast and reliable way. Near Infrared Spectroscopy (**NIRS**) presents all of these advantages and in the biomedical field it is mostly used to monitor hemodynamic and oxigenation level of various tissues using light in the range of 650-950 nm, exploiting its property of penetrating a few centimeters inside soft tissues, being less affected by absorption and scattering: therefore this range of wavelengths is called tissue optical window.

Cerebral autoregulation is one of the biological mechanisms that can be monitored exploiting NIRS: from the extracted signals important parameters such as tissue oxygenation index[1] in a resting state can be retrieved, as well as oxy and deoxy-hemoglobin changes in concentration ($\Delta[O_2\text{Hb}]$ and $\Delta[\text{HHb}]$) in the cortex in response to a wide range of stimuli (e.g. apnoea or stroop test), thus detecting variations in blood hemoglobin composition associated with neural activity. NIRS technique is limited to a **surface investigation**, nevertheless the possibility of studying CBF in the gray matter is pertinent since most of the functions are accomplished there, as already explained (see section 1.1.1).

[1] TOI, calculated as the ratio of oxygenated to total haemoglobin

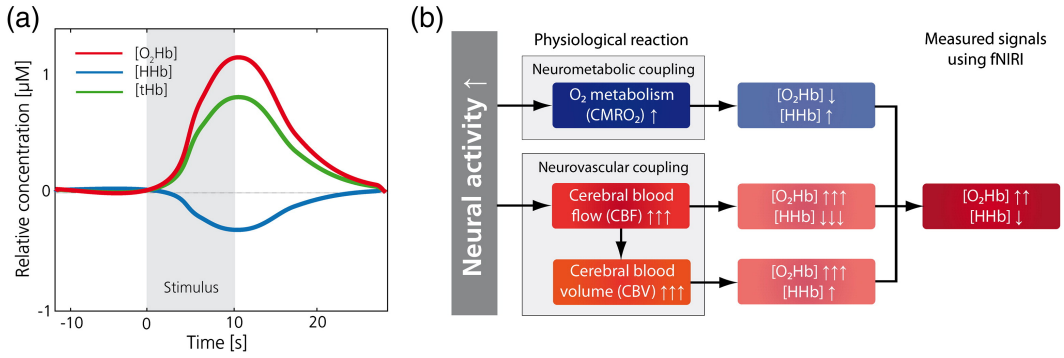

Figure 2.1: a) Usual variations in [O2Hb], [HHb] and [tHb] (total hemoglobin concentration) signals due to brain activity. (b) Hemodynamic and oxygenation changes in response to cerebral activity [29].

In 1977 Jobsis [12] stated for the first time that spectroscopy could be used to quantify oxygen saturation in myocardial and brain tissues, thanks to their relative transparency in near-infrared spectrum. Jobsis discoveries opened the way for the clinical application of NIRS to investigate cerebral oxygenation and muscle oxidative metabolism; nowadays quantitative thresholds on cerebral oxygenation allow to identify cerebral ischaemia and NIRS imaging (NIRI) is used for brain mapping [11] and muscle pathologies [1]. Since 1993 also functional activation in human adult [35] and newborns [19] cortex was studied with the **fNIRS** technique. Traditionally two different wavelengths were used to acquire $\Delta[O_2Hb]$ and Δ[HHb] signals, but also cytochrome-c-oxidase redox state (Δ[CtOx]) has recently gained clinical relevance. This third chromophore is placed inside the mitochondria and plays the role of terminal electron acceptor in the mitochondrial respiratory chain that brings to the production of ATP in the aerobic synthesis [26], consequently CtOx is a biomarker of the cerebral metabolic status. Moreover it has been demonstrated that Δ[CtOx] has higher brain-specificity than traditional haemoglobin indicators when there is a change in cerebral oxygen delivery. This is due to the higher presence of mithocondria in this tissue than in skin or skull: in particular an increasing amplitude of the Δ[CtOx] signal has been noticed with deeper light penetration, a behaviour not shown by the haemoglobin chromophores and observed using multiple source-detector distances, allowing investigation at multiple depths [15]. This kind of studies strengthened trust in exploiting this signal as a brain-specific biomarker

while previously, in presence of considerable higher concentrations of haemoglobin, the interference of the other chromophores made Δ[CtOx] measurement very difficult.

2.2 Mathematical Methods

As already said, near-infrared means adopting light in the 650-950 nm range where the relevant chromophores absorb more than water and lipids (figure 2.2) and moreover the different peak of absorption between O_2Hb and HHb gives the possibility of addressing them singularly using the proper wavelength; anyhow an issue that must be taken into account is light scattering inside tissue. The first mathematical method developed to quantify Δ[chromophores] is the **differential path-length factor method**: it uses the modified Lambert-Beer equation and permits to measure changes in chromophore concentration but not their absolute values [5]. The equation gives the light attenuation (A) in optical density (OD):

$$A = -log(I/Io) = Bd\alpha c + G \tag{2.1}$$

where Io is the incident light intensity, I is the transmitted light intensity, α is the extinction coefficient, c the chromophore concentration, B is the differential path-length factor that takes into account the additional absorption due to an increased optical path, d the distance between light emitter and receiver (Bd = differential path), G a value that accounts for scattering losses [4].
The differential path-length factor (DPF) must be found in the literature [9] or measured dividing the absolute pathlength (d_a) travelled by light for the distance emitter-detector: to calculate d_a the first possibility is to use ultra-short light pulses coupled with a fast optical detector (TRS, time resolved spectroscopy) [4]:

$$d_a = \frac{ct}{n} \tag{2.2}$$

where c is the speed of light, t is the mean time of flight, n is the refractive index of the tissue. A time resolution of 10 picoseconds of the camera means 2.14 mm of spatial resolution in the tissue [4]. The second possibility exploits a radiofrequency

modulated light source and evaluates the phase shift of the transmitted light (PMS, phase modulation spectroscopy) [3]:

$$d_a = \frac{\phi c}{2\pi f n} \tag{2.3}$$

with ϕ representing the phase shift and f the modulation frequency. It has been demonstrated that, for a given tissue, the DPF is constant if the distance between light emitter and receiver is above 2.5 cm [4] and the distance calculated by phase or mean time correlates below 200 MHz (see section 2.2.1 for further explanation). For what concerns G, this is an unknown term so, with this type of mathematical model, only ΔA can be retrieved, and consequently the measured changes in light attenuation are assumed to be the changes in the chromophore concentration:

$$\Delta A = Bd\alpha\Delta c \tag{2.4}$$

Of course, in case $\Delta[O_2\text{Hb}]$ and Δ[HHb] need to be measured, the above equation must be modified to obtain the following system of equations, in which two wavelengths are necessary to find the solution:

$$\begin{cases} \Delta A_{\lambda 1} = Bd\alpha_{\lambda 1}^{O2Hb}\Delta c_{\lambda 1}^{O2Hb} + Bd\alpha_{\lambda 1}^{HHb}\Delta c_{\lambda 1}^{HHb} \\ \Delta A_{\lambda 2} = Bd\alpha_{\lambda 2}^{O2Hb}\Delta c_{\lambda 2}^{O2Hb} + Bd\alpha_{\lambda 2}^{HHb}\Delta c_{\lambda 2}^{HHb} \end{cases} \tag{2.5}$$

From equation 2.5 it is clear that the geometry and the composition of the tissue must remain constant (the DPF method makes the assumption of tissue homogeneity), otherwise they will cause variations in light absorption that will wrongly be interpreted as chromophore concentration changes: this may happen in case of motion artifacts.

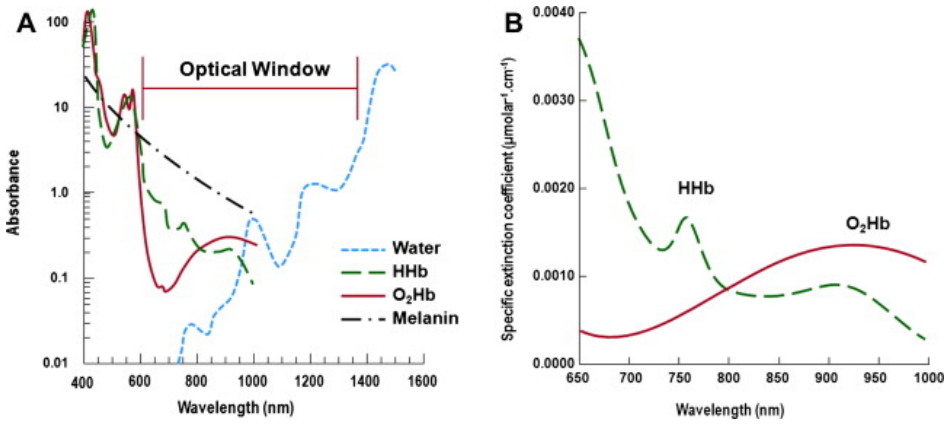

Figure 2.2: LEFT: Main absorbers in the 400-1400 nm range, with the "optical window" between 600 and 1000 nm, adapt for NIRS researches [23]. RIGHT: extinction coefficients of O_2Hb and HHb for different wavelengths.

2.2.1 Techniques

Near infrared spectroscopy measurements can be obtained exploiting various methods that differs from each other in accuracy or number of parameters obtained. At first the most widely used approach was the Continuous Wave Technique, or **CW NIRS**, that measures only variations in light intensity relying on the DPF method (figure 2.4a). The number of wavelength needed are at least as much as the number of chromophores investigated, but using more wavelengths increases the accuracy of the system. The devices commercially available adopt four wavelengths at most and the light sources are usually semiconductor laser diodes. The detector can be a photomultiplier, convenient for its low noise, or a silicon photodiode, which has a small size and high quantum efficiency (see section 3.1).

An advantage of this technique consists in its cheapness and the possibility of miniaturization. Moreover if more emitter-receiver couples are distributed on the tissue, the chromophores changes in relative concentration can be monitored in more areas, in order to create images: this type of setting are exploited in the functional NIRS devices. For what concerns the disadvantages, as already explained in section 2.2, the main problem is that CW NIRS cannot calculate tissue optical properties like light scattering and absorption coefficients, so absolute concentrations can not be retrieved; moreover this type of technique is very sensitive to motion artifacts, since

it pretends that DPF factor and light scattering remain constant, so that changes in absorption are only due to the chromophores.

As hinted in section 2.1, another technique is the Spatially Resolved Spectroscopy (**SRS**) or multi-distance spectroscopy: it uses more than one light detector to measure light intensity at different distances from the source [10] (figure 2.3). The innovative characteristic of SRS technique consists in its assumption of having the same optode-tissue[2] coupling for all the given source-detector distances and, calculating the light intensity a function of the distance, it can determine the ratio of O_2Hb to total hemoglobin and thus tissue oxygen saturation [23], that is a useful parameter when related to arterial diseases.

Then there is the Time Resolved Spectroscopy or time domain spectroscopy: it uses an approach based on the time of flight measurement. The method consists in the typical emission of a 100 ps pulse of light through the tissue and the subsequent calculation of the time point spread function once the light has been transmitted. The light pulse is divided into two rays: one goes through the tissue, the other one goes to a camera to create a temporal reference, then the difference in time between the light entering and exiting the tissue is used to calculate the DPF, as already explained in section 2.2. Two processes affect this function: the first is the scattering, which makes the pulse spread, the second is the absorption, which instead diminishes the intensity of the light (figure 2.4 C).

[2] An optode is defined as an optical sensor device that can measure a specific substance.

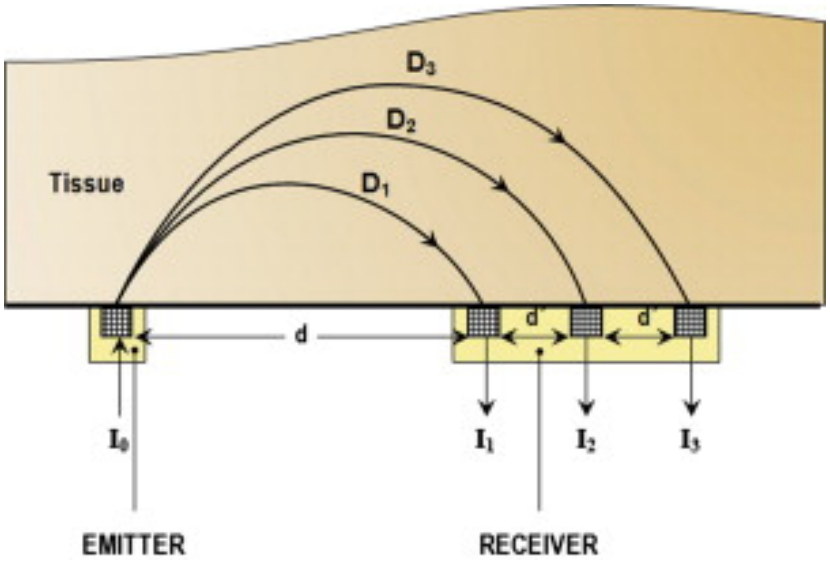

Figure 2.3: Scheme of a multi-distance NIRS system, which gives the opportunity of addressing different and deeper levels of brain cortex [23].

The advantage in adopting this type of technique is represented by the possibility of calculating the absolute values of chromophores concentration: an histogram is created with the number of photons on the y axis and the time of flight on the x axis, so it gives information about the depth traveled by each photon. From the absorption and scattering coefficients calculated, the absolute concentration values can be obtained. The disadvantage of the TRS is that it needs expensive instrumentation that works in photon counting mode, that makes it very sensitive but also quite affected by noise. The size of the instrumentation is also a problem in clinical applications; in the future miniaturization will definitely improve the employment of the TRS technique.

The last one is the Phase Modulation Spectroscopy (**PMS**) or frequency domain spectroscopy: it can be considered as the equivalent of the TRS but acting in the Fourier domain. PMS consists in modulating the intensity of light sources at radio frequencies from 50 MHz to 200 MHz. Once the light has been passed through the tissue, a number of parameters are collected: the mean light intensity, the amplitude, and the emerging wave phase which gives information about the time of flight (figure 2.4b) and consequently permits to calculate the DPF, as seen in section 2.2. The advantage of this kind of instruments with respect to the TRS ones is

their smaller size and better signal-to-noise ratio because they can reveal an higher number of photons. The disadvantages in clinical approaches consist in the use of environment light sensitive photomultiplier tubes.

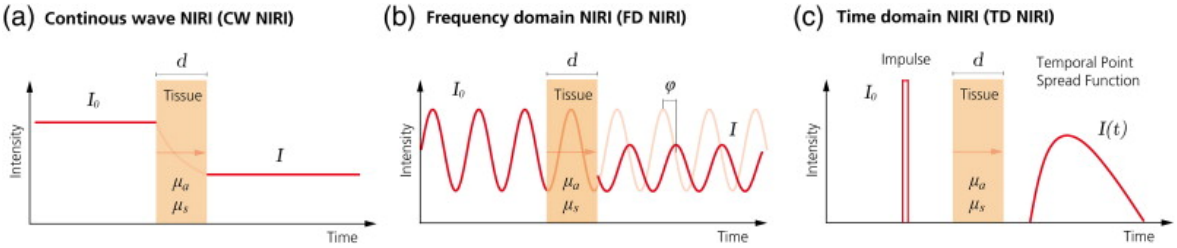

Figure 2.4: The three main methods used in NIRS measurements.
A) The continuous wave technology sends light and measures the changes in the intensity of the light transmitted through the tissue. B) The frequency domain technology modulates the emitted light intensity and then measures intensity of the emerging light as well as its phase shift, that represents the time of flight. C) The time domain technology gives an short pulse of light into the tissue and measures the arrival times of the photons coming from the tissue. (I_0): incident light signal, I: transmitted light signal, d: thickness of the medium, μa: absorption coefficient, μs: scattering coefficient, ϕ: phase delay, I(t): temporal point spread function of the transmitted light signal [29].

The technologies described above are currently the most affirmed ones, but there are others that may become popular in the next years: for example a recent way to derive absolute values of total hemoglobin concentration implies the use of ultrasound waves with optoacoustic spectrometers [2]: they generate short optical pulses and detect the incoming waves with an acoustic transducer, adopting a time-resolved method.

2.3 Available NIRS devices

The first devices released from companies were CW instruments with one channel available, used in clinical applications such as functional brain activity investigations, and able to detect relative changes in chromophores concentration (e.g. *FORESIGHTc* from Casmed, USA, which adopted the multidistance technique). Later also spatially and time resolved methods were exploited to develop new types of

Parameters and instrumentation	CW	SRS CW	PMS	TRS
$[O_2Hb]$, $[HHb]$, $[tHb]$	relative values	absolute values	absolute values	absolute values
Scattering, absorption coefficient and pathlength	no	no	yes	yes
Tissue $[O_2Hb]$ saturation measurement	no	yes	yes	yes
Depth with 4-cm source-detector distance	low	low	deep	low
Sampling rate (Hz)	≤ 100	≤ 6	≤ 100	≤ 6
Instrument size	very small	small	small	medium
Transportability	easy	easy	easy	uneasy
Cost	cheap	moderate high	moderate high	high
Tissue-source contact	critical	not critical	not critical	not critical

Table 2.1: Characteristics of the principal NIRS techniques [37].

devices, with the characteristic of retrieving absolute values of concentration (e.g. *OxiplexTS* from ISS, USA, or *TRS-20* from Hamamatsu, JPN.) This improvement led to a more intensive use of NIRS for monitoring patients during treatments like cardiac and carotid surgery in adults or neonatal medicine. Furthermore, wireless multichannel instruments with multiple emitters and receivers brought the measurements from a single location, assumed as globally representative of the tissue oxygenation, to a whole area covering, giving a better description of the tissue. Researchers are nowadays paving the way towards multifunctional wireless devices which include EEG and multichannel NIRS systems in order to have a more complete description of the cerebral activity with a good temporal resolution, gaining the possibility of studying deeply brain activity during dynamic tasks, such as post-stroke gait rehabilitation [28].

2.4 The technique implemented

Figure 2.5 shows the time-resolved method thought up for this NIRS device: a square wave with default period of 100 ms and duty cycle of 10% is used to light on the LEDs, shifting one signal from the other in order to light up one emitter at a time, and contemporaneously the voltage signal from the photodiode due to the LEDs blinking is sampled. The amplitude of the impulse was fixed at 1.5 V in order to obtain a 45 mA current through the LED; despite this, as expressed later in chapter 6, the possibility to change this parameter was introduced to examine the variation of the signal quality. In every cycle, after 10 ms from the switch off of LED2, the output of the receiver is sampled again and the voltage obtained is used to estimate the noise amplitude used in the calculation of the signal to noise ratio (SNR).

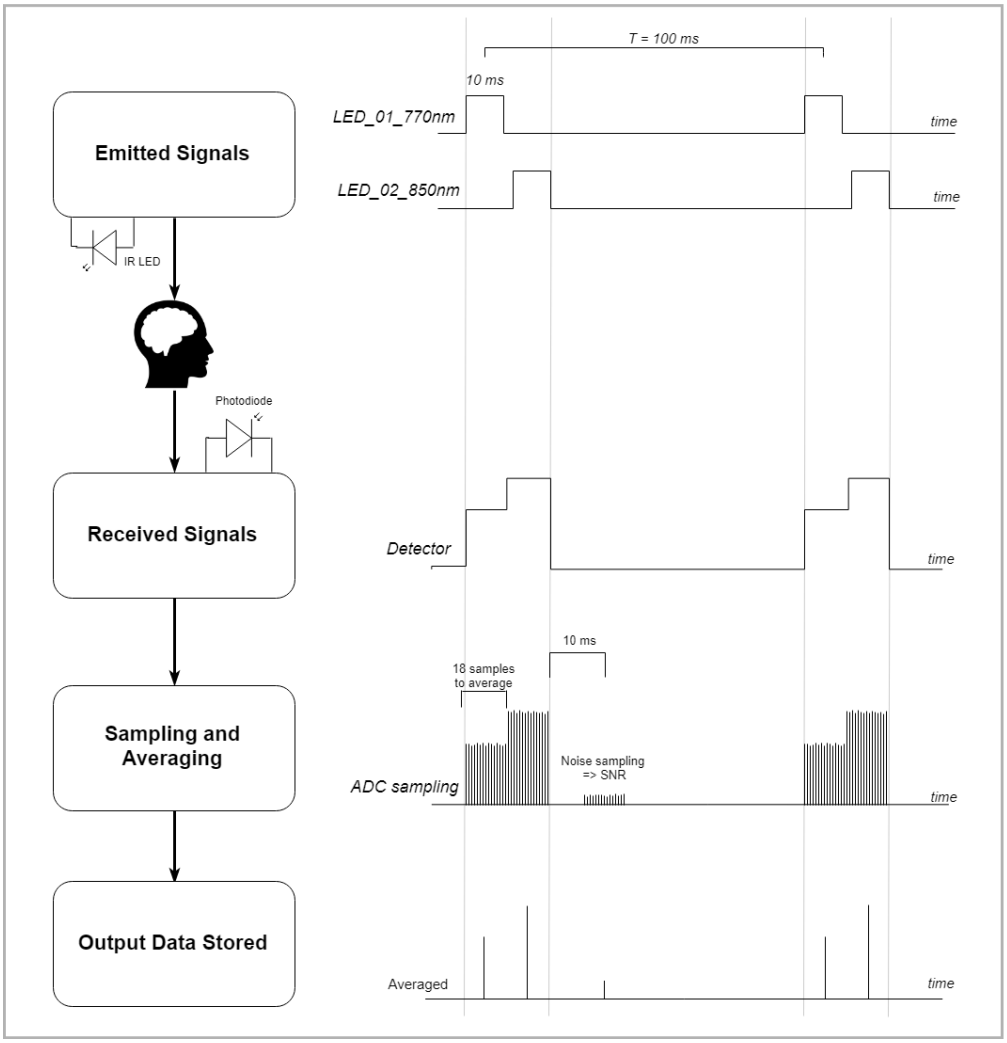

Figure 2.5: Diagram of operation of the implemented technique

Then the Lambert-Beer equations system seen in equation 2.5 is solved to obtain the variations of concentrations:

$$\begin{cases} \Delta[O_2Hb] = -\frac{[(\frac{\alpha_{\lambda1}^{HHb}\cdot\Delta V_{\lambda2}}{DP})-(\frac{\alpha_{\lambda2}^{HHb}\cdot\Delta V_{\lambda1}}{DP})]}{\alpha_{\lambda1}^{HHb}\cdot\alpha_{\lambda2}^{O_2Hb}-\alpha_{\lambda2}^{HHb}\cdot\alpha_{\lambda1}^{O_2Hb}} \\ \Delta[HHb] = -\frac{[(\frac{\alpha_{\lambda1}^{O_2Hb}\cdot\Delta V_{\lambda2}}{DP})-(\frac{\alpha_{\lambda2}^{O_2Hb}\cdot\Delta V_{\lambda1}}{DP})]}{\alpha_{\lambda1}^{O_2Hb}\cdot\alpha_{\lambda2}^{HHb}-\alpha_{\lambda2}^{O_2Hb}\cdot\alpha_{\lambda1}^{HHb}} \end{cases} \tag{2.6}$$

where DP is the differential path found multiplying the source-receiver distance d with the DPF factor; in fact, as previously anticipated in section 2.2, to extract the quantitative information of the concentration changes this factor takes into account the increased distance traveled by light due to the different path that the light travel

under the skin, the so called "banana shape" (figure 2.3). The DPF factor typically varies with the age of the subjects [9]: the range for an adult is between 3 and 5, and in this NIRS device a DPF of 3.5 was chosen. The ΔV value is used as ΔA, since they are proportional between each other, and it is calculated with respect to a reference voltage obtained averaging data in the reference time chosen (default 10 s), as will be explained later in chapter 6. For what concerns the molar extinction coefficients, their values are not standardized and there is not an accepted convention as many groups of researchers have presented their own tabulation: for this device the values presented in table 2.2 have been adopted, taken from [32].

Molar Extinction Coefficients ($cm^{-1}/\mu M$)			
	770nm	830nm	850nm
α_{O2Hb}	650*10^{-6}	974*10^{-6}	1058*10^{-6}
α_{HHb}	1311.88*10^{-6}	693.04*10^{-6}	691.32*10^{-6}

Table 2.2: Molar extinction coefficient used.

The principal advantage of this technique consists in the small energy consumed during the acquisition process since LEDs don't need to stay switched on for all the duration of the recording; moreover the SNR is an useful quantity to evaluate the quality of the signal which is an important aspect to consider during the positioning of the probes.

Chapter 3

Hardware Design

3.1 Probes

The design of the NIRS device started by projecting its hardware: as outlined in section 2.2.1, NIRS systems, from an electrical point of view, basically rely on near-IR light emitters and light detectors. For each of these components there are different possible choices, whose advantages and disadvantages will be presented in the following paragraphs.

3.1.1 NIRS emitter

Two factors must be evaluated when selecting the proper light source in a device of this kind: the need for discrete wavelengths and the need to generate a relevant amount of power through the tissues, without overcoming the heating safety limits due to power dissipation though [29]. The first requisite reflects what has been explained about chromophores absorption spectra and ideally the radiation spectrum of the emitter should be monochromatic. In practise it is expected to be at least very peaked on a precise wavelength with little variance in intensity, as its fluctuations would be considered as changes in the concentration of the chromophores in the tissue under investigation. The second requirement takes under consideration that the more power leaves the emitter the more can be obtained on the detector side, so the loss due to light path should be compensated; moreover in this conditions larger

source-receiver distances could be chosen to explore deeper portions of the tissue. Typically the alternative is among laser diodes (LD) and light emitting diodes (LED), two semiconductor technologies that employ electroluminescence by way of electron-hole recombination in forward biased p-n junctions, emitting light whose wavelength is based on the device material and doping [17]. The main difference between LEDs and LDs is the type of emission, which is spontaneous in LEDs case and only allows for incoherent light with a large bandwidth (typically 25–50 nm), while is stimulated for LDs and gives coherent light with a narrower bandwidth. Anyway the operating range of LDs is limited with respect to the one of LEDs, whose intensity is easily adjustable, and LDs often need relatively large packaging inconvenient for miniaturization challenges; moreover, they can be dangerous for eyes safety and present less variety of wavelengths, limited between 695 nm and 775 nm, with difficulty in finding at a reasonable price a 760 nm emitting laser, a wavelength that represents an absorption peak of HHb. This is a relevant disadvantage of LDs with respect to LEDs, since the selection of the right wavelengths combination may considerably change the quality of the measurements: LEDs gives an higher flexibility from this point of view. Table 3.1 summarizes advantages and disadvantages if these technologies.

Usually LDs are preferred over LEDs in Time Resolved NIRS systems, as the pulse width is of the order of 100 ps and LDs fast response results suitable for this type of application. However in the system developed in this thesis high speed characteristics were not required and LEDs features has been considered good enough for the purpose.

Source Type	Power Range (mW)	Bandwidth (FWHM)	Cost	Size	Speed	Color	Heating
Light emitting diodes	Low to Medium (1 to 30)	30 nm band surrounding nominal color	Cheap	Small	Slower	Many	Lower
Laser diodes	Low to High (1 to >500)	Discrete colors (1 nm)	More expensive	Bulkier	Faster	Limited	Higher

Table 3.1: Principal characteristics of the two light sources exploited in NIRS devices [33],[29].

Three wavelengths have been chosen, that are 770 nm, 830 nm and 850 nm, selected taking into account the absorption spectra of HHb and O_2Hb (see figure 2.2) and of cytchrome c oxidase. The default LEDs pair used in the designed NIRS device is composed by the 770 and 850 nm LEDs, as it permits to separate as much as possible HHb response signal from the one of O_2Hb after a stimulation (see section 7.4.1); even though the system created is at the moment limited to this type of investigation, the 830 nm was added with the aim of creating in a future improvement a more informative system able to control also cytochrome-c-oxidase changes, whose relevance has been explained in section 2.1. In details the infrared LEDs chosen are a 770 nm *OSA Opto Light OIS-330 770* , an 830 nm *Vishay VSMG2700* and an 850 nm *VSMG10850*; from datasheets specifications typical forward voltage were around 1.5 V and the range of forward current at maximum ratings stays between 65 mA and 100 mA. They have been mounted on the circular PCB presented in the figure 3.1 and connected to the mainboard with a 6 conductors cable of 3.3mm diameter.

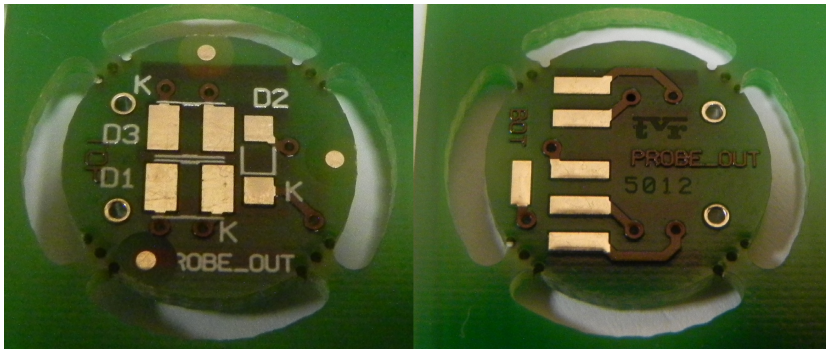

Figure 3.1: Printed circuit board for the LED probe. Left: top view, right: bottom view

3.1.2 NIRS receiver

The photodetectors used in NIRS biomedical studies can be divided into three categories:

- Photomultiplier Tubes (PMT)
- Photodiodes (PD)
- Avalanche Photodiodes (APD)

Those devices rely on external or internal photoelectric effect: PMT are based on the first one, in which a photon frees an electron from the photocathode which, thanks to a strong electric field, is accelerated towards a series of dynodes, with enough kinetic energy to produce several secondary electrons when striking in cascade the dynodes's surface. The final electrical multiplication factor is of about 10^6 to 10^7 [17]. APD and PD exploit instead the internal effect that generates when a semiconductor junction diode absorbs a photon, event that leads to the production of several electron–hole pairs and thus a photo-current corresponding to a measurable electrical signal.

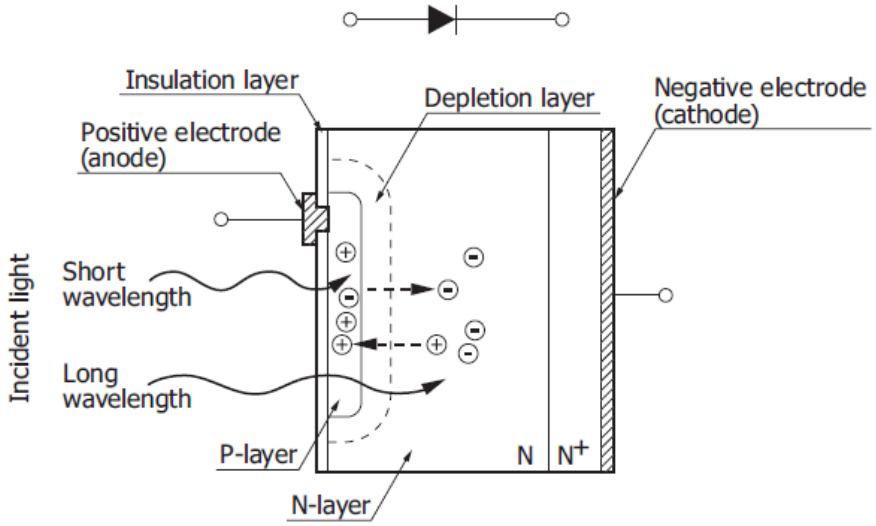

Figure 3.2: Silicon photodiode cross section [25]: a photodiode is created by selective diffusion of impurities (boron or phosphorus) which create two regions that contains electrons (n-layer) and a region that contains positive charge carriers (p-layer); the depletion region present no charge carriers instead. When a sufficiently high electrical potential is applied, it allows electrons to flow through the depletion region from the N-type side to the P-type side.

As schematized in figure 3.2, PD uses the internal photoelectric effect without any signal amplification and can be employed in both photovoltaic or photoconductive mode: the first is an unbiased operating mode where the photocurrent has a logarithmic response to the optical power [17], while the second is a biased mode, as a reverse bias is applied across the junction and the measured output current is linearly proportional to the input optical power (figure 3.3).

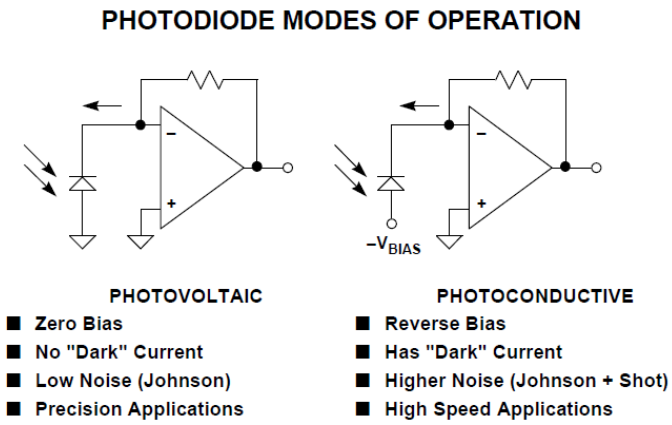

Figure 3.3: Pros and cons of Photovoltaic and Photoconductive mode [14]

Avalanche photodiodes are also based on the internal photoelectric effect, but their name derives from the avalanche multiplication of carriers obtained by applying a large electric field across the APD junction: similarly to what happens in PMT, the charge carriers created by photon absorption are accelerated to give them a sufficient high kinetic energy to generate more carriers through impact ionization, resulting in an internal current amplification of few hundred times [17].

Detector Type	**Gain**	**Dynamic Range**	**Size**	V_{op}	**Speed**	**Robustness**	**Susceptibility**
PMT	Large	Moderate	Bulky	1 kV	Fast	Medium	Higher
APD	Moderate	Moderate	Small	100 V	Fast	Medium	Lower
PD	None	High	Small	1 V	Medium	Good	Lower

Table 3.2: Principal characteristics of the three photodetectors: PMT = Photmultiplier Tubes, APD = Avalanche Photodiodes, PD = Photodiodes [33].

These last two types of photodetectors are actually the most used in near-infrared spectroscopy devices, with the considerable differences summarized in table 3.2[1]. In view of a portable device, which is the final goal towards this work is oriented, an avalanche photodiode would not be convenient because of the high voltage operating range required: eventually, a **Vishay BPW34** silicon p-i-n photodiode has been selected [30], whose relative spectral sensitivity[2] at the various wavelengths is shown in figure 3.4: this photodiode has the optimal response in the range of 770-980 nm, proper for a near-infrared application.

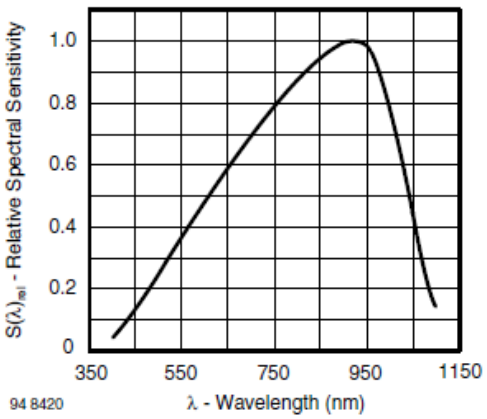

Figure 3.4: Relative Spectral Sensitivity vs. Wavelength of the BPW34 [30]

3.1.3 Model - Electronic Circuit

Before discussing the most suitable operation mode for the photodiode (photovoltaic or photoconductive), it is useful to create its electrical equivalent model to better understand the electronic behavior: in summary a photodiode correspond to a current source in parallel with a diode, a capacitance, a shunt resistance and a series resistance (figure 3.5).

[1]Susceptibility refers to sensitivity to ambient light or magnetic fields

[2]Relative spectral sensitivity is the normalized ratio of the output photocurrent due to the incident light power at a given wavelength, it is also called normalized responsivity.

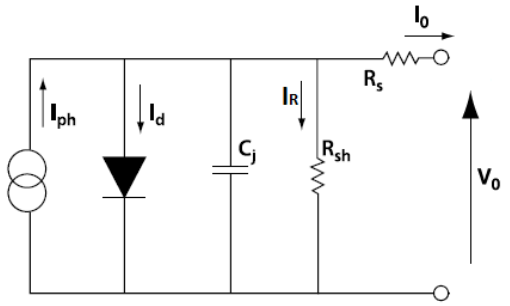

Figure 3.5: Photodiode electrical equivalent: Iph = Current generated by incident light, Id = Diode current, C_j = Junction capacitance, R_{sh} = Shunt resistance, R_s = Series resistance, R_L = Load resistance [24].

The shunt resistance represents the slope of the current-voltage curve of the photodiode at the origin (V=0), experimentally calculated by applying $\pm$ 10 mV, measuring the current and applying Ohm's law: best photodiode performances can be found when the highest shunt resistance is found. Series resistance is due to resistance of the contacts and the resistance of the undepleted semiconductors, if it increases it produces a significant reduction in the output current I_o, therefore series resistance affects the linearity of the photodiode in photovoltaic mode (typical values stay in the range of 10-1000 Ω [24]). The junction capacitance is instead related to the presence of the depletion region with boundaries act as the parallel plates of a capacitor. It is used to determine the speed of the photodiode response. The following formula is used to approximate the capacitance value:

$$C_j = A\sqrt{\frac{\epsilon\epsilon_0}{2\mu\rho(V_a + V_{bi})}} \tag{3.1}$$

where ϵ_0 is the permittivity of free space, ϵ is the semiconductor dielectric constant, μ is the mobility of the majority carriers, ρ is the resistivity, V_{bi} is the built-in voltage of the semiconductor of the P-N junction, V_a is the applied bias and A is the diffused area of the junction. From this equation it is clear that faster rise times are obtained with smaller diffused area and larger reverse biases applied [24].

3.1.4 Noise and Operating Configuration

Noise can affect the output of a photodiode in different way whether it is used in photovoltaic or photoconductive mode, so it is relevant to examine the sources of noise to select the more convenient operative configuration. There are three main types of noise: shot noise, dark current and thermal noise; in brief, *shot noise* describes statistical fluctuations of the photocurrent and is unavoidable because it is

related to the stochastic non-uniform temporal distribution of the photons that enter the detector; anyway this kind of noise can be limited shielding the detector from background radiation e.g. with opaque cover or with NIR bandpass filters. The *dark current* is the current measured even in dark conditions due to electron–hole pairs forming spontaneously in PDs without photons incidence; *thermal noise* is related to the thermal agitation (Brownian motion) of the charge carriers, but is usually quite small compared to the signal obtained when lighting the detector.
The photovoltaic mode is preferred in ultra low light level and low frequency applications (up to 350 Hz). The amount of dark current is kept at a minimum when operating in this mode so high sensitivity is achieved, and the photocurrent have less variations in responsivity with temperature. When applying a reverse bias instead, the width of the depletion junction increases producing a faster response with a decrease in junction capacitance. However, as a side effect, this condition tend to produce larger dark and noise currents.
Regarding the linearity of the response, in the I-V characteristic curve from figure 3.6 it is visible that voltage moves around $V = 0$ in photovoltaic mode, and a quite linear behavior can be guaranteed while V < V_{OC} (open circuit voltage) and the load resistance seen from the photodiode is low (in this case it will be respresented by the input resistance of an operational amplifier). Anyway, the increase in linearity given by a biased configuration would be payed with more noise, as already said. The features offered by these two modes (see figure 3.3) has been compared in view of:

- the speed requirements for the application: the voltage impulses to the LEDs will be in the range of *ms*, while the changes in rise time between photoconductive and photovoltaic are typically some order of magnitude lower and would not give considerable improvements to the system;
- the dark current tolerable: it is minimal, since light power transmission through biological tissues leads to very low detectable levels of light;

Eventually, the most compliant operating mode for this application was recognized as the **photovoltaic** mode.

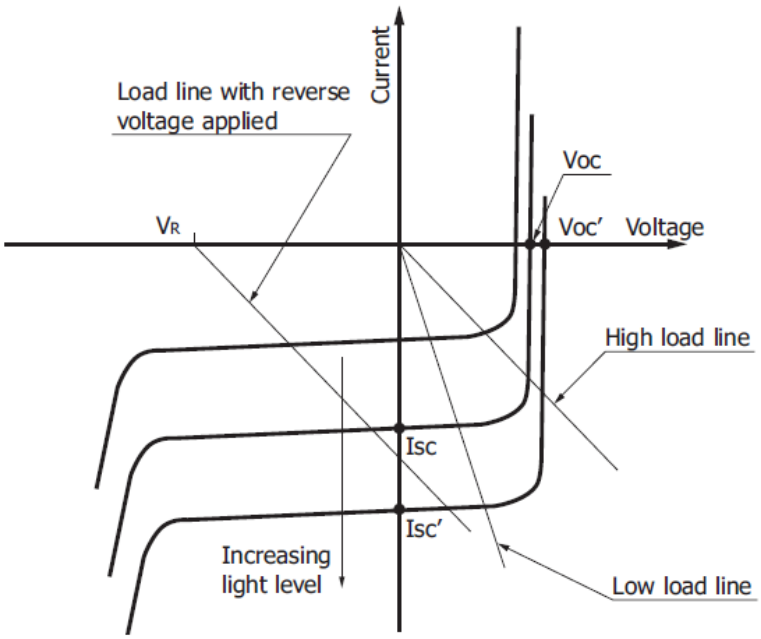

Figure 3.6: Detail of I-V curves of a photodiode in biased or unbiased configuration. V_{oc} = open circuit voltage.

3.1.5 Signal Conditioning

The photodiode output signal can be measured as a voltage or a current but the latter shows far better linearity, a fundamental characteristic for the correct solving of the Lambert-Beer system which implies a linear relationship between the parameters involved. For this reason a transimpedance configuration has been carried out on the PCB on which the photodiode has been soldered. As visible in figure 3.7 the output voltage basically can be obtained as

$$V_o = I_d * R_f \tag{3.2}$$

where Rf is a feedback resistor whose value must be high enough as tissues' attenuation is great (typical values goes from 1 to 500 MΩ).

The receiver PCB of this device is presented in figure 3.9, and its electrical schematics are described in figure 3.8. The components chosen are: a low power, low noise AD795 amplifier, a feedback resistor of 10 MΩ (R1) and a feedback capacitor of 8.2 pF (C3), so that the the operating bandwidth (f_{OP}) is of about 2 kHz, in order to

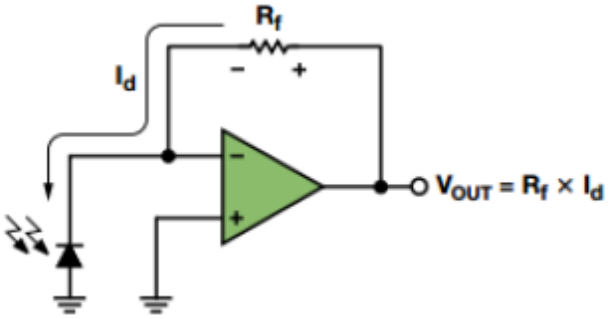

Figure 3.7: Simple electrical scheme of a transimpedance configuration in photovoltaic mode [22].

stabilize the opamp [18].

$$f_{OP} = \frac{1}{2\pi RfCf} \tag{3.3}$$

Two more capacitors (C1 and C2) with the value of 100 nF have been added to work as by-pass capacitors between V_{cc} and ground, to remove AC 50 Hz ripple. $\pm V_{cc}$ corresponds to $\pm$ 12 V at the moment, adapted to the developed prototype with a stabilized power supply.

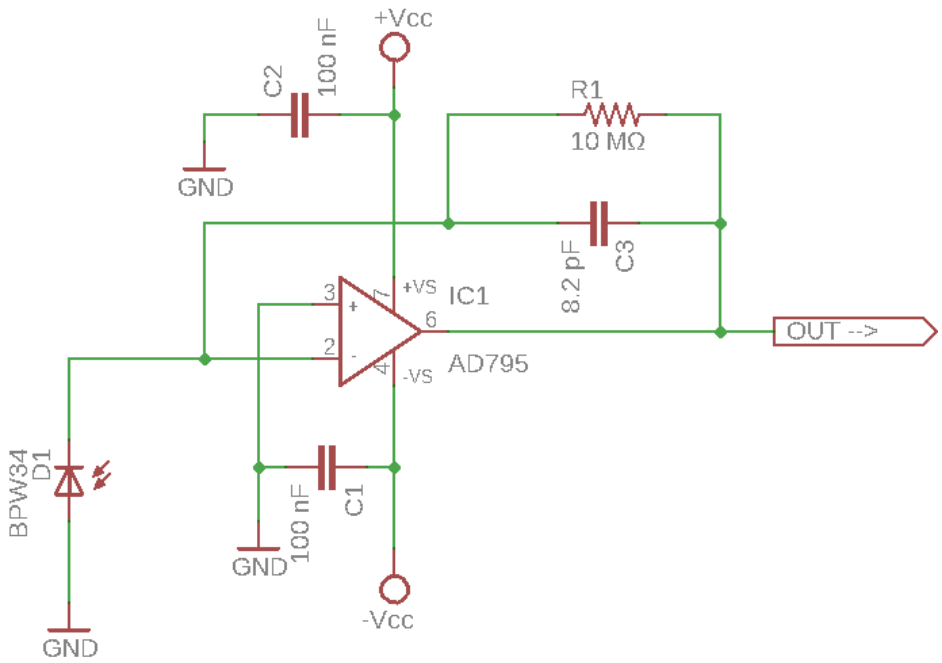

Figure 3.8: Transimpedance configuration set up in photovoltaic mode of operation

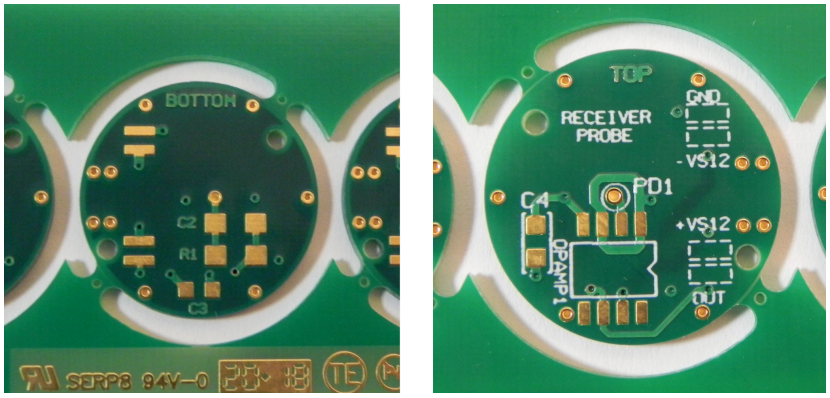

Figure 3.9: Printed circuit boards for the photodiode receiver probe. Left: bottom view, right: top view.

3.2 Mainboard

During the development of the NIRS device, two steps has been made to realize the final system: in the first approach a NIMAX DAQ (the NI USB-6002) was used as control unit, and this represented an intermediate phase useful to confirm the goodness of the time-resolved technique conceived. Once the results were satisfying, the logic of the system passed to the microcontroller which would have become the actual logic unit of the device. Both configurations were powered between $\pm$ 12 V with an Hewlett Packard E3631A Triple Output DC Power Supply, with current limitation of 60 mA to avoid the overcurrent on the LEDs (see section 3.1 for detailed specifications) during the various tests; the power requirements were fixed accordingly to the printed circuit boards which were inherited from a previous NIRS project.

3.2.1 LEDs conditioning circuit

The circuit set up for the control of the LEDs is shown in figure 3.10: it is based on a TL081 operational amplifier configured to work as a voltage follower, giving as input a square wave of 1.5 V with period of 100 ms and DC of 10% as seen in section 2.4.

The value of the resistor chosen is 33 Ω so that about 45 mA pass through the

LED, obtaining enough light intensity without damaging the component itself. However this current level can't flow directly out the opamp, which gives only hundreds of μA, so a MPSA13 Darlington transistor has been connected in series to the LED to reach the current flow desired; in this configuration it is possible to control the level of brightness with voltage pulses up to 3.3V, which allow an hypothetical current of about 100 mA.

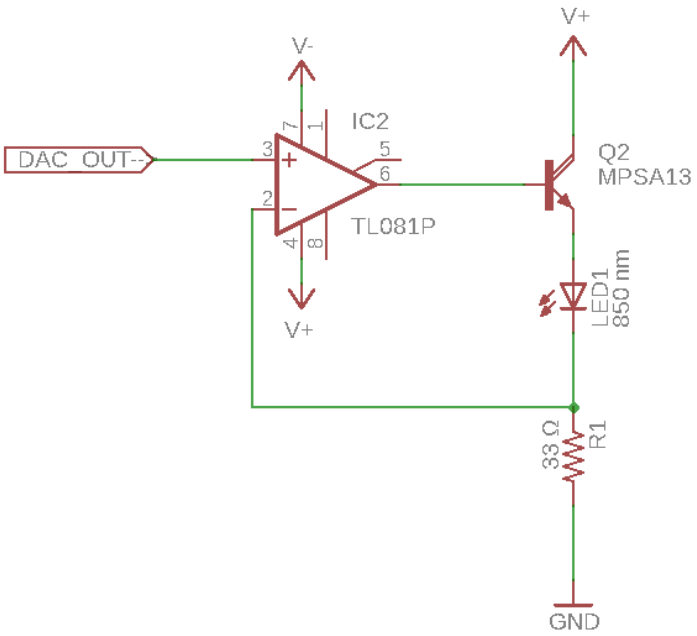

Figure 3.10: LED conditioning circuit: in the figure the 850 nm is taken as example, but the same circuit is used for all the LEDs.

3.2.2 Amplification Stage for Photodiode Output

A stage of amplification has been added between the output of the transimpedance amplifier and the microcontroller ADC input pins, since the values of the voltage coming from the photodiode resulted from tens to hundreds of mV, depending on the subject, while the input range of the ADC can vary from the two devices used for the acquisition; thus, an amplification stage was required to exploit each input range at best. For the microcontroller is $\pm\ V_{cc}/2$ which corresponds to $\pm$ 1.65 V, while for the NIDAQ is $\pm$10 V: in figure 3.11 the scheme represents the electrical set up where the opamp is a TL081 used in a non-inverting configuration with amplification factor

G calculated as:

$$G = 1 + \frac{R_3}{R_4} \tag{3.4}$$

This gain factor was chosen to work at half of the ADC range, to ensure avoiding saturation of the input ports. The R4 resistor has a value of 2.7 kΩ for both configurations, while R3 is 180 kΩ for the NIDAQ board and 18 kΩ for the microcontroller, leading to an amplification of 67.7 and of 7.7 respectively.

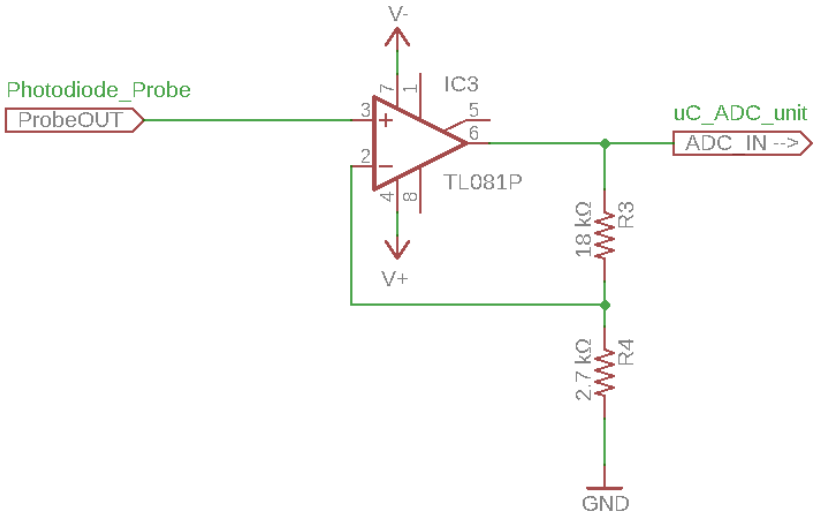

Figure 3.11: Amplification Stadium of the photodiode's voltage signal to comply with the microcontroller's ADC input range

3.3 NIMAX USB-6002: First System Set Up

Figure 3.12 presents the circuital diagram of the first system set up to make the initial considerations on the acquired signals and the impulse parameters. It is essentially composed by three blocks: the conditioning circuits for the IR LEDs, the amplification stage for the output signal of the photodiode probe, and the NI-6002 device. Two main differences have to be noticed with respect to the microcontrolled-based configuration that will be discussed in the next section:

1. the different amplification stage of the photodiode probe;

2. the acquisition of the pulse signal given to LED1: it is brought to the ai1-ai5 differential input pair of the DAQ, with the aim of temporizing the photodiode

output sampling (see section 6.1.1 for further explanations).

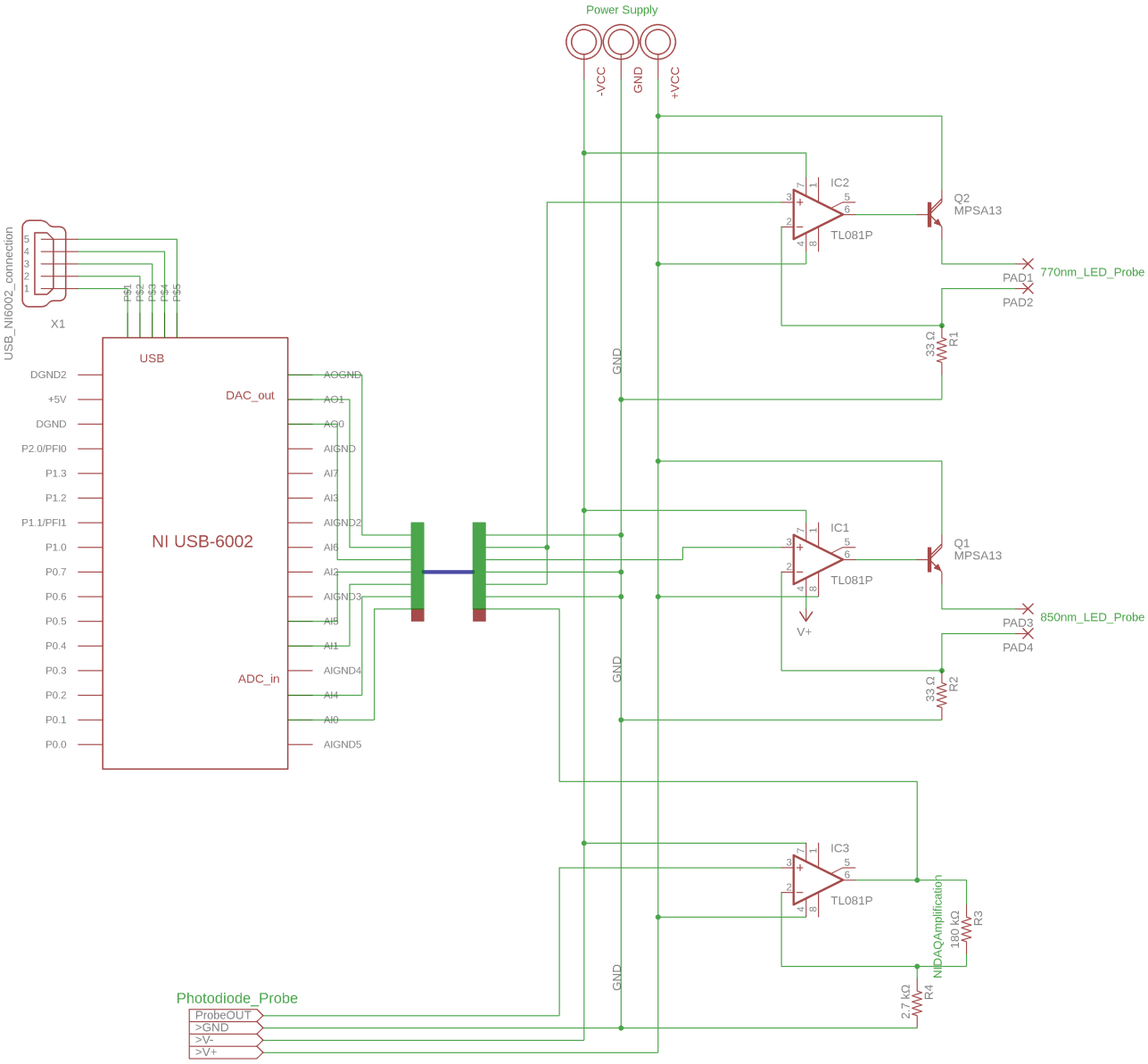

Figure 3.12: Electrical scheme of the system circuit when using NI USB-6002

With this set up the transmission of data occurs only through USB serial communication and the storage of the signals is carried out later in the Matlab environment. For the method implemented to make the NI-DAQ system work in the desired way and to manage the acquired data see chapter 6.

3.4 Microcontroller Unit

Like previously stated, this NIRS device is thought to be a low-power system able to store and/or transmit the voltage data acquired during a cerebral oxygenation monitoring for quite a long time without needing to be recharged (see section 7.5 for a further examination of this aspect). To reach this low-consumption purpose, the prototype mainboard has been developed around a low power AVR 8-bit microcontroller (the ATxmega128A1U) programmed through the specific evaluation board, the Xmega A1U Xplained Pro, which represents the control unit of the hardware mainboard. The microcontroller will have the function of a data logger which acquire and save the direct voltage data: have access to the raw signal from the photodiode is not always possible in commercial devices and this particular feature can be useful during the probes positioning process to have a direct estimation of the quality of the signal. In figure 3.13 the proposed hardware configuration is presented, and resulted similar with the one presented previously for the NIDAQ. However, in the microcontroller-based system, data can be transmitted through USB just like before, but they are also constantly saved on a 4 Gb microSD card which exploit the extension header of the evaluation board: in this case an Atmel I/O1 Xplained Pro SD extension was used.

As previously anticipated, the amplification of the photodiode signal should be appropriately adjusted for the specific input range of the ADC with a 18 kΩ resistor; compared to the NIDAQ setup, here two additional features are provided: two LED indicators used to display the device status and the user button for starting and stopping the acquisition process. As visible in the figure, two USB connectors are available for the microcontroller and can provide the power to the board, but they have different aims: one is linked to the embedded debugger (EDBG) and it is used for the programming of the board via Atmel Studio, the other is the target USB and can provide a USB serial communication to transmit stream of data.

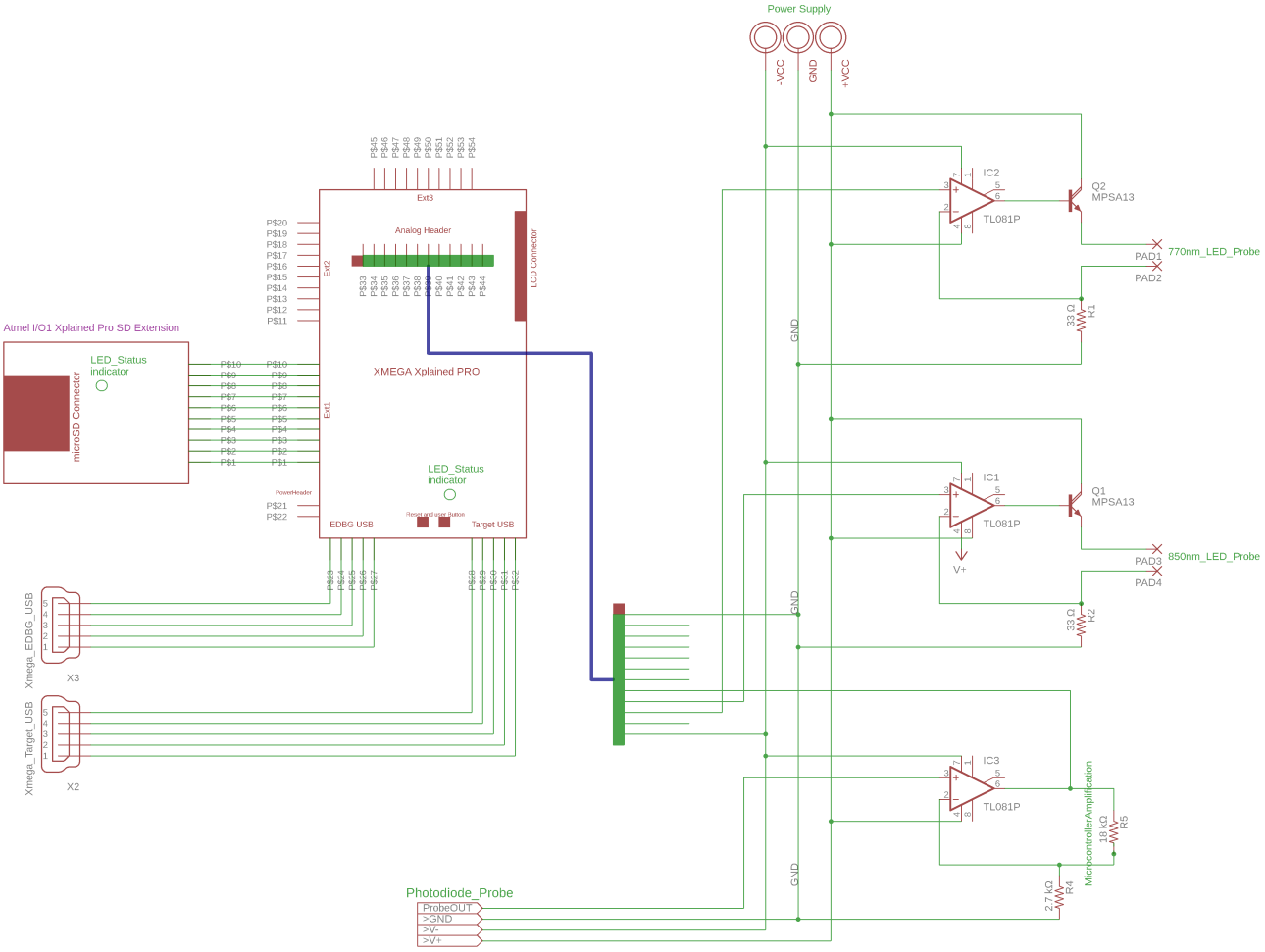

Figure 3.13: Electrical scheme of the system's circuit after substituting the NI-DAQ with the microcontroller

In summary, the selection of the microcontroller was based on a number of desired features for the device to be designed:

- Low-power architecture;
- Two independent two-channel Digital to Analog Converter;
- Integrated USB interface;
- Possibility to communicate with an external SD card.

The ATxmega128A1U 8-bit microcontroller seemed to adapt to those specifications as it is characterized by:

- 128 kB of flash memory;

- Two independent 12-bit two-channel Digital to Analog Converter;
- Two sixteen channels 12-bit Analog to Digital Converter inputs;
- Operating voltage: 1.6 – 3.6V;
- One USB 2.0 device interface;
- Four serial peripheral interfaces (SPIs);

As said, the data logger task was achieved by continuously storing data only onto the microSD card, adopting an SPI communication and, beside this function that is always implemented, there is also the possibility of a continuous stream of the acquired values towards a host computer connected with an USB cable. The two operating modes are distinguishable according to the state of the LED indicator on the XMEGA and the SD extension boards:

1. Only the LED on the SD extension board is switched on: data are being stored on microSD (the SD-LED is circled in yellow in figure 3.14);
2. Both the LED on the SD extension board and on the XMEGA are switched on: data are being stored on microSD and sent to PC (the XMEGA-LED is circled in red in figure 3.14)

Either the storage alone or together with the USB streaming can be started and stopped by pushing the button indicated in figure 3.14 on the XMEGA board; further details about data acquisition and transmission will be examined in chapter 6; moreover, the introduced architecture was realized by using the general evaluation board, but it is intended to be transferred on a single PCB in the future, once the battery needs of the device have been examined to guarantee a good autonomy.

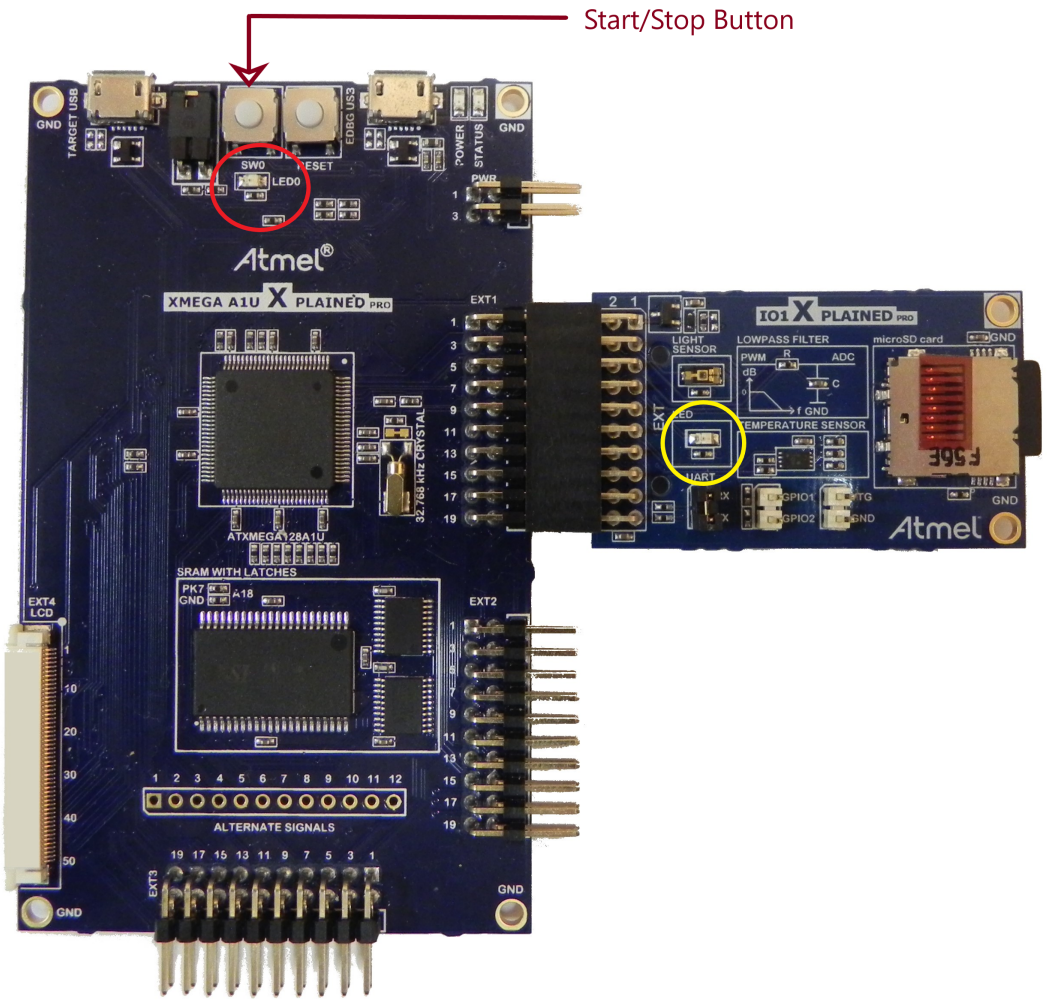

Figure 3.14: XMEGA A1U Xplained Pro: in red = XMEGA-LED, in yellow = SD-LED

Chapter 4

Structural design

This chapter describes the design of the probes containers and their holder: two specific materials have been selected basing on their suitable physical and mechanical properties and both probes have been provided with a strain relief for the 3.3 mm, 6 wires cable. The structures have been designed with Solidworks 3D CAD software and then 3D-printed.

4.1 Probe Containers

The two probes containers presented in the following are both realized from a black rigid plastic resin to obtain a solid structure. The black color was chosen to isolate as much as possible from ambient light and to prevent LEDs light from laterally passing through and being detected by the photodiode, once the probes are positioned on the forehead. The containers have been 3D printed with a Form 2 SLA laser 3D printer (Formlabs). Figure 4.1 describes the geometry studied for the emitter probes, where the cylindrical shape adapts to the PCB circular form and a strain relief has been added to prevent the soldered cables from breakage because of mechanical stresses at the entry of the container; furthermore, the height of the cylinder has been chosen accordingly to the thickness of the final hardware of the probe, avoiding the direct skin-components contact which was obtained instead with a final casting of PDMS, as will be explained.

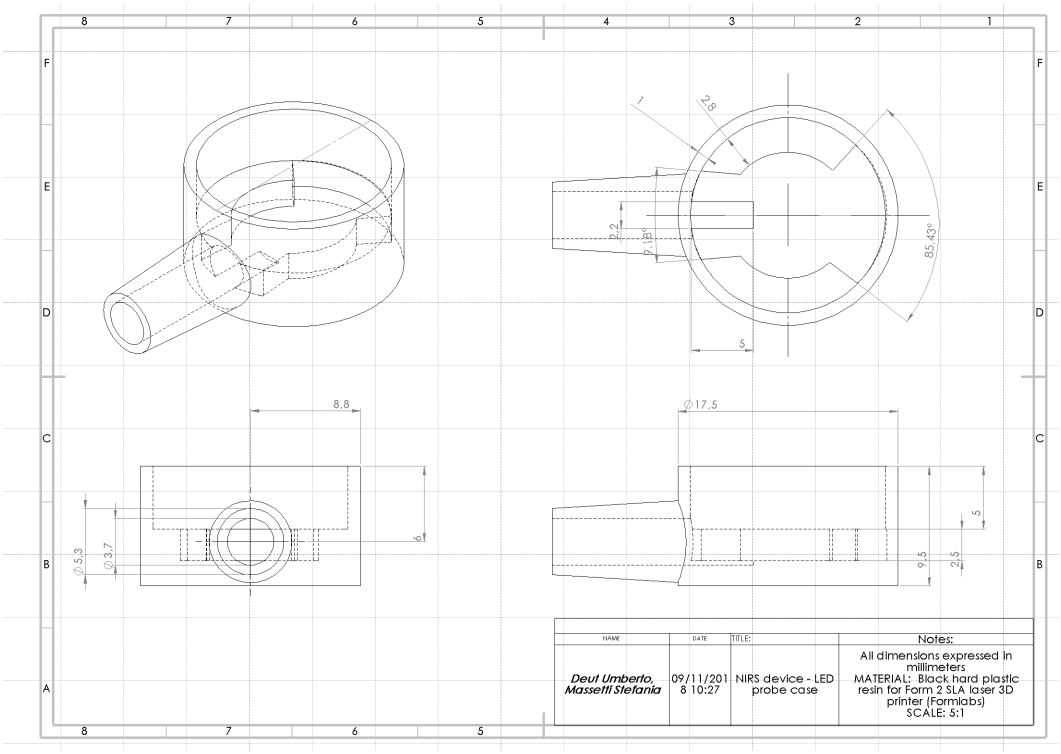

Figure 4.1: Technical drawing of the IR LED probe case

For what concern the receiver probe, the structure of its container is similar to the previous one, except for its dimension, it is slightly bigger and the depth of the internal space, which has been projected to give the possibility of testing the system with different photodiodes and to guarantee a good distance from the skin both in case of a bigger or a smaller receiver component, as will be explained in section 7.1.1.

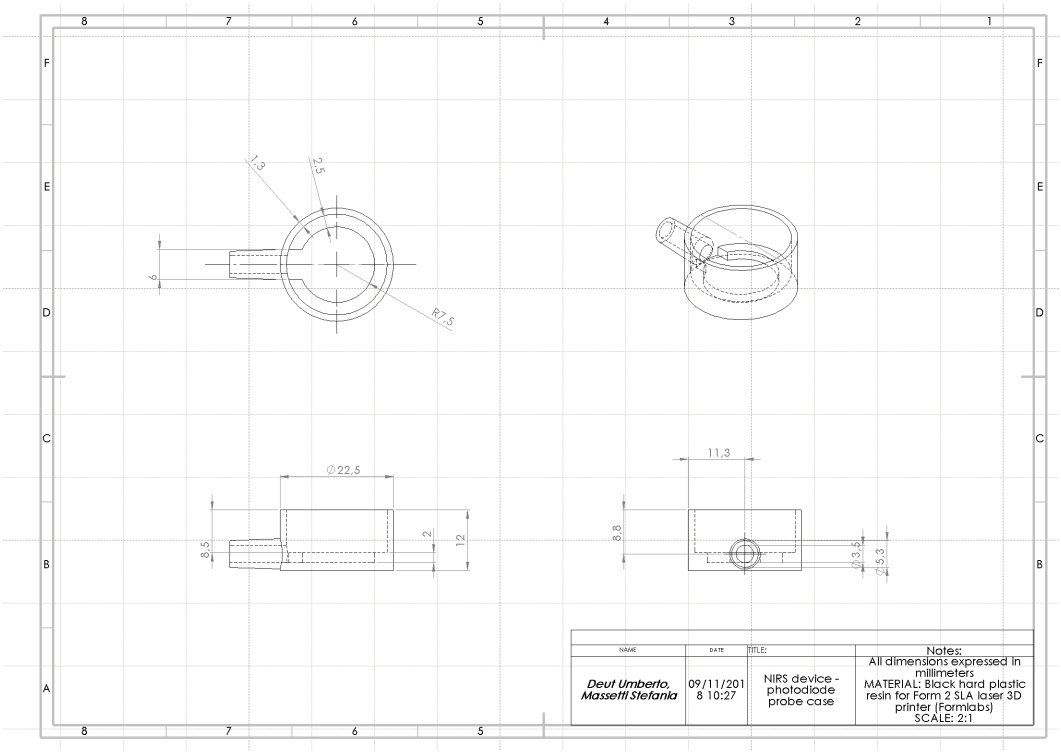

Figure 4.2: Technical drawing of the photodiode probe case

PDMS casting

As a final adjustment, all the empty space of the probes is filled with PDMS to make them compact and robust components: the details of the process are presented in the diagram of figure 4.3. The two substances implied in the realization of the PDMS compound are the silicon base and the curing agent that promotes the polymerization; it must be blend in a ratio 10:1. Firstly the two components have to be carefully weighted with a precision balance: in this PDMS realization, 15 grams of polymer have been mixed with 1.5 grams of curing agent and, after stirring the compound for about two minutes, it was left for an hour in a covered container to remove the air bubbles produced. Meanwhile the probes have been secured on a stable support with adhesive tape and, one hour later, PDMS was slowly poured into the probes trying to avoid the creation of air bubbles. Particular attention has been paid while pouring the PDMS in order to obtain a convex meniscus on top of both probes, necessary for a perfect coupling with forehead skin that avoids the creation of an air

layer interposed, which would result in noisy effects due to light refraction. The containers were left for 3 days in a covered container to avoid the dust to deposit on the exposed surface; the final result is presented in figure 4.4.

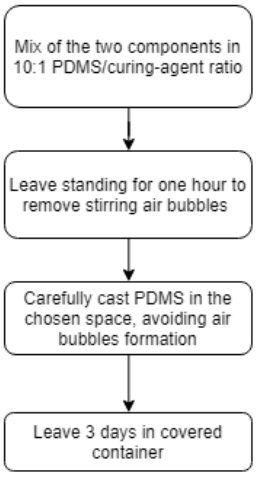

Figure 4.3: Brief overview of the procedure used to prepare the fluid PDMS compound and the casting process

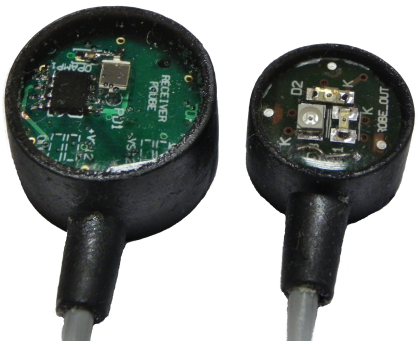

Figure 4.4: Final probes after filling with PDMS

4.1.1 Flexible probes holder

The design of the probes holder reflected the requirement to guarantee a stable and comfortable positioning of the probes on the forehead. For this reasons the flexible

Opaque Black VisiJet M2 EBK[1] was the material selected for the holder realization: the black color was chosen to accomplish the same goal as in the probes containers; then the studied geometry was 3D printed with the ProJet MJP 2500 Plus printer by 3D Systems. The dimensions of the structure designed have been decided to make the holder as small as possible, to comply with the comfort requirements. As reported in figure 4.5, the distance between the centers of the probes sockets is 4 cm, a typical value used in NIRS devices, while the width is of 2 cm, the same measure of the double-sided adhesive tape that would be put on the surface of the holder to fix it on the forehead. The length of this upper surface was made of 8 cm to exploit a major contact area with the skin.

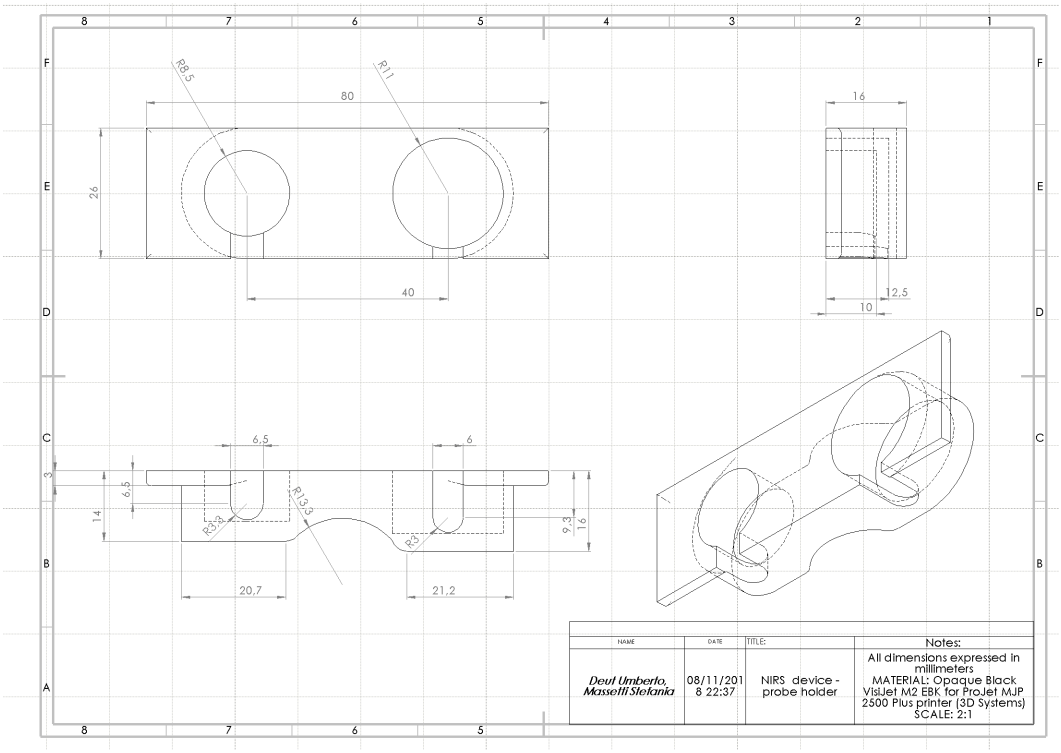

Figure 4.5: Technical drawing of the holder designed to contain the probes.

[1]Elongation at break 160-230%, Young's modulus 0.27-0.43 MPa

4.1.2 Holder Positioning on the Forehead

The final structure with the probes inserted is visible in figure 4.6: this is the holder to be sited on the right side of the head, instead the left holder has the two probes sockets inverted. The two configurations were provided because in some subjects one side of the brain might be more responsive than the other, when a certain task is demanded in a fNIRS recording. In the placement studied, the cables pass over the head of the subject and will fall down to the box containing the control logic of the system, once it will become portable.

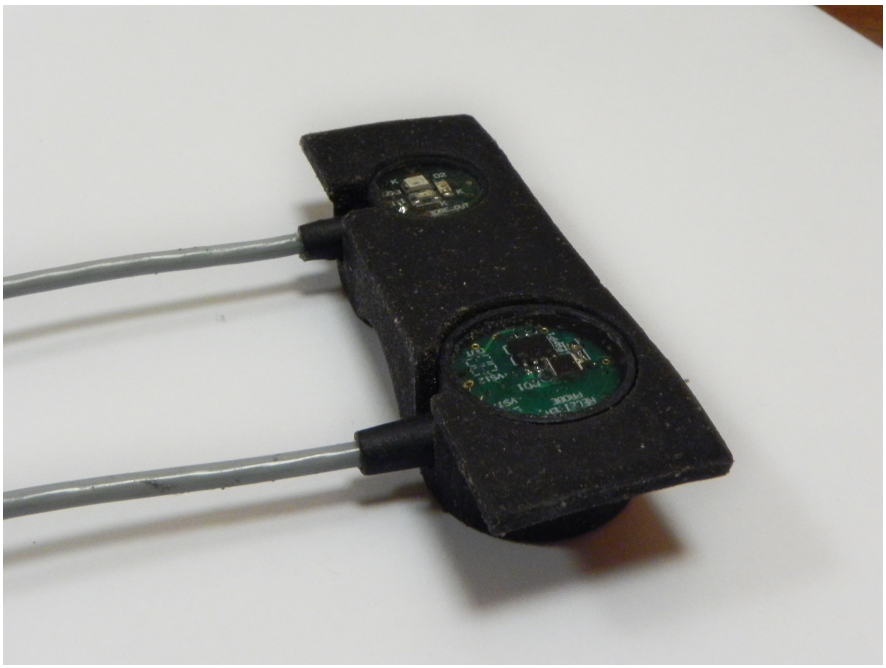

Figure 4.6: Final probes holding structure

Figure 4.7: The picture illustrates the positioning of the probes holder on a subject: the emitter is almost on the temple while the receiver is placed two cm to the right from the middle of the forehead.

Chapter 5

Firmware

As anticipated in section 3.4, the Atxmega128A1U was adopted to work as control unit of this NIRS device prototype: after the analysis with the NIDAQ system, the acquisition flow and the electrical parameters to use were definitively fixed, thus the logic of the device was moved to the firmware of the microcontroller, which was programmed exploiting C as the programming language.

5.0.1 Flow charts and Code Details

The device presents three principal functional states shown in figure 5.1: a standby state, where the device is continuously waiting for a "button pushed" event to start the data acquisition, and the two main routines for the data acquisition, one which implements the specific data logging functionality and the other which saves data to the SD card and also transmits them through a serial communication port. Thus the main routine of the code contains two blocks of actions, one for the writing on SD, the other for allowing the stream of data through a USB port; as shown in figure 5.2, after the first part of initialization, the while loop of the program starts at the so called 'Start Acquisition Loop': a NIRS recording starts once the button on the XMEGA board is pushed, but a start action could cause the continuous toggle of the *status_flag* whose value controls the beginning and ending of the acquisition. To avoid this problem, the value 100000 has been assigned to the variable called *wait* in order to disable the button until its decrease to zero: the value is high enough

to disable the start functionality of the button for about 3 seconds, considering a clock cycle of 25 μs due to the system clock settings of the microcontroller. After this amount of time has passed the device status can be changed again.

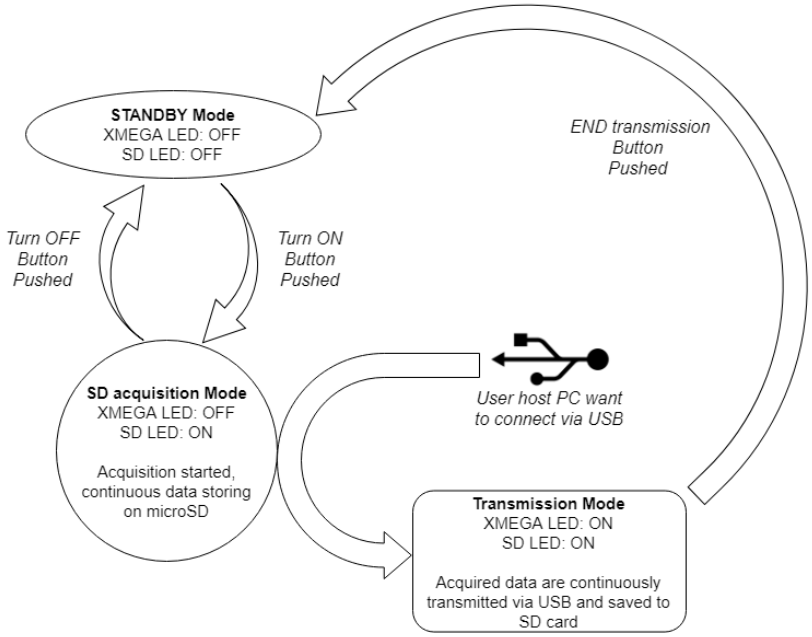

Figure 5.1: Device state diagram. The Button in figure is the *Start/Stop Button* of figure 3.14 but it has different functions depending on when it is pushed: it can launch the SD acquisition alone and stop it when pressed again, or it can stop also the USB communication in case it was requested from an host computer after the recording had started. The couple of LEDs indicated notify the state of the device

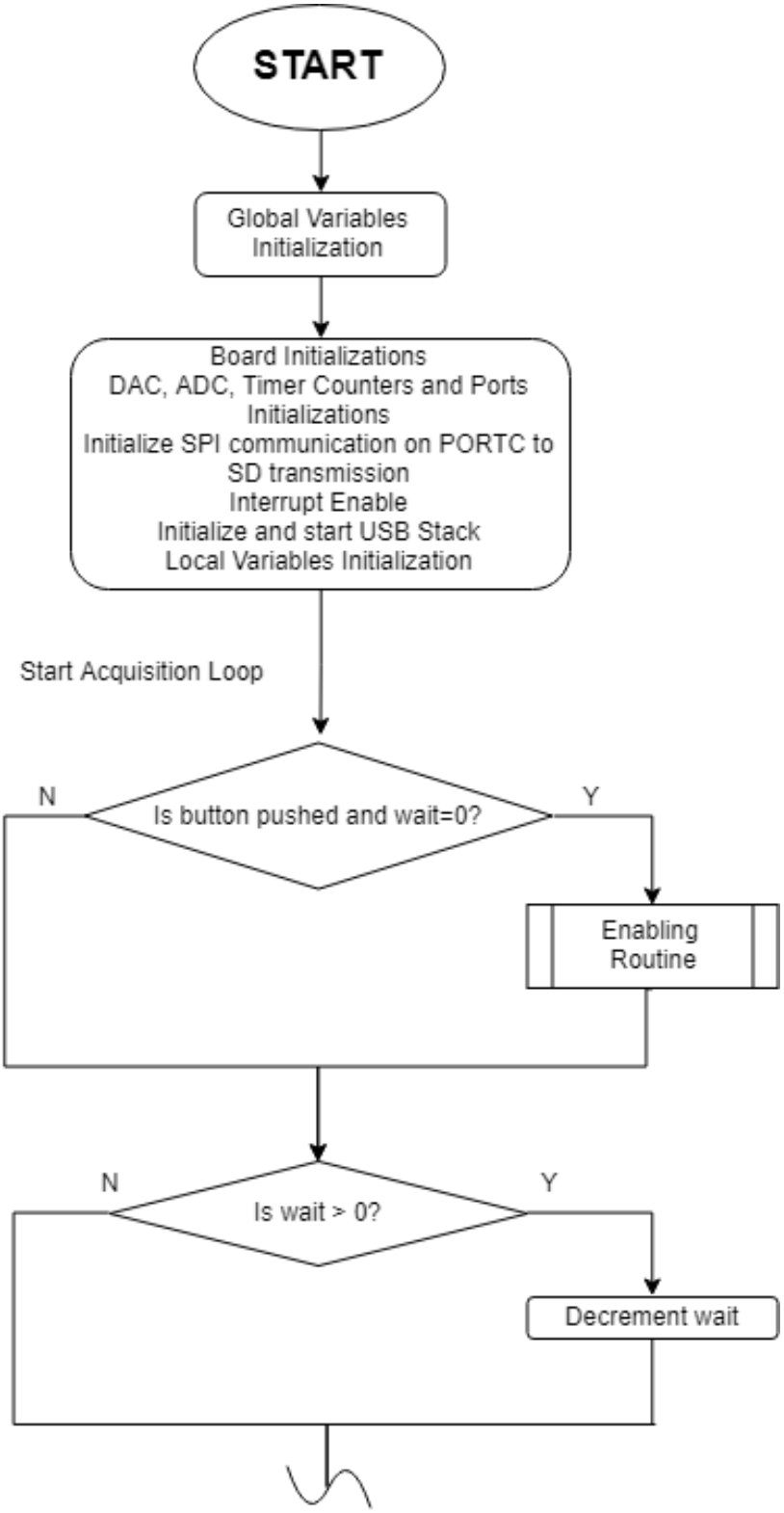

Figure 5.2: Main routine - part one.

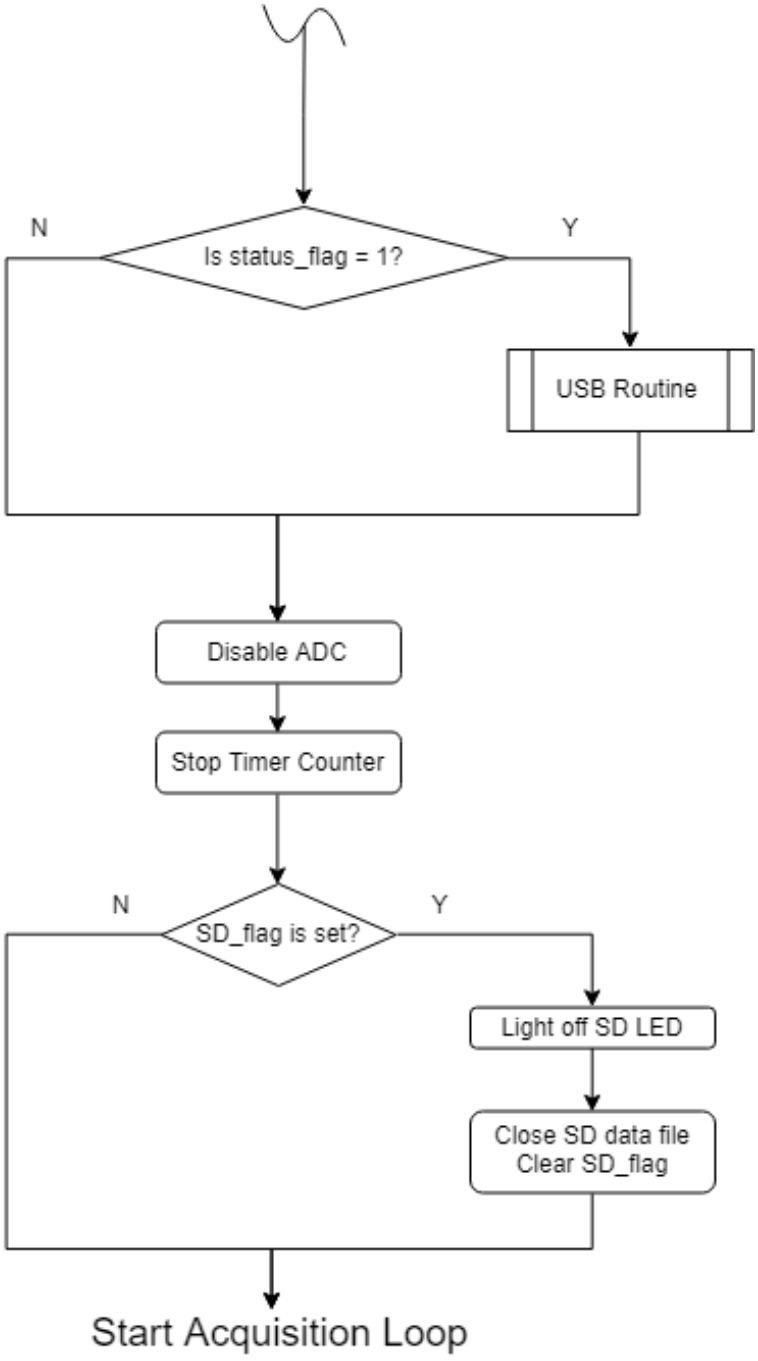

Figure 5.3: Main routine - part two.

Once the acquisition has been launched checking the button pushed and the wait equal to zero conditions, the **Enabling Routine** begins: the ADC and DAC are enabled and start acquiring and generating signals, then the Timer Counter Zero (*TCC0*) begins its counting, which is used for the triggering of DAC channels and obtaining the right timing for the LED blinking.

Moreover a *.txt* file is created on the SD card and the SD LED is switched on to confirm to the user the good response of the system (see figure 5.4); note that the microSD process is finished when the button is pushed and the SD-LED is turned off. For what concerns the ADC, its conversion frequency has been set to 93.7 kHz, meaning that one conversion lasts 10 μs, and is triggered with the Timer Counter One (*TCC1*) overflow every 0.5 ms: in this way 20 samples can be gathered in the 10 ms of LED impulse, even though only 18 samples are saved actually, avoiding to take the first and last one to ensure that all samples are taken inside the LED-on interval, so that no errors due to delay between DAC output and ADC input reading occur. This ADC frequency was chosen to have a discrete amount of samples to average, thus decreasing the sensitivity of the device to the noise; considering this averaging step, the frequency of the extracted voltage values is of 10 Hz, as seen in section 2.4.

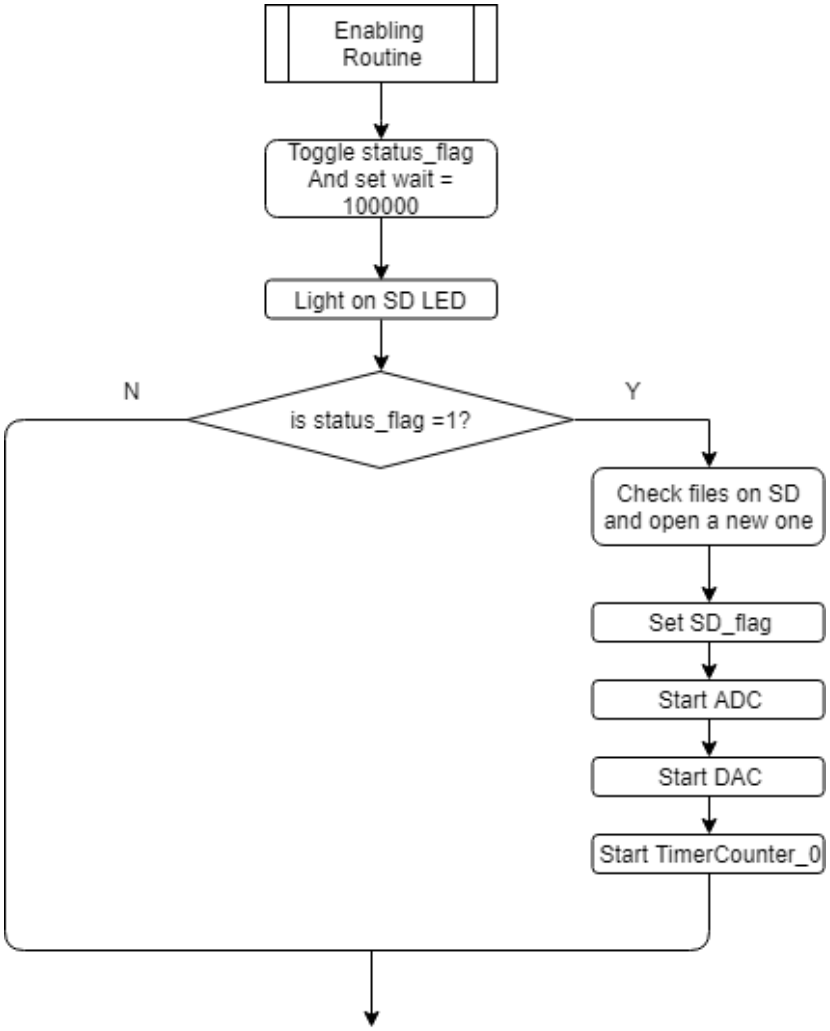

Figure 5.4: Enabling Routine

Only after the *status_flag* has been set to one in the *Enabling Routine*, the **USB Routine** can start. The control on the *status_flag* is used to avoid that a new recording is launched when stopping the previous one, as the same button is used for the two functions and they would conflict. In the *USB Routine* data are saved only on microSD until the number 1 is sent by the interfaced device to the microcontroller through the USB serial port, so that the system can work without losing data even if the USB connection is not established. In case this word is received, the USB streaming starts and continues until the user button on the XMEGA is pushed and the number 5.1 is sent by the microcontroller to close the transmission with the host device. This number was chosen as the voltage data during the acquisition will never reach that value so it can not be confused with the significant data. The closing trans-

mission number is not an integer value as the opening transmission one, because the averaged voltage data from the photodiode are saved as float so it was convenient to maintain this type also for the word received by the PC. Since in MATLAB, the software used to develop the App for the USB communication (see chapter 6), the maximum number of bits allowed in this kind of transmission is 8 bit, each 32-bit float was sent splitted in 4 packets and then re-united into a unique number from the software side. The beginning and the ending of the USB communication are notified to the user by respectively switching on and off the XMEGA LED. Once the recording has been interrupted, the *status_flag* is toggled so that the last check on its value permits to disable ADC and DAC, stop *TCC0* and close the SD file: when the SD LED is at low level the loop has reached its end and can start back with another button-pushed event.

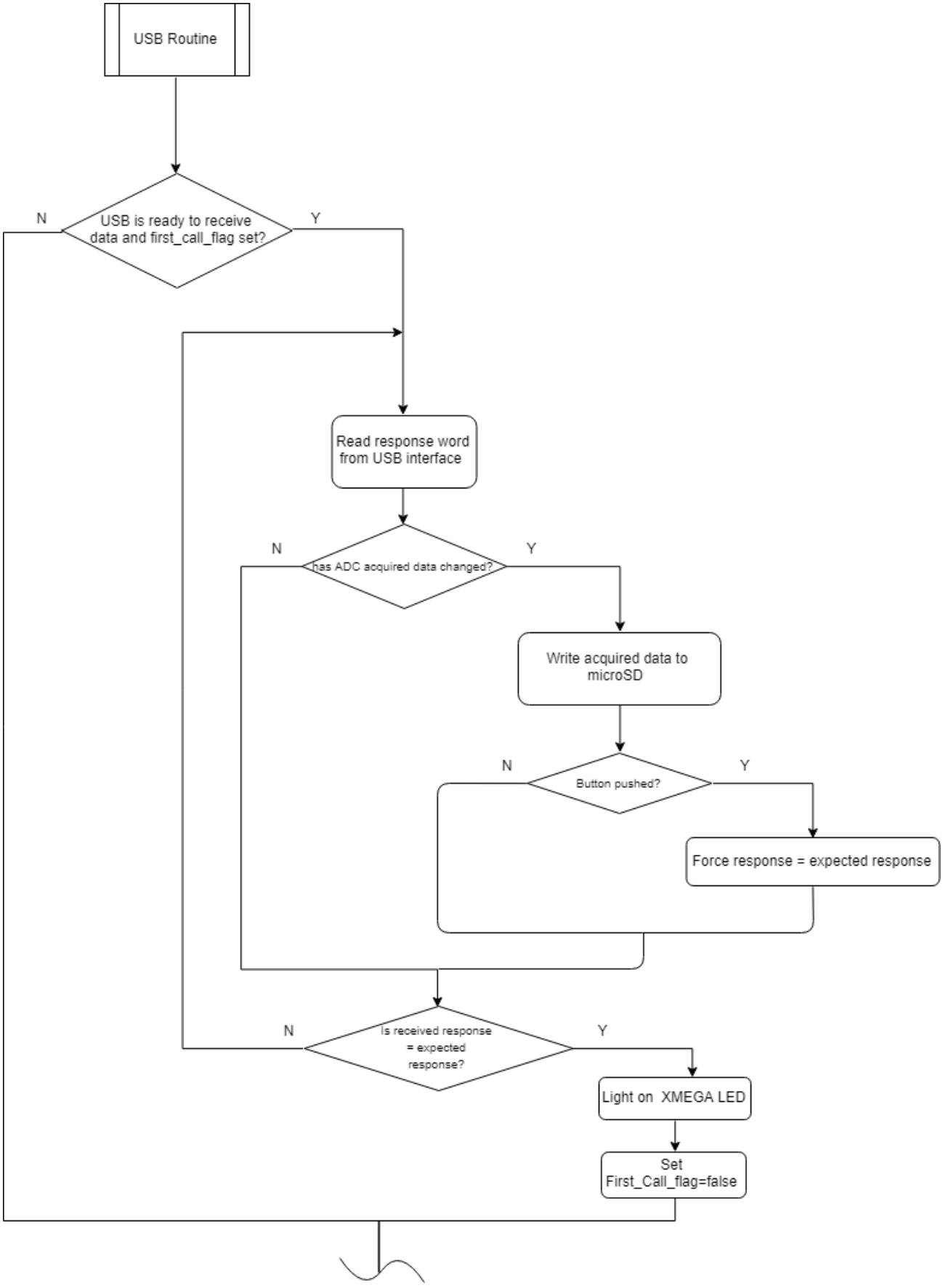

Figure 5.5: USB communication routine - part one.

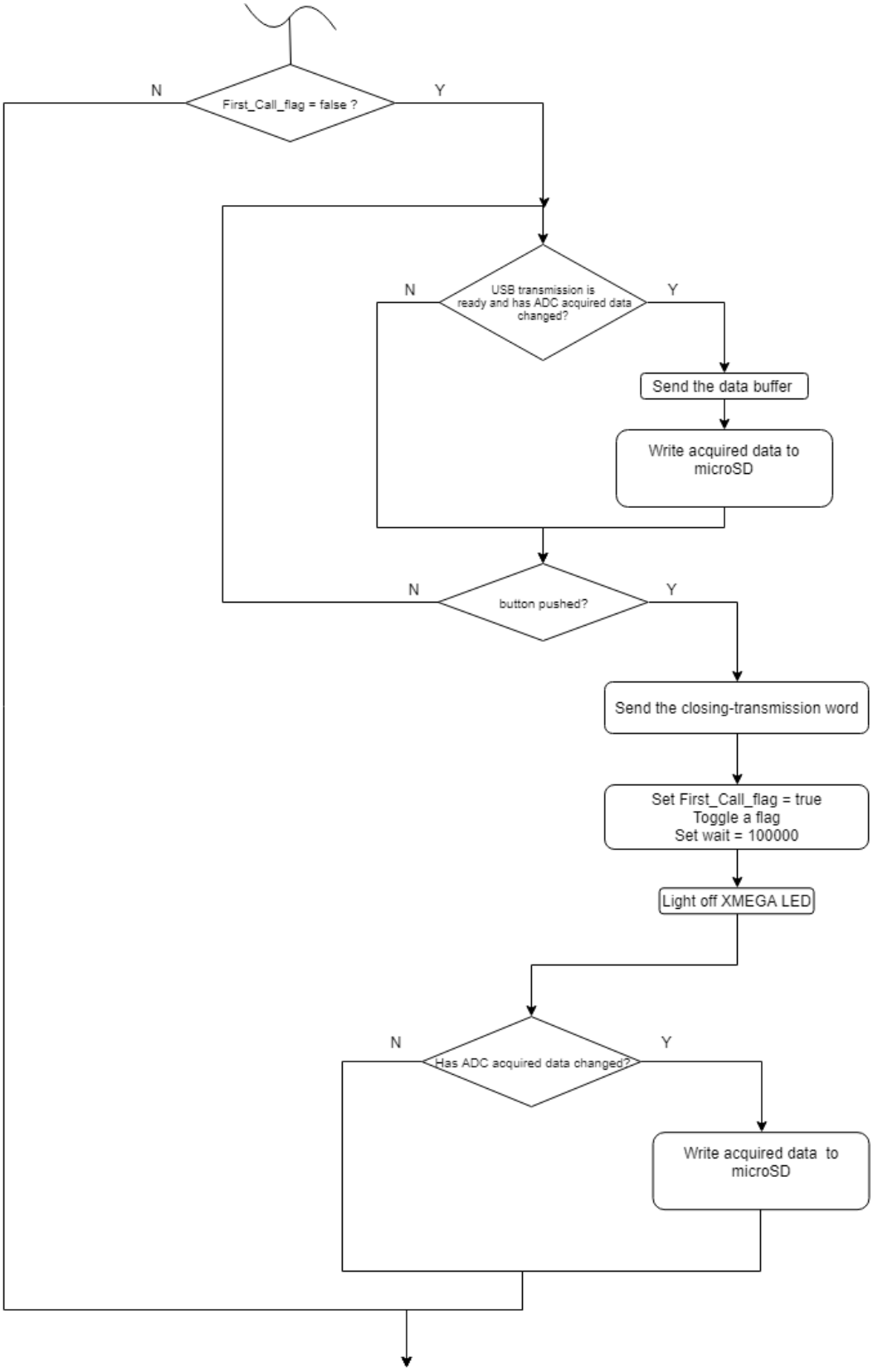

Figure 5.6: USB communication routine - part two.

5.0.2 Data Acquisition Storing and Sending

In this section there is a further clarification of the system management for what concerns the square wave pulses generation, the acquirement of the photodiode data and their utilization. First of all, as visible in the flow chart of figure 5.7, the callback function *my callback* is executed every 10 ms in response to a *TCC0* overflow: it has been implemented in order to control which DAC channel had to generate and maintain the impulse for the established duration, this function is processed by running the *dac write* function whose diagram is displayed in figure 5.8. The *my callback* routine sets also the *flag actual* variable, which is used in the *ADC handler* callback to fill the right array of data, distinguishing between voltage data due to LED1 and LED2 blinking or data acquired during their off phase. Moreover, the first time *my callback* is executed, *TCC1* is started: in this way it is possible to synchronize the ADC readings with the output of the DAC.

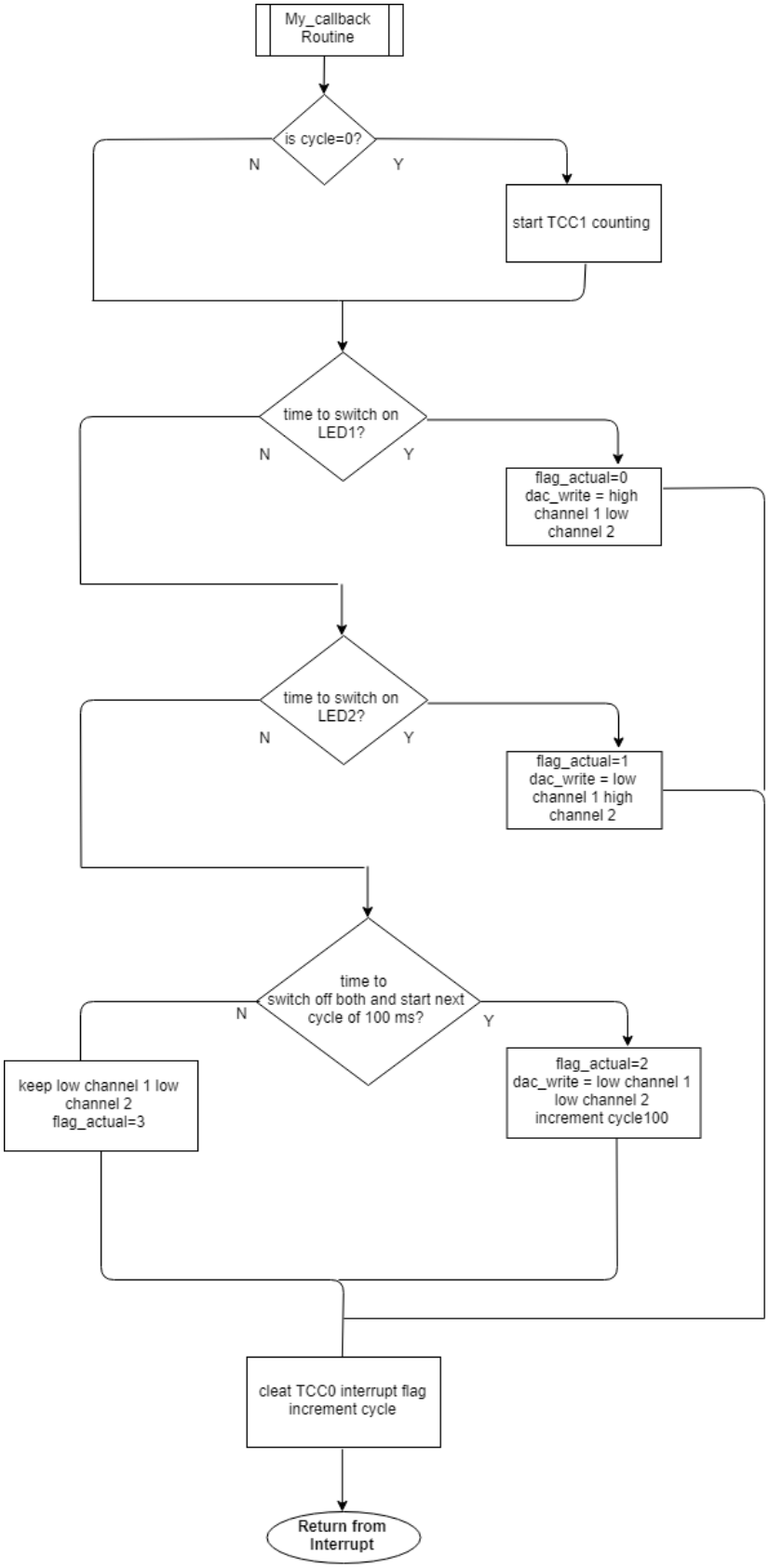

Figure 5.7: Callback for DAC handling

In figure 5.9 the flow chart of the **ADC_handler Routine** shows the management of the acquisition. The check on *flag actual* reveals the system state among the three possible conditions:

- LED1 on LED2 off - 10 ms duration
- LED1 off LED2 on - 10 ms duration
- Both LED1 and LED2 off - 10 ms duration

This is necessary since, to solve the Lambert-Beer equation, the voltage values from LED1 and LED2 must be differenciated one from the other and both from the noise. Three arrays has been prearranged to contain the 18 samples taken in each of the listed cases: once the state has been recognized, first there is a control on the fullness of the previous state array and, if it is, the *average* function (figure 5.10) is called giving these 18 samples as input and obtaining the **average voltage value**, **standard deviation** and **maximum and minimum voltage values** as output; these are the data for the three listed conditions, that will be saved and/or sent during NIRS acquisition and as said in the previous section, the resulting data signals will have one sample every 100 ms for each of the four output values (sampling at 10 Hz). The average function is performed only once in each case, as the array used to calculate these parameters is emptied right after, and the counter variable used to fill is set to zero in order not to enter anymore in this initial "if" condition. Then, the voltage data from the photodiode are added to the proper array until *flag actual* changes, and the same operations just described repeat, with one exception in the noise instance: once both LED1 and LED2 are off, noise is not sampled immediately, due to possible errors in the DAC switching from high to low value; only after 10 ms have passed the 18 samples of noise are stored and averaged during the next cycle of pulses.

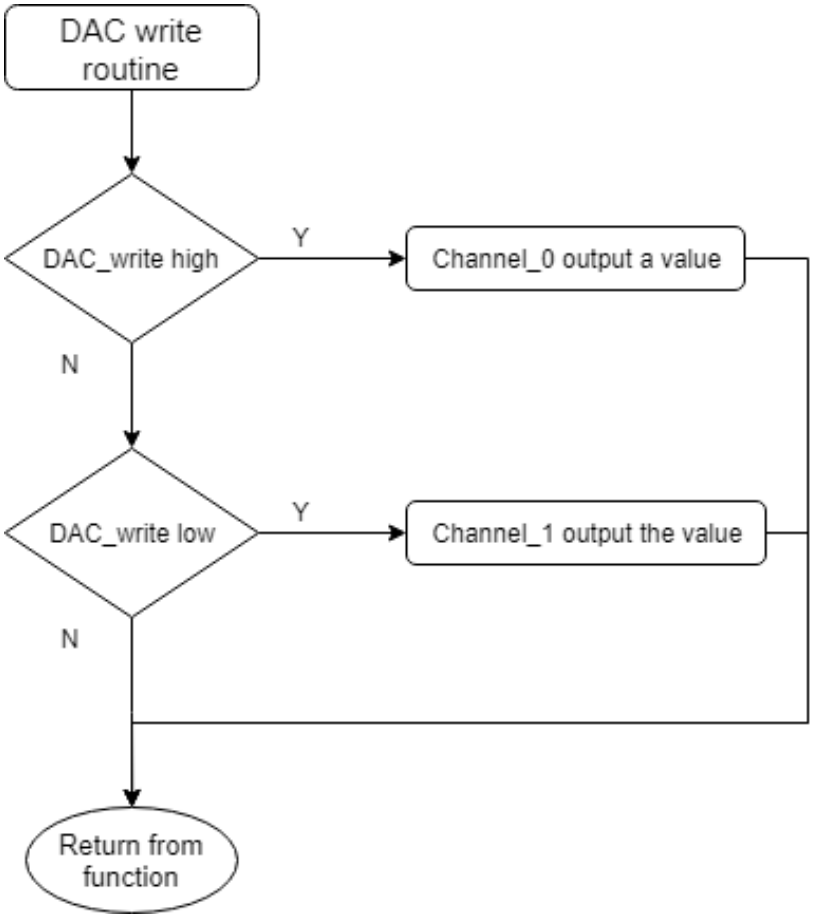

Figure 5.8: Function to handle the DAC output channels

Any time a new group of values have been calculated by the *average* function, they can be stored on microSD only or sent via serial USB communication too, as already seen in the *main routine* discussion. The format of the data packets to send was thought to make the extraction of each system state information easier: for each configuration, group of **5 values** are compacted together, the first one is the variable *flag actual* which permits, when unpacked by the Matlab interface, to identify correctly the states; the others are the ones relative to voltage levels, in the sequence previously listed. A custom-made software application has been created on MATLAB expressly for reading these data packets and elaborate them to obtain the [ΔO_2Hb] and [ΔHHb] signals; refer to chapter 6 for further explanations. In table 5.1 a summary of the microcontroller configuration is proposed.

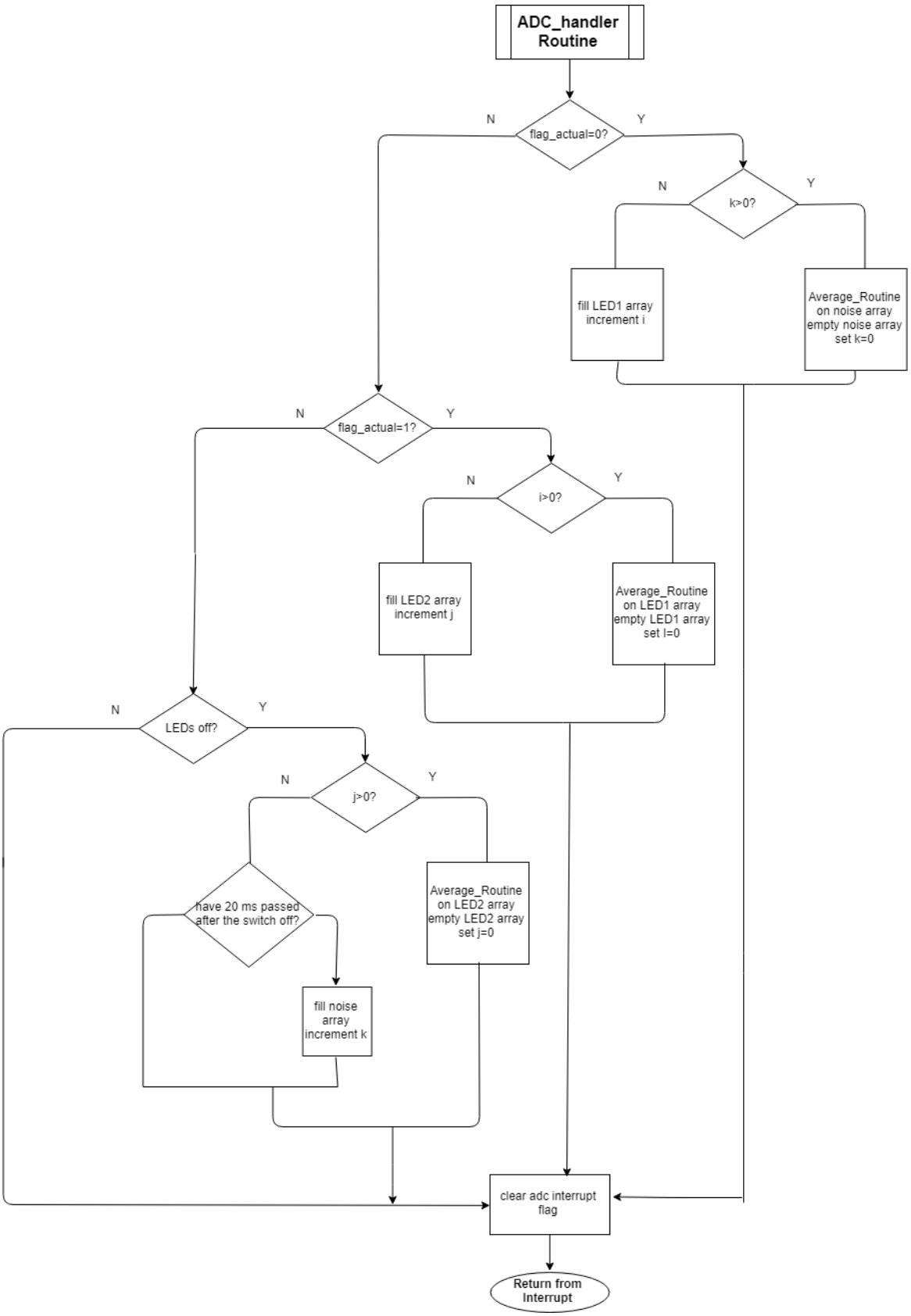

Figure 5.9: Callback for ADC handling

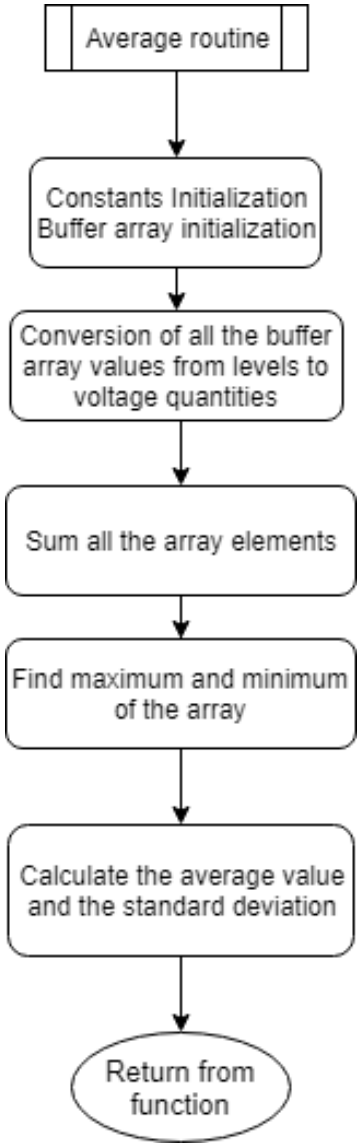

Figure 5.10: Average function to calculate on the 18 samples the averaged, the maximum and the minimum voltage value and the standard deviation.

ADC	Conversion frequency = $system_clock/512$ = 93.75 kHz. (one conversion lasts about 10 μs) Triggered by TCC1 overflow $\Rightarrow$ ADC sampling every 0.5 ms (2 kHz frequency) Differential 12 bit signed conversions VCC referenced (Vcc/1.6) PA7 positive pin PA0 negative pin
DAC	DACB 12 bit conversions VCC referenced $\Rightarrow$ maximum voltage value obtainable = 3.3 V Channels PB2 and PB3 Triggered by TCC0 overflow Square wave pulses of 1.5 V with T = 100 ms and DC = 10 % (pulse duration = 10 ms)
Timer Counter Zero	Clock set with 1/1024 prescaler leads to a frequency of 46.87 kHz Clock cycle = 21 μs Count value for overflow every 10 ms = $\frac{pulseduration}{Clockcycle} = 470$
Timer Counter One	Clock set with 1/256 prescaler leads to a frequency of 187.5 kHz Clock cycle = 5.3 μs Count value for overflow every 0.5 ms = $\frac{ADCsamplingtime}{Clockcycle} = 94$
Spi Port	PORTC for microSD communication Baud rate for communication with slave device 400 kHz
USB	12 Mbps at full speed Baudrate = 115200 DataBits = 8 Parity = None Stop Bits = 1
System Clock	System Clock up-calibrated at 48 MHz for USB transmission

Table 5.1: Summary of the main settings of the microcontroller modules

Chapter 6

Software Design

6.1 MATLAB Graphical User Interface

This chapter presents the MATLAB application created to manage the NIRS system using either the NIMAX USB-6002 or the microcontroller; it was thus structured in a way that permitted to exploit identical graphical tools both with the DAQ and the microcontroller when used in USB streaming mode, while an additional Tab Group was dedicated to the processing of the data stored on the microSD, exploiting a slightly different course to get to the Lambert-Beer system solution. The *NIRS Acquisition* and the *microSD Reading* Tabs represent the principal case of use of the interface, so the chapter will focus on their description, but two other functions have been developed for giving additional versatility to the App, exploiting a general signal acquisition and generation functionality of the DAQ: these sections will be briefly discussed at the end of the chapter.

6.1.1 NIRS Acquisition Tab Group

The main tab of the app carries out the management of the whole NIRS system, from the LEDs blinking, the photodiode output reading, the Lambert-Beer equation solving and the real-time plotting of the signals, to the saving of the results at the end of the recording. The figure 6.1 shows the window that appears when the App is started; in the left side, a panel is devoted to the control of the impulse settings and

below other system configurations can be chosen before the start of the acquisition; in the middle a number of parameters calculated on the voltage data are displayed and a warning field is present to notify the status of the acquisition; on the right the control buttons are provided to start and stop the system with the NI-DAQ (the blue *Start* and *Stop* buttons) and with the microcontroller (the yellow *Start_MICRO* button and the relative *Connection* status text field). Moreover in this section there are the *Set ZERO POINT* and *Set MARKER* buttons to manage the real-time acquired signals graphs, and the *PLOT* button, useful, at the end of the acquisition, to show the whole ΔHHb and ΔO_2Hb signals in a Matlab figure, since the real-time plot has a fixed observation window. Finally the two graphs at the bottom are used to display the oxygenation signals and the voltage bars for the evaluation of the quality of the acquisition.

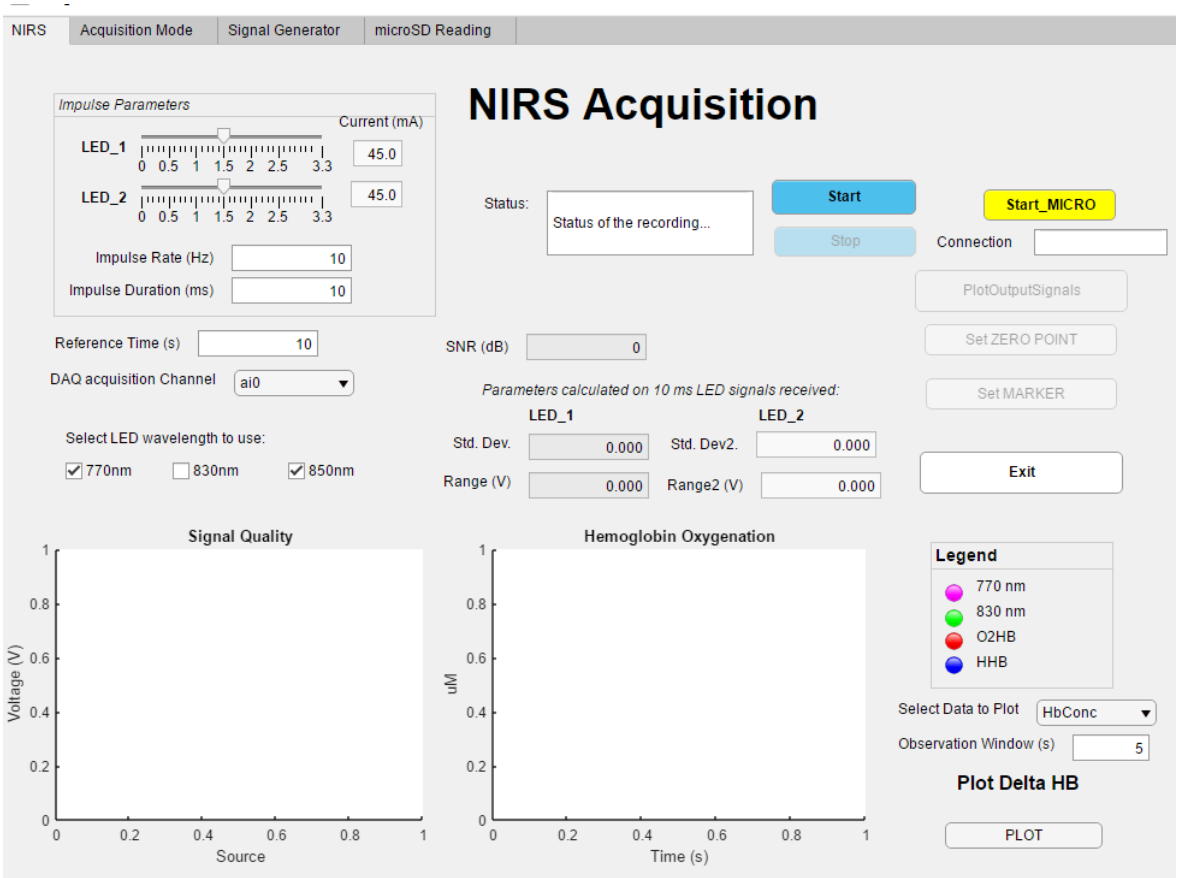

Figure 6.1: Matlab Application created to interface with the NIRS system

The options on the *impulse parameter* panel can regulate:

- the voltage amplitude of the square wave sent to the LEDs, separately for LED1 and LED2 with the devoted slider: this option is only available with NI-DAQ recordings, while in the microcontroller case the value set is 1.5 V and can be changed only modifying the firmware. 1.5 V is also the default value of the sliders, whose range goes up to 3.3 V, according to what is the maximum voltage value the ATxmega128A1U can give; in this way it has been possible to exploit the same LEDs driving circuit with both the two control logic. Just at the right of these sliders it is also indicated the current level that passes through the LEDs to easily make a comparison with the maximum values found in the LEDs documentation and avoid the risk of overcurrent;

- the impulse rate in a range between 1 and 10 Hz, in order to have time periods between 100 ms and 1 s;

- the impulse duration, which gives the possibility to have longer "LED-off periods" without changing the pulse duration and vice versa, to find the better solution for the system in terms of SNR and power consumption. The default value is 10 ms and, since the DAQ sampling frequency was set to 1 kHz, 10 voltage values are acquired from each received impulse. The impulse duration can not exceed half of the whole time period, as it is necessary to maintain the right LEDs blinking: in case it is wrongly set a warning window will appear, as shown in figure 6.2.

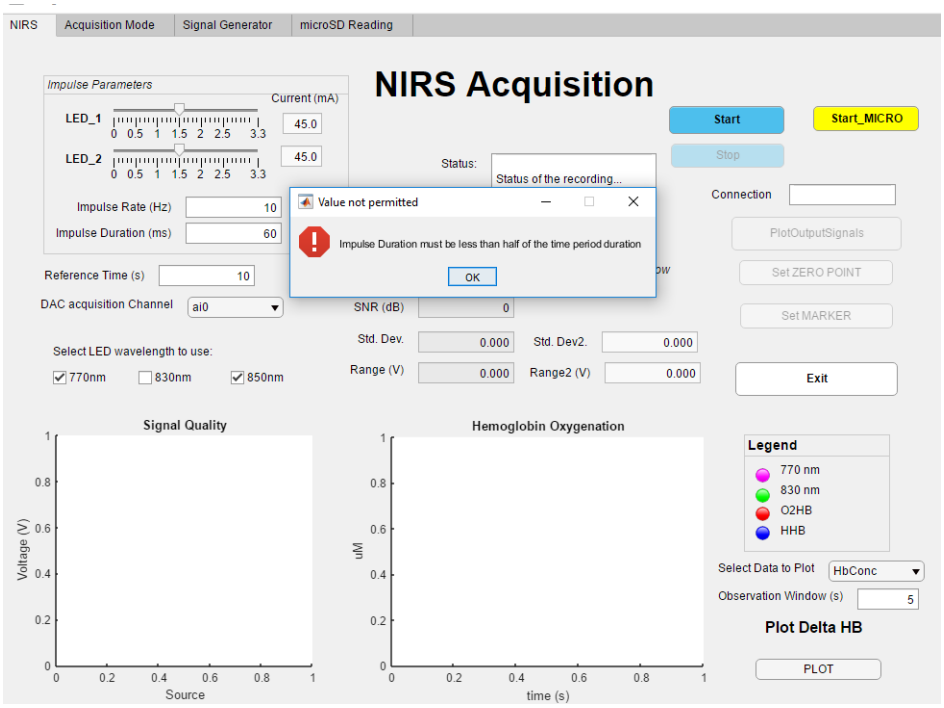

Figure 6.2: Warning window in case of wrong impulse duration setting

Then some other general settings can be set in the App before the acquisition starts:

- the reference time, which correspond to the number of seconds of signal to average for the purpose of creating the zero point from which calculating the variations in the chromophores concentration;
- the DAQ channel for the acquisition, selected from the drop down menu;
- the wavelength of the couple of infrared LEDs to use, choosing between the three available.

On the right of the graphs, two parameters can be used to manage the settings of the signals plotted: the first is the *Observation Window*, used to display the desired number of seconds of the acquired signals in the **Hemoglobin Oxygenation** graph, in a range between 0.5 s and 60 s[1]; the second is a drop-down menu that permits to select the data to be plotted between the hemoglobin oxygenation concentrations,

[1]It should be taken into account that a longer observation time can lead to an higher graphical load and consequently to lagging problems

the mean values extracted with a 10 Hz frequency and the real-time raw data sampled at 1kHz directly from the output of the photodiode amplification stage.
In the upper right of the window the *Start* button launches the NI-DAQ system and the *Stop* button terminates it. Once the parameters have been decided and the *Start* button is pressed also the *PlotOutputSignals* button is enabled, and permits to open the *TimeWindow* App created to show in a different window the output signals used to control to the LEDs.

During the NIRS recording the three bars of the *Signal Quality* graph displays every 2 seconds the values of the amplitude of the voltage read from the photodiode due to LED1 and LED2 blinking and due to noise (see figure 7.3a): these bars are used together with the SNR value for the best holder positioning with the most intense signals; moreover, during this phase the two LED bars should be equalized by modifying the two voltage-controller sliders to achieve the same signal intensity from the two LEDs thus preparing the system with the best conditions. For what regards the parameters in the middle of the window (e.g SNR and voltage range), they are printed every two seconds and are calculated on the 10 ms received signal from the photodiode; in fact, the range of amplitude of the samples averaged for the single LED and their standard deviation are used to estimate the noise on the signal and the accuracy of the acquisition.
The main difference between the DAQ-controlled and the microcontrolled system is limited to the averaging routine of the samples taken from each pulse, since in the first case this step is made in the App environment, while in the second case the mean value has been already calculated on the microcontroller side and is sent to the App through USB communication (see section 5.0.2). In both cases, the averaged value is stored in the proper array, depending on which LED was lightened, and used to calculate the [ΔHHb] and [ΔO_2Hb] signals, which are then shown in the *Hemoglobin Oxygenation* graph, when the default *HbConc* configuration has been set in the *Select Data to Plot* drop-down box. The plot starts after a number of seconds equal to the reference time have passed from the beginning of the data acquisition, to permit the creation of the voltage reference value for both of the channels, averaging the samples stored until that moment in each of the two arrays. The *Set*

ZERO POINT button is enabled when this reference time has passed twice and is useful because in a real-time acquisition it may be necessary to reset the zero point, e.g. in case of movement artifacts or other problems that have resulted in undesired behaviour of the signals. Moreover with the *Set MARKER* button, markers can be set over the signals to underline the starting point of a task performed by the subject. During the recording, the *Warning* text field is helpful as it can notify whether the system is working fine or there is some error because of which the LEDs are not blinking (*LED NOT WORKING PROPERLY!* warning) and moreover notifies the storing of the data after the *Stop* button has been pushed (*Saving Data...* warning).

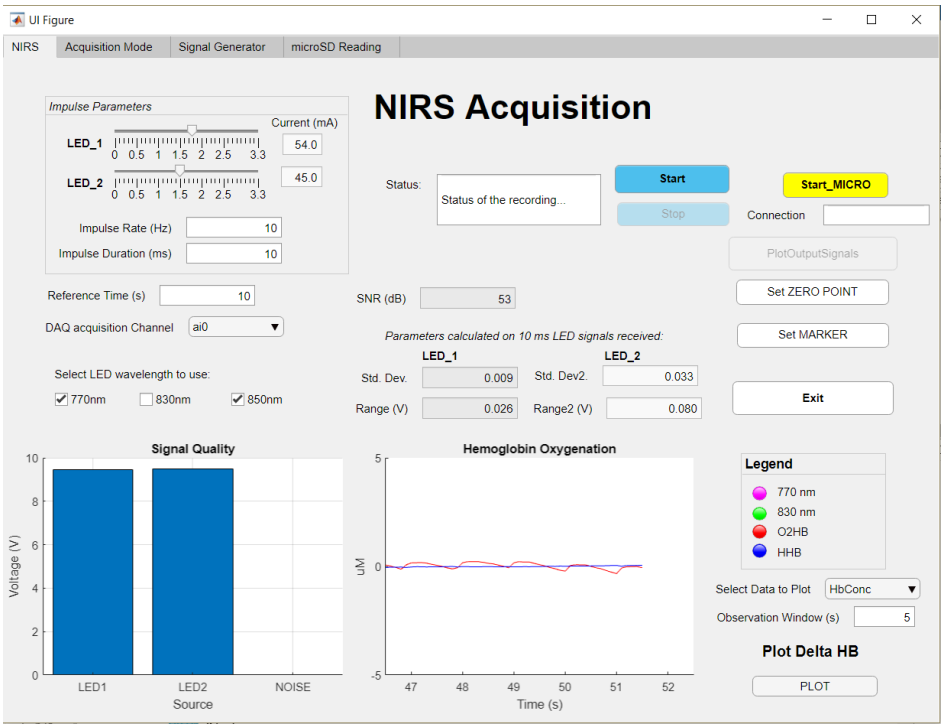

Figure 6.3: The figure refers to a DAQ acquisition (the*Stop* button has been pushed before the screen-shot). The SNR obtained in this case was of 53 dB, a value that permits to be sure of the correct holder positioning. Moreover on the *Hemoglobin Oxygenation* graph the cardiac rhythm is visible on the [ΔO_2Hb] signal.

After the acquisition finishes, the relevant data are automatically saved in a folder named "*NIRSdataFolder*" to allow a further inspection of the signals or to post-

process the acquired information.

6.1.2 Notes about the MATLAB Code

A certain number of issues linked to the utilization of the NI-DAQ had to be faced during the creation of the App. First of all it has been chosen both to generate the voltage square waves and to acquire the the voltage data in a *background* session: when interfacing with a DAQ tool, Matlab gives the possibility of working in this operation mode which allows the PC to control the DAQ signal acquisition and generation without working with the main Matlab workspace, that is left free to process the data without interrupting other tasks. For this reason, this mode resulted compliant to the system management thought for this purpose as it was necessary to perform simultaneously the control of the LEDs lightening using channels ao0 and ao1 and the reading and processing of the photodiode output from channels ai0 and ai4 (differential acquisition), using for the two aims the *QueueMoreData* and the *plotData* callback function respectively.

Another problem came upon during the set up of the system concerned the synchronization of the photodiode voltage sampling with the LEDs blinking; in order to achieve this goal, another differential couple of channels (ai1 and ai5) was used to acquire the square wave generated from channel ao0 which was the one used to give the first pulse, and a threshold on the voltage value read was used to find the index corresponding to the transition from low to high level. Then this index was used to re-align the array filled with real-time voltage data with impulses sent to the LEDs, as visible in figure 6.4.

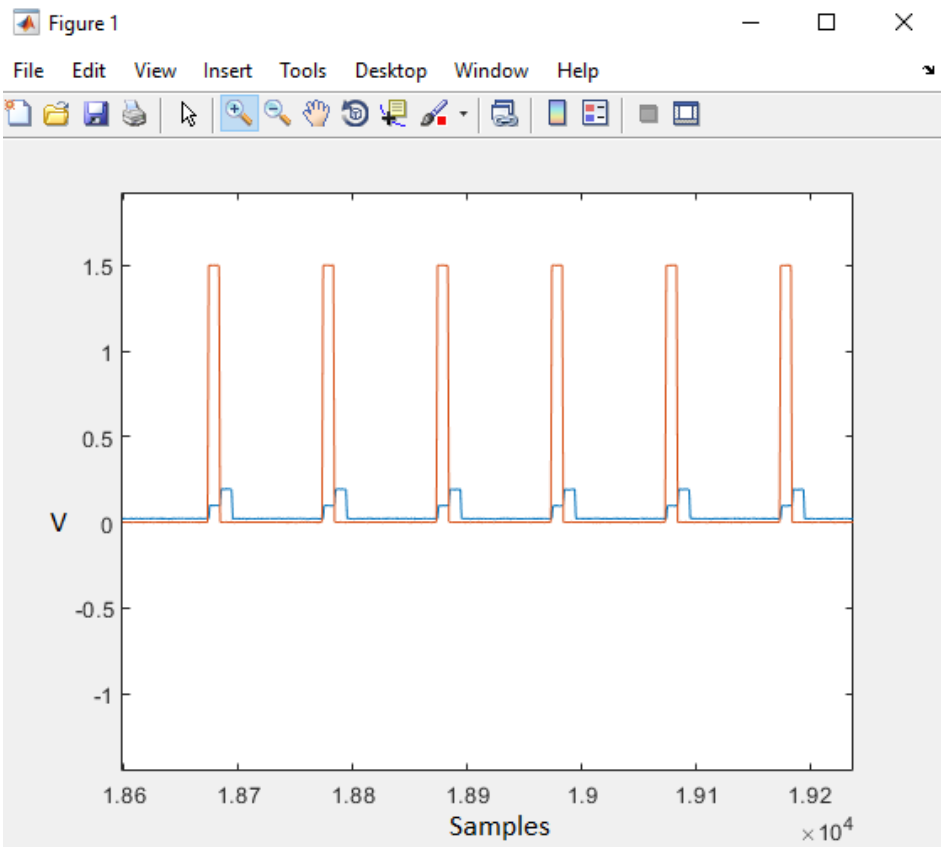

Figure 6.4: Realigned data. In orange = Voltage from channel ao0 of the DAQ, in blue = voltage from photodiode before the amplification stage

6.1.3 Microcontroller-App communication

The *Start_MICRO* button enables the USB communication with the microcontroller and permits to use the same graphs and App features just explained when the control of the system moves to the ATxmega128A1U, with the exception of the parameters on the LEDs pulses that were set in the firmware instead (see figure 6.5). An additional check is the *Connection* text field, on which three possible states can appear after pushing the Start button on the XMEGA board:

- *"Port not Found"*, in case the microcontroller is not connected with the USB cable or Matlab do not recognize the serial communication port;
- *"Acquisition Terminated"*, which is triggered by the pressing of the Button on the XMEGA board to stop the recording and means that the acquisition was successful;

- *"DATA Saved!"*, which appears automatically after the *"Acquisition Terminated"* to notify that is now possible to plot the signals of [ΔHHb] and [ΔO_2Hb] recorded.

The plots on the two graphs, the *Set ZERO POINT* and *Set MARKER* Buttons and the numeric variables calculated on the signals (like SNR or STD) that have been described in the previous section, work in this configuration as well as in the DAQ one.

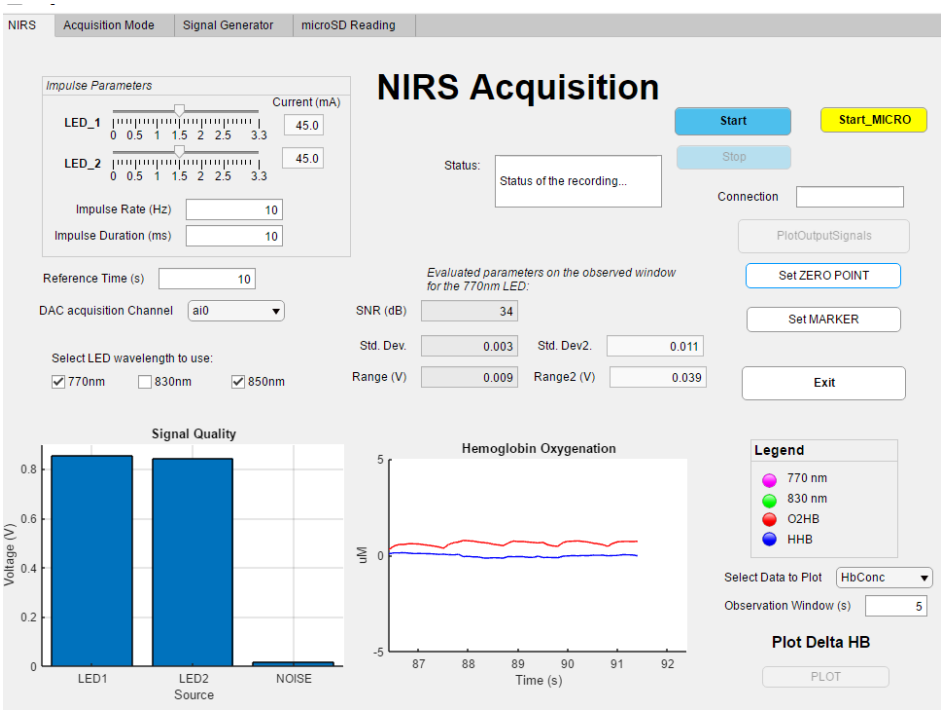

Figure 6.5: The figure refers to a USB acquisition distinguishable from a DAQ one merely for the voltage values visualized on the bar graph (due to the different gain factor, as seen in chapter 3). Moreover on the *Hemoglobin Oxygenation* graph the cardiac rhythm is visible on the [ΔO_2Hb] signal.

6.1.4 MicroSD Data Processing

Another Tab in the App has been dedicated to the microSD data reading and processing since as anticipated, the microcontroller carries out the data logger functionality where data are saved as 32 bits float numbers and needs to be read properly from the .txt file on the microSD. Figure 6.6 shows how the *microSD Reading* Tab

works: first of all, once the microSD card is inserted in the PC, the button *Open* permits to get inside the SD folder in which the .txt data file of interest is located and load it. Then, pressing the *Start* button indicated by the *Start the Data Extraction and Solve the dMBLL system* quote, the code section that takes up the reading of the data packets and separates the four 32 bits data among the ones related to LED1, LED2 and noise acquisition depending on the opportune flag, as presented in chapter 3. This process is notified with the sentence *'Extracting Data...'* in the Status field at the bottom, and at the end of the operations four MATLAB figure opens: three reporting average, maximum and minimum voltage data and standard deviation of the averaged samples for each of the cases seen above, then the forth figure appear with the plot of the [ΔHHb] and [ΔO_2Hb] signals recorded. At the end of the process the sentence *Success!* appears in the Status field if everything went right(figure 6.7).

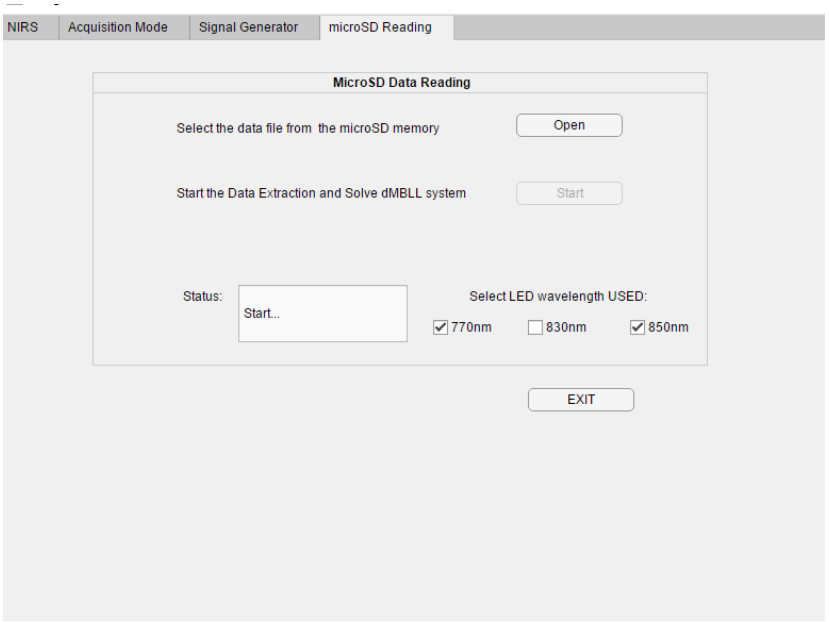

Figure 6.6: MATLAB App for reading data saved on microSD

In chapter 7 the figures showing the ΔConcentrations obtained from the USB real-time acquisition and the SD reading will be compared.

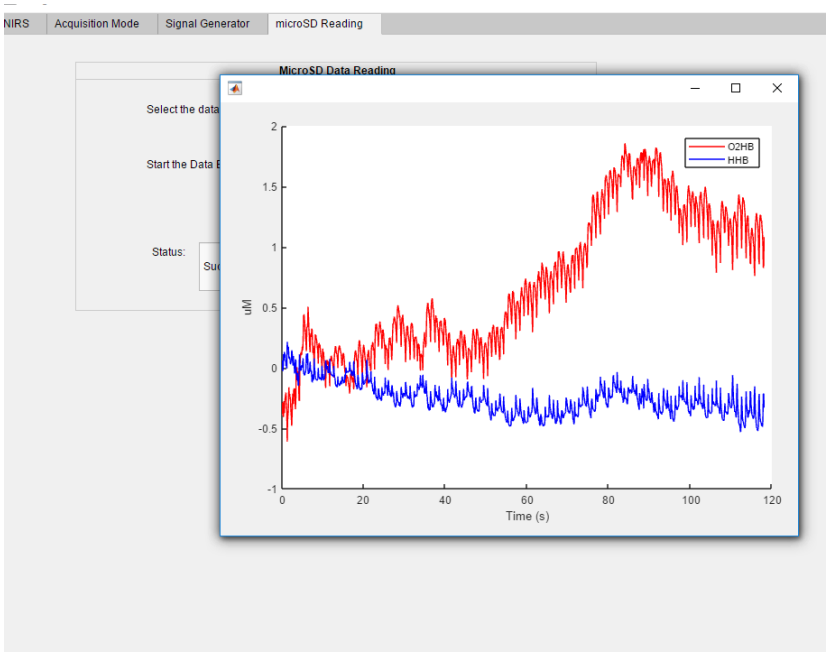

Figure 6.7: In figure the result of the *Start* button of the *microSD Reading* Tab Group reporting the hemoglobin oxygenation variations during an inspiration apnoea task (see section 7.2).

Signal Acquisition

As anticipated in the introduction of the chapter, the two generic working modes of the DAQ have been included in the App for the purpose of testing the system during the various steps of the design process and will be briefly exposed below. The *Signal Acquisition* tab permits to choose the DAQ channel from which receiving the signal, the input configuration (single ended and differential), the sampling rate and eventually the duration of the observation window. Once the *Start* button is pushed the signal is displayed in raw-mode (one sample at a time) until the window duration is reached, then the visualization starts back (figure 6.8). This *Signal Acquisition* mode was thought to work in foreground which means that Matlab can not perform other operations during the recording: it lasts for a time equal to the window duration set, then the signal is stored and displayed, but of course it is not a real-time acquisition. There is the possibility to stop the acquisition using the *Stop* button: in this case the initial configurations of sampling rate, length of the observation window and terminal configuration can be changed, as well as it is possible to investigate another channel of acquisition choosing one from the drop down box;

once the *Start* is pressed new data are plotted. The *Reset* button starts a new session of the DAQ, which is necessary because of the other applications of the GUI that typically exploit the same DAQ and would generate errors. The *Exit* button closes the app, it is common to all of the tabs.

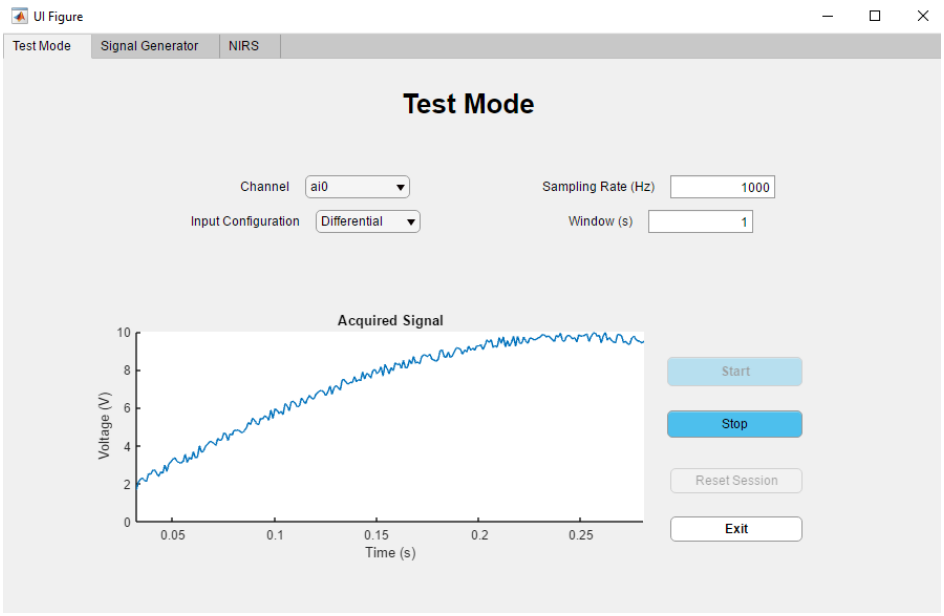

Figure 6.8: Signal Acquisition Tab group.

Signal Generator

The last Tab Group can be used to generate sine wave signal: voltage amplitude and rate can be set independently for the two output channels (in case both of them are selected) as shown in figure 6.9.

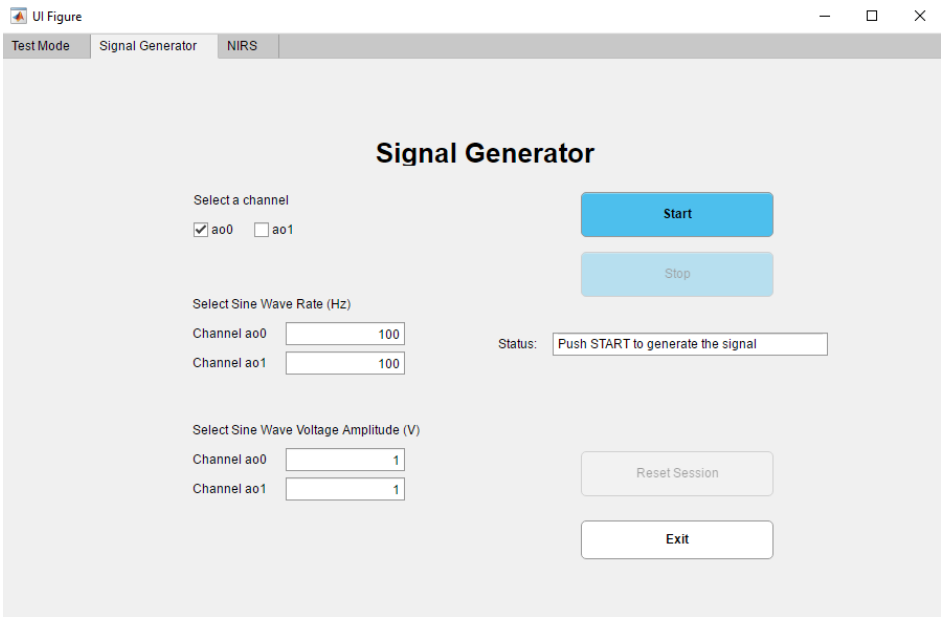

Figure 6.9: Signal Generator Mode

The *status* bar shows the ongoing process: the sentence '...Sending Data' appears once the signal generation starts as a background operation, and the *Reset* button is simultaneously enabled.

Chapter 7

Evaluation steps and Results

This last chapter will be devoted to discuss the tests made in order to pass from the NI-DAQ based system to the microcontrolled one, and will present the signals of [ΔO_2Hb] and [HHb] detected in two kind of breathing tasks to demonstrate the behaviour of the tool created in a cerebral oxygenation monitoring.

7.1 Hardware check

This section describes the controls made on the hardware components to get to the final board configuration that would be used in the microcontrolled device.

7.1.1 Photodiode choice

Once the NI-DAQ controlled hardware had been configured (see section 3.3) the three photodiodes shown in figure 7.2 were soldered on the pcb and the probes were tested to find the one that gave the better performances in terms of sensitivity and noise: not only the 50 Hz noise had to be taken into account, but also ambient light and lamps flickering which were present during the operating conditions.

Figure 7.1: LEFT: the Si-Pin s1223 series from Hamamatsu, RIGHT: the Si-Pin s5973 series from Hamamatsu

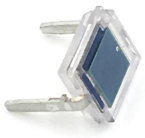

Figure 7.2: Vishay BPW34 [30].

After positioning the two probes on the forehead, the system was powered up and the output voltage from the photodiodes was checked on the oscilloscope in correspondence to the LEDs blinking, observing amplitude and potential interference: even though all of the photodiodes were equally influenced by the flickering noise, the Si-Pin s1223 series and s5973 series from Hamamatsu showed the worst performances when sited on the forehead, as they were more affected by a noisy capacitive coupling due to the bigger metal case; moreover the last one revealed also lower values of voltage amplitude probably because of the smaller active surface of the sensor. Eventually, considering the better behaviour, the Vishay BPW34 was chosen as light detector of the device.

7.1.2 Current input and Voltage output

The second check was then made on the definitive hardware configuration, and consisted in controlling that the value of current passing through the LEDs complied with the value theoretically calculated of about 45 mA (see section 3.2.1), and that the voltage received by the photodiode in correspondence of the LEDs blinking, after the amplification, maintained a satisfying amplitude with respect to noise level, without introduction of other interference sources. Both the first and the second questions had a positive outcome after visualizing the same signals of interest on the oscilloscope and on the App interface (figure 7.3b) which helped in determin-

ing more accurately the level of noise present. Eventually, from an electrical point of view, it was assured that everything worked fine. Moreover, these evidences meant that the probes holder could not only guarantee a mechanical stability, but was also steady enough to reach a good SNR shielding from ambient light and from lateral crosstalk of the LEDs pulses.

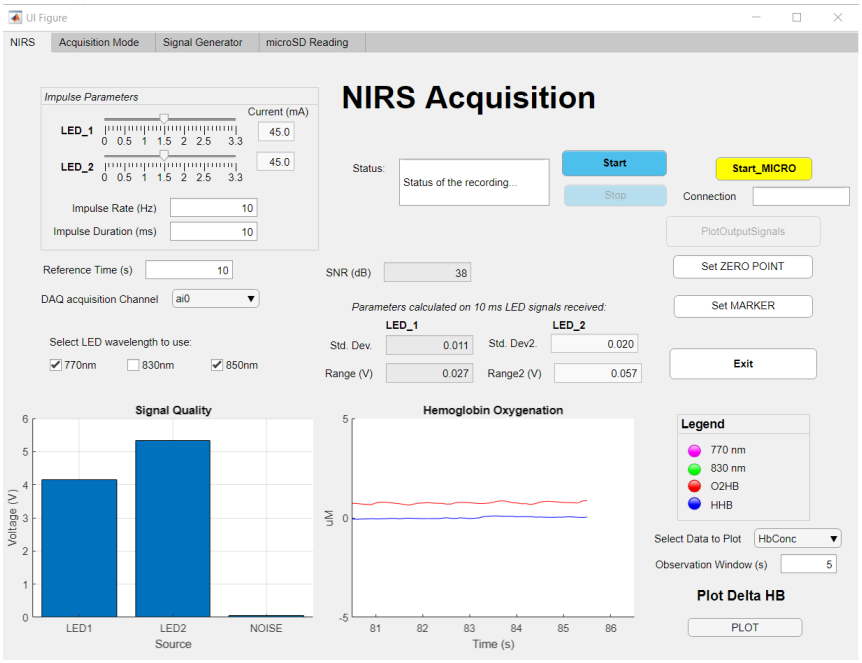

(a)

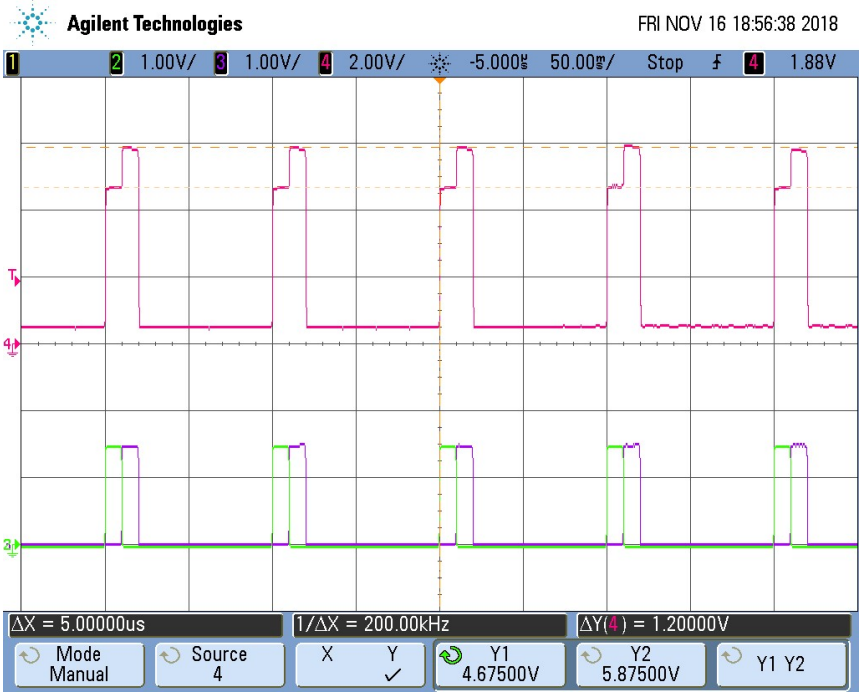

(b)

Figure 7.3: (a) The bar graph of tha app, corresponding to the oscilloscope screen, with the output voltage due to LEDs blinking compared to noise level (SNR = 38 dB) (b) Oscilloscope screen showing the DAC voltage pulses (GREEN= LED1, PURPLE = LED2) = 1.5 V (offset = 3 V), and in RED the correspondent response from the photodiode, after amplification: 4.68 V and 5.88 V respectively due to LED1 and LED2 blinking.

7.2 Physiological testing on NI-DAQ system

Once all the electrical functioning had been checked, the successive step had the objective to confirm that the time-resolved method implemented was actually informative from a biological point of view: in other words, the signals of [ΔO_2Hb] and [HHb] observed had to recover the expected biological trend in determinate conditions.

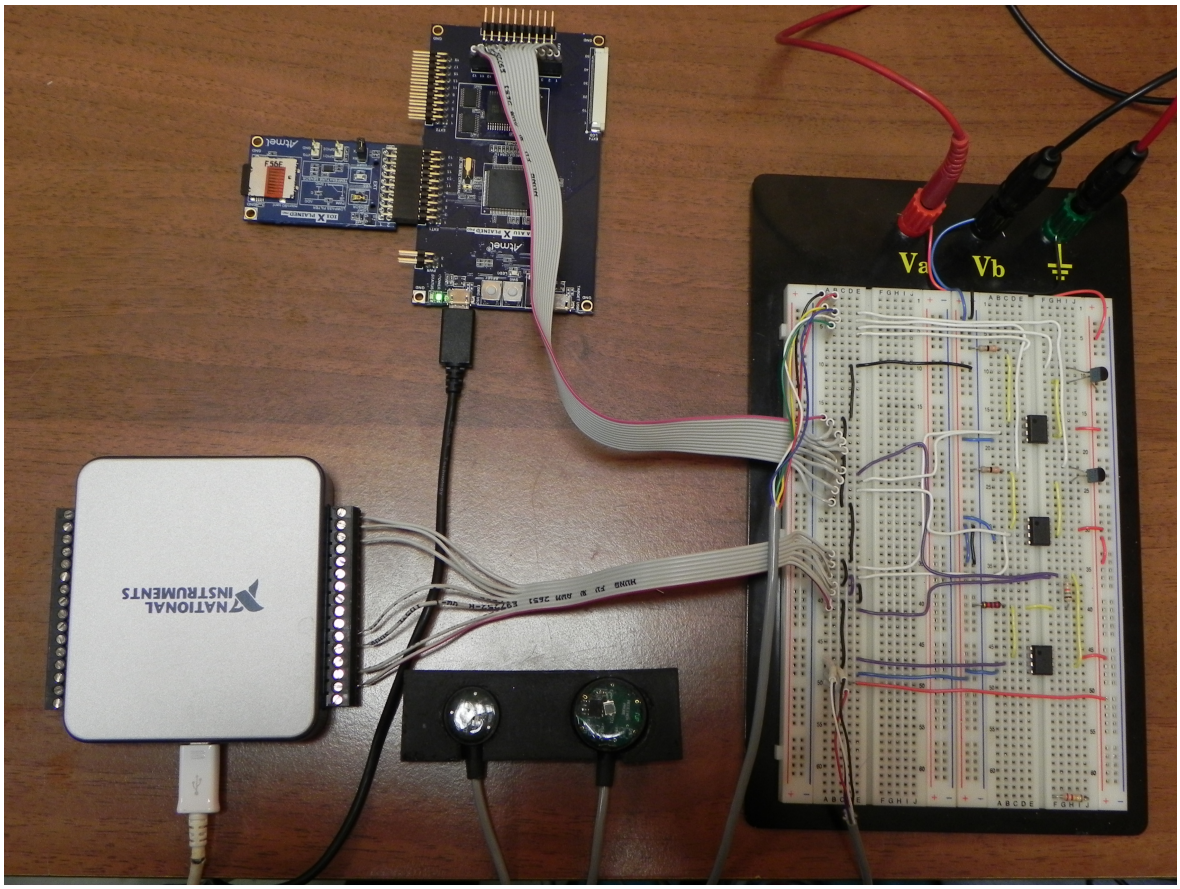

Figure 7.4: The figure shows the probes, the two control units and the mainboard of the system with the final board design.

Since the variations of the chromophores at a cerebral level are always limited to small ranges, before evaluating the sensitivity of the system to these little changes, a test of muscular contraction was made. Even though the system was not optimized for this use, since the DPF selected was relative to the cerebral tissue, this experiment could give at least the certainty that the solution of the Lambert-Beer equation was giving the expected results. In a muscular contraction a relevant increment of [HHb]

and decrement of [ΔO_2Hb] is expected, due to the vasoconstriction that the muscle apply on vessels.

The probes were put in the middle of the right shank, just beside the tibia, and the contraction was executed rising the right foot while the left was opposing to the movement, in order to get the maximal activation and minimal motion artifacts. In figure 7.5 the result is shown: both at the beginning and at the end of the event, it is evident that the variation of the two concentrations follows the desired behaviour (note: in all the figures of the chapter the dotted lines represent starting and ending point of the event of interest). After this test, it was at least proved that the system was giving the proper physiological feedback.

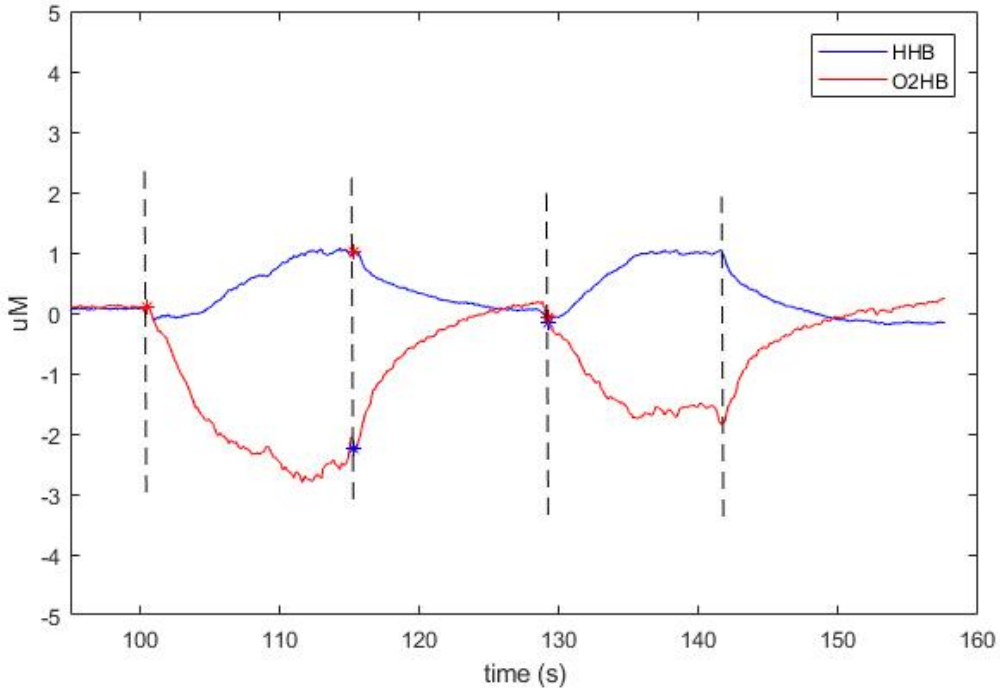

Figure 7.5: Signal of [HHb] and [ΔO_2Hb] in the contraction of the tibial muscle. As expected oxygenated hemoglobin decreases while deoxygenated increases.

At this point the cerebral response was investigated to find out whether a concrete usefulness of the system in the cerebral autoregulation monitoring had been obtained or not. Three types of tasks were used to reach this goal:

1. Inspiratory apnoea;

2. Expiratory apnoea;

3. Hyperventilation.

In the first two cases an increase in [O_2Hb] and a reduction in [HHb] is expected while in the third case the opposite situation should happen as the vessels vasoconstrict due to higher values of O_2Hb in the blood. At the beginning of each test the best positioning of the holder was found checking the bar plot on the App: usually in the lowest noise condition, the heartbeat artifact became evident on the [ΔO_2Hb] plot as a rhythmical sine-wave like behaviour due to the arterial pulsing under the temple (see figure 7.3a). However this artifact could be easily removed later with a low-pass filter at 500 mHz; a typical placement of the probes is shown in figure 4.7 of chapter 6.
The three tasks have been performed by a female non-smoker subject of 24 years in good healthy conditions. In the inspiratory apnoea experiment, the subject was asked to breath normally for 20 seconds for revealing the initial oxygenation condition, then a marker has been set at the beginning of the apnoea (the asterisk in figure 7.6): it was particularly evident how the value of oxygenated hemoglobin increased while the deoxygenated decreased after a few seconds due to the autoregulation mechanism. The end of the event, signaled once again by the dotted line, correspond to the peak of the signals. Anyhow this test lasted enough to get the desired biological feedback, but typically the system should be kept acquiring for more time to see the signals getting back to the base line, as the biological responses are always slow ones.

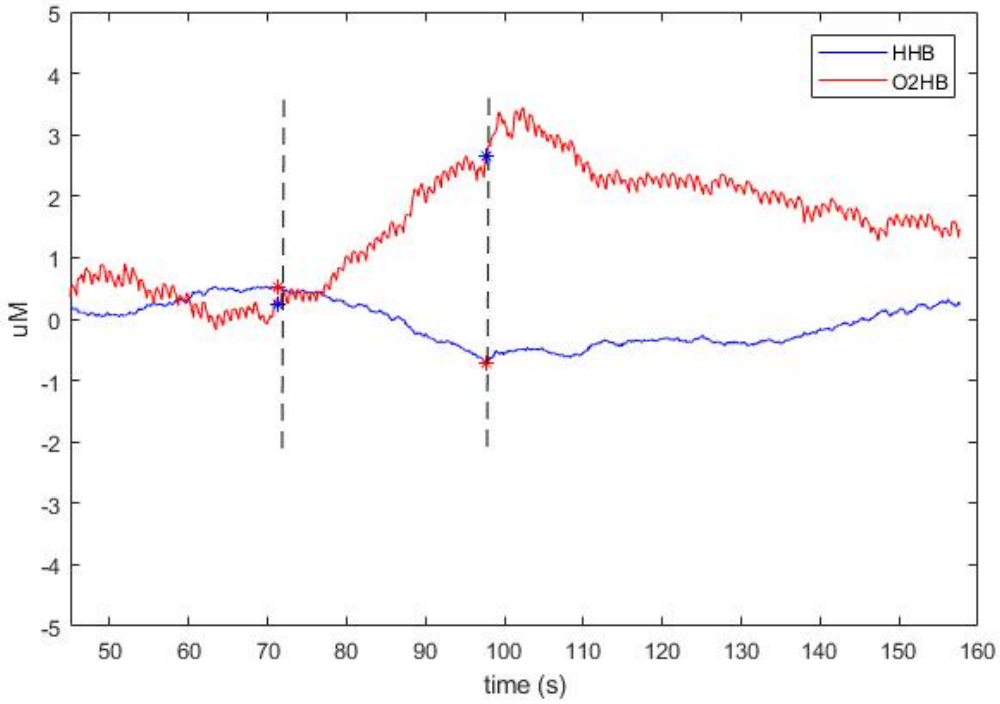

Figure 7.6: Inspiratory Apnoea Task. The cardiac rhythm is very evident on the [O_2Hb] signal due to the positioning of the holder.

Figure 7.7 shows the results obtained performing the second task, an expiratory apnoea. In this case a zero point was set just before the event started to be sure that the variations recorded were the biggest achievable. The desired behaviour of the two signal is clearly visible in figure, even though the decrease in [HHb] is less evident; however usually it is easier to observe variations in oxygenated hemoglobin than in the de-oxygenated. In this graph it is also more visible the successive return towards the zero point.

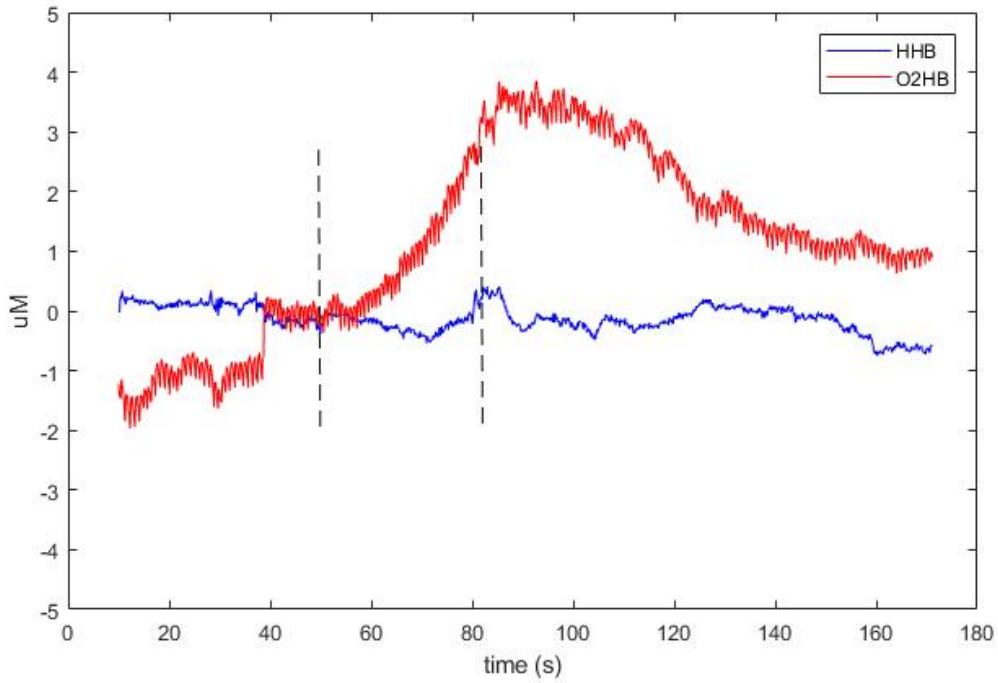

Figure 7.7: Expiratory Apnoea Task: relevant Δconcentrations were found; the subject reported having difficulties in maintaining the apnoea condition.

The hyperventilation task is then presented in figure 7.8: the behaviour is the expected one, moreover at the end of the event, when the subject felt the need of breathing normally, a notable increment of [O_2Hb] is visible, probably because a mechanism of re-assessing of normal oxygenation condition started. In this test the recording lasted enough to see the signals getting back towards the zero line.

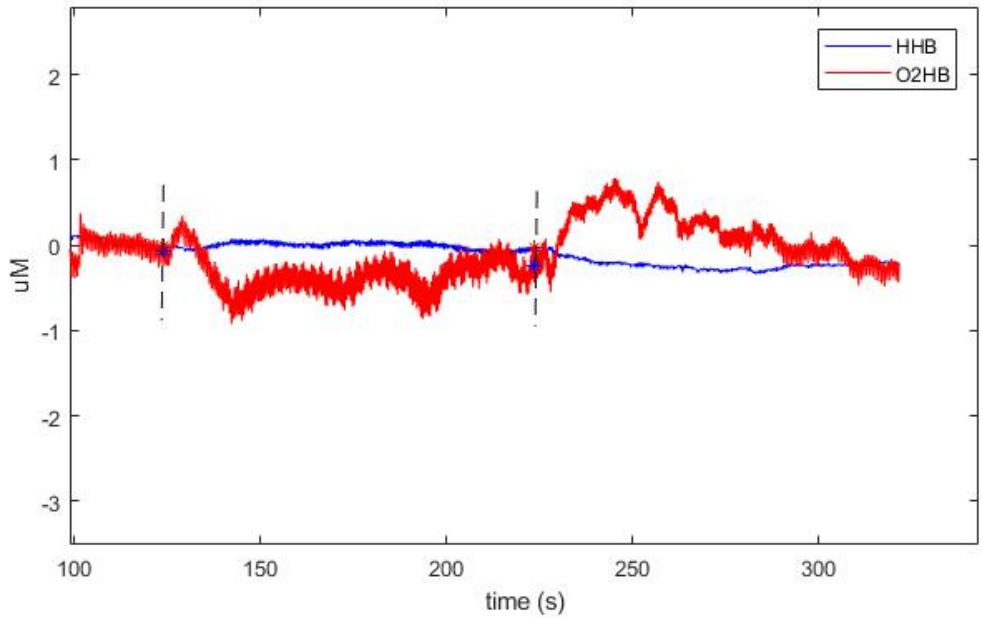

Figure 7.8: Hyperventilation Task. The cardiac rhythm is very evident on the [O_2Hb] signal and the subject reported an increment of the heartbeat when started to feel dizziness.

These tests gave the reasonable certainty that the NIRS system developed with the NI-DAQ was monitoring cerebral autoregulation in a proper way, so the control logic was moved to the ATxmega128A1U implementing the already described code (chapter 3).

7.3 Physiological check on Microcontrolled system

The physiological reliability of the final microcontrolled system was checked repeating the same tests made with the NI-DAQ: firstly the response to a muscle contraction was recorded and plotted, obtaining once again a positive outcome and demonstrating that everything was working as hoped (figure 7.9b).

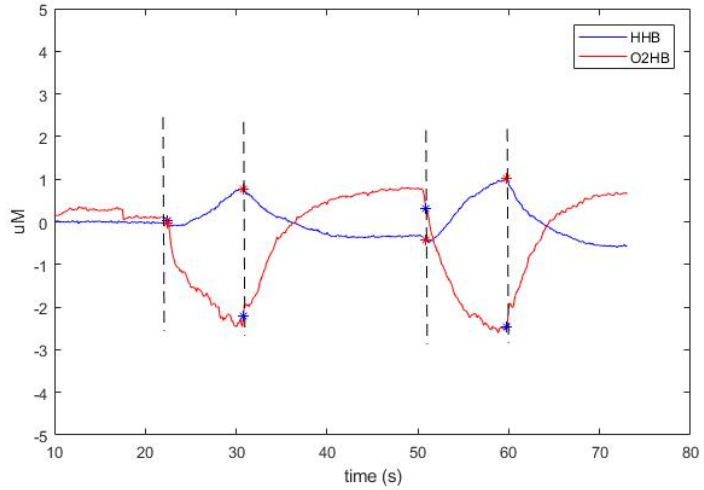

(a)

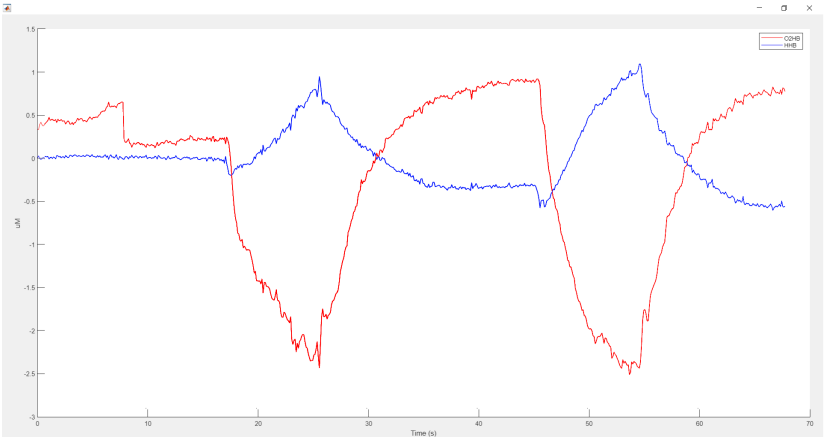

(b)

Figure 7.9: (a) The plot shows the results for a tibial muscle contraction with the microcontrolled system, the dotted lines represent the beginning and the end of the acquisition (b) The result of the SD data stored in the same test.

Secondly, the three tasks explained above have been performed with the same subject, to test if the signals trend was similar to the one obtained with the NI-DAQ controlled version of the system, and to be sure also that the SD and the USB software processing of the data was giving the same final output in terms of ΔConcentrations (figure 7.13). Below the results for each test are presented: the respective discussions are almost the same as before, since the system provided the expected behaviour in a range of uM comparable with the range found with the DAQ designed system.

Just like in the first case, to make the graphs of immediate impact, the recordings with the microcontroller focused on the physiological response right in correspondence of the execution of the task, so the return of the signals to the zero point is not always present.

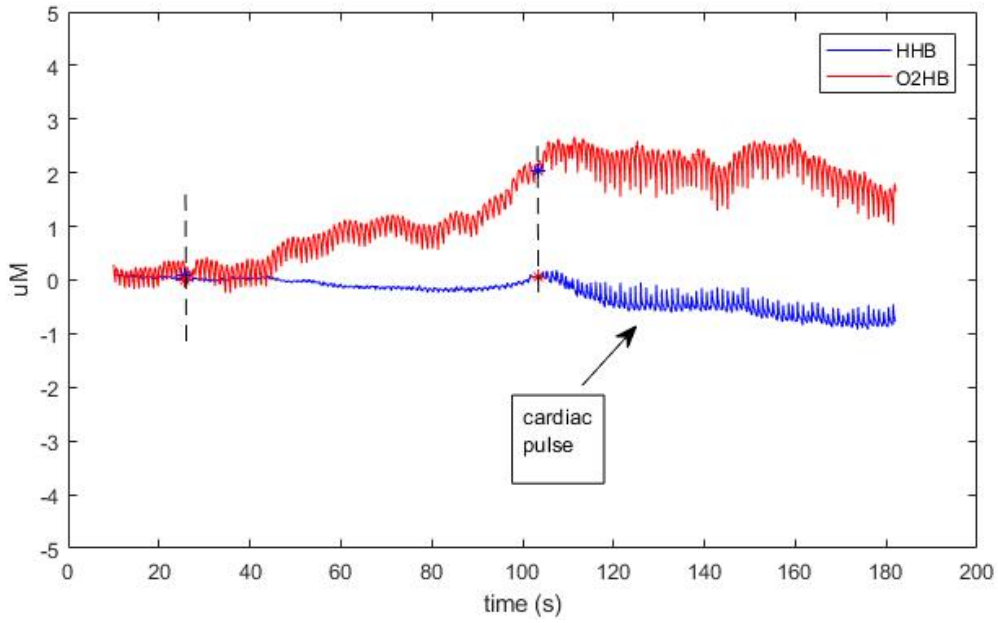

Figure 7.10: The plot shows the results for inspiratory apnoea recorded with the microcontroller.

It is interesting that in the inspiratory apnoea (figure 7.10) at the end of the event is particularly evident the cardiac cycle on both the signals: the subject reported then the difficulty faced to keep the apnoea as longer as possible so this artifact is due to the pulsing a the blood vessel under the holder, which was kept on the forehead with an elastic strip.

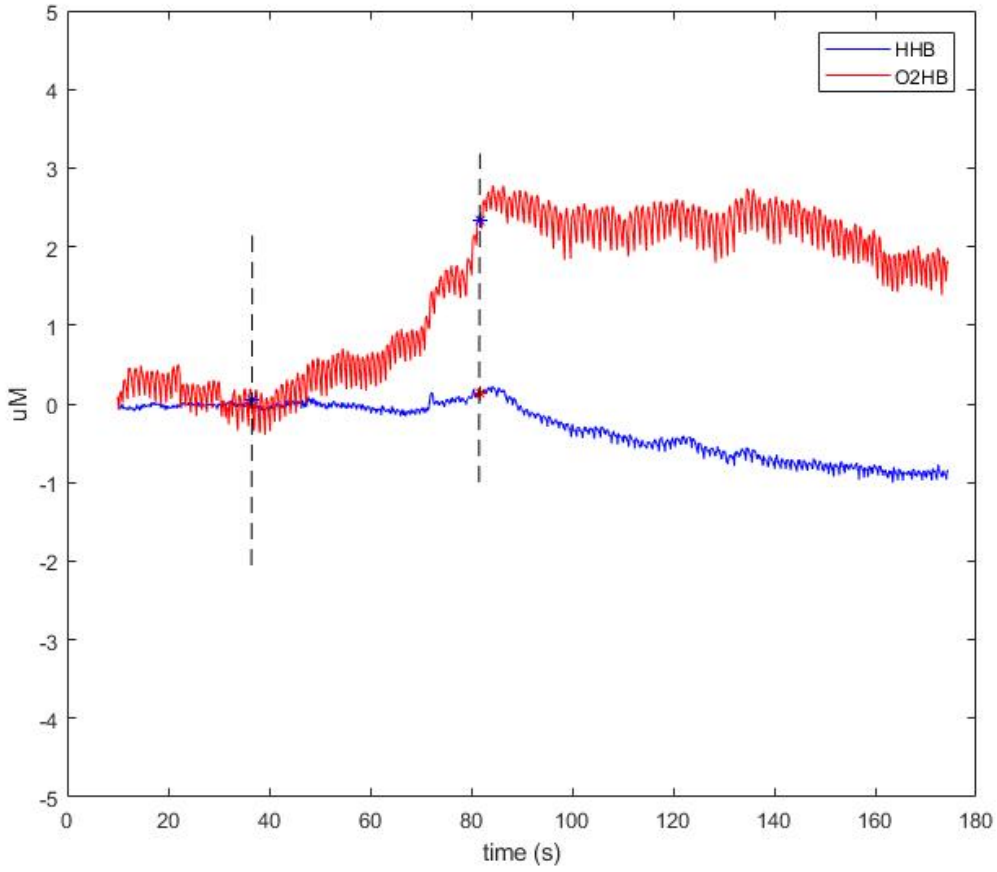

Figure 7.11: The graph represents the results for expiratory apnoea recorded with the microcontroller. The decrease in [HHb] was delayed in this case.

In the hyperventilation task instead there is a sort of spike before the end of the event: that is the point in which the subject felt a more accentuated beat of the heart. Except from this condition, the behaviour of the signals is the expected one (figure 7.12).

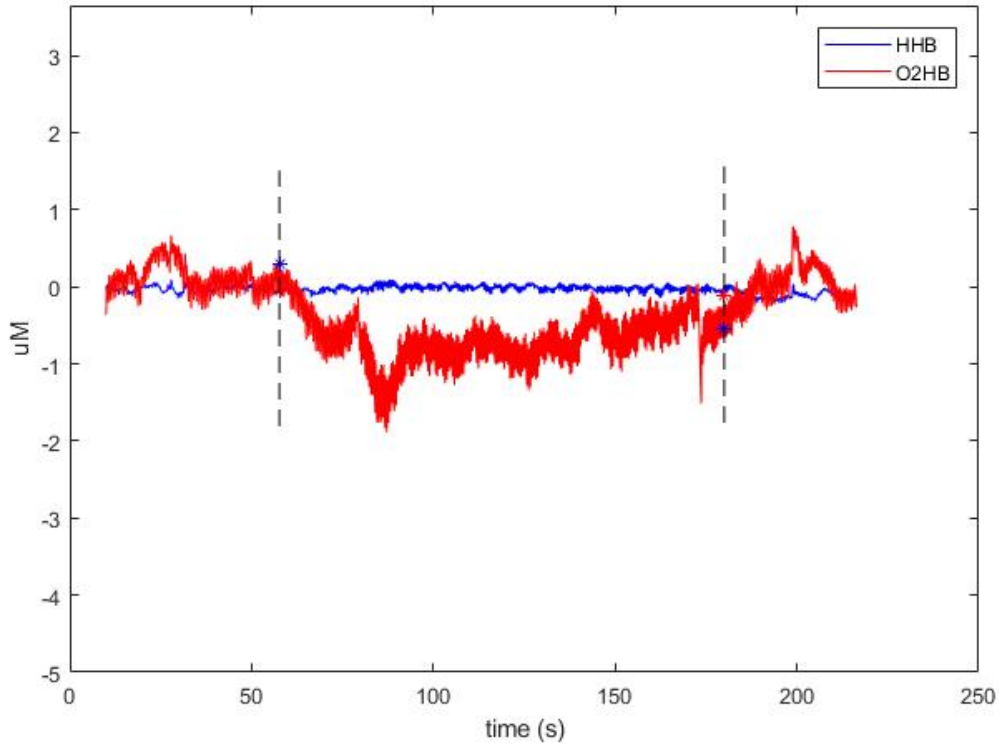

Figure 7.12: In figure the results for the hyperventilation task recorded with the microcontroller are reported. The return of the signals to the base line was particularly rapid in this case.

Figure 7.13 was helpful to confirm that the data saved on the SD and their successive processing reflected the USB real-time elaboration with the App; to plot the data together an offset of 3 μM was applied to the USB-obtained signals. At last, the tests outcome was considered satisfying enough to assert that the NIRS system designed was responding as it could be expected from a physiologically informative tool.

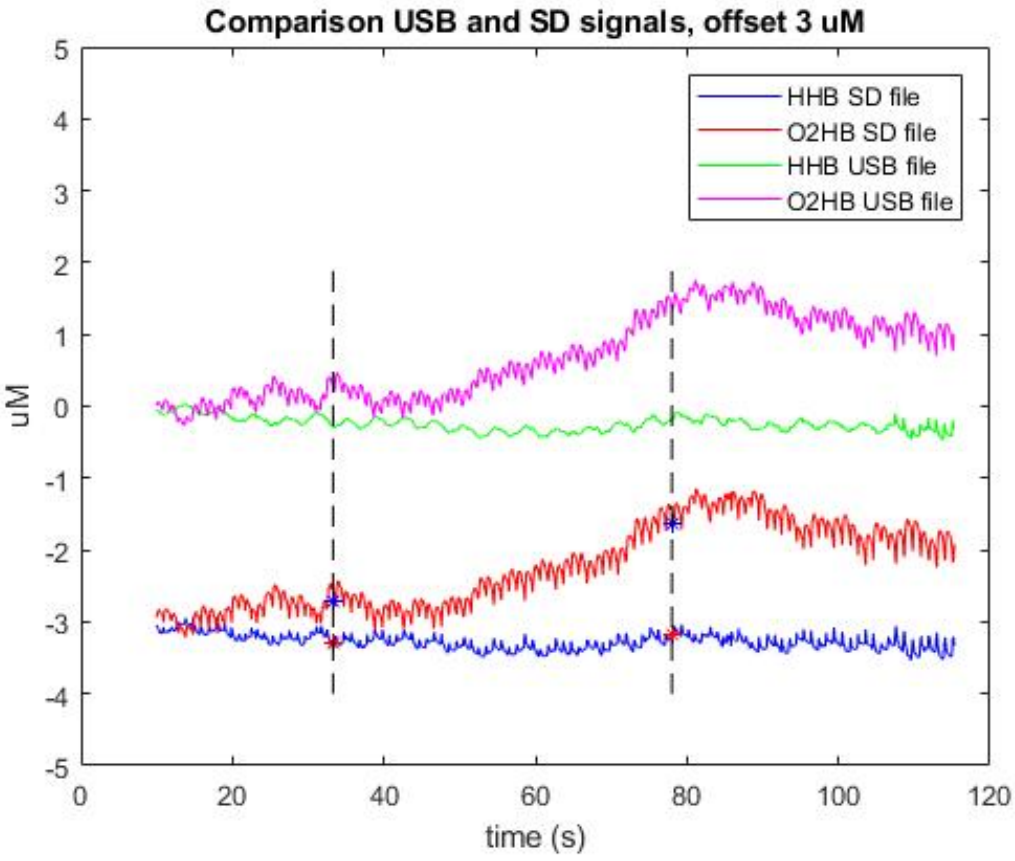

Figure 7.13: The figure shows the comparison between the SD elaborated data and the USB real-time processed ones. The task performed was an expiratory apnoea.

7.4 Limitations and critical features

7.4.1 Crosstalk and Positioning

The reason why the LEDs wavelengths chosen for a NIRS acquisitions needs to be the farthest possible is clearly explained in figure 7.14: here 830 nm and 850 nm LEDs were adopted and the signals obtained are specular one to the other, as the absorbance both of HHb and O_2Hb in this range is very similar for one wavelength and for the other. In the shown plot, an apnoea task was performed starting from the red and blue asterisks visible on the plot, and the two behaviours are almost completely the same, but opposite; moreover also the motion artifacts present at the beginning of the graph seem to be mirrored. To reduce at minimum crosstalk the

770 nm and 850 nm were then used.

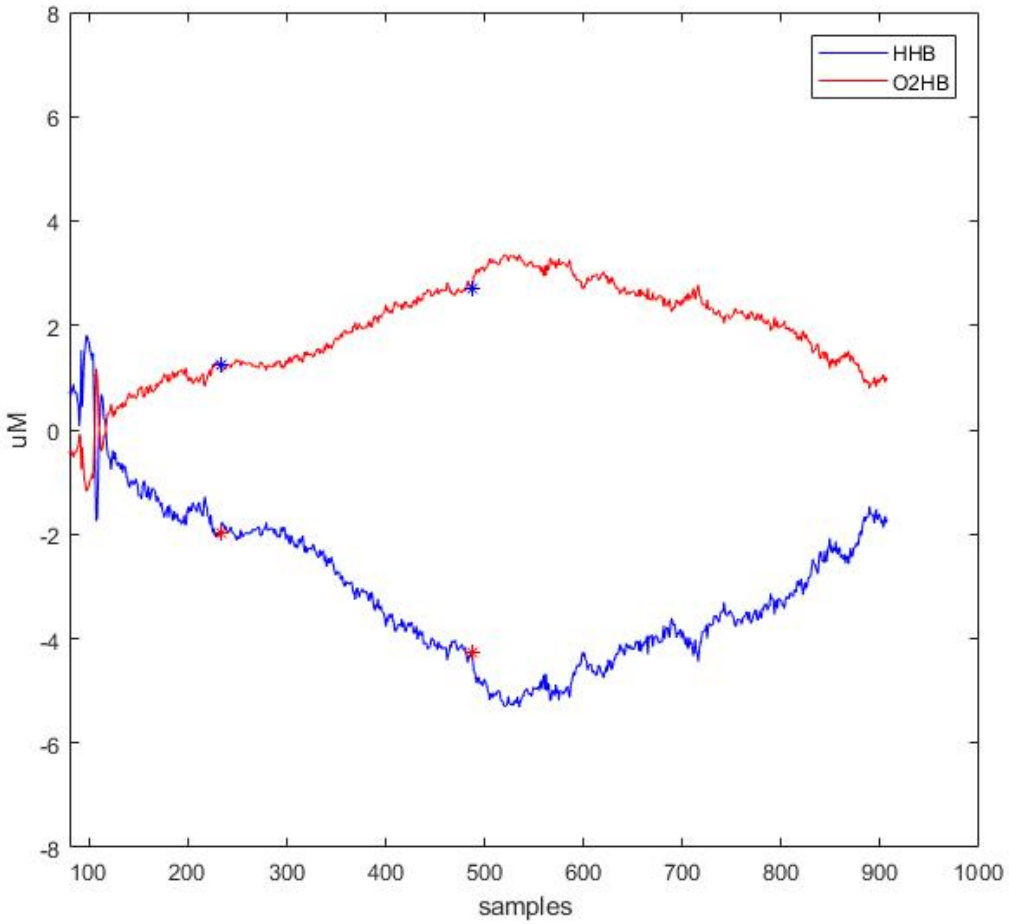

Figure 7.14: The figure shows the problem of crosstalk when adopting 830 nm and 850 nm as LEDs: as visible the behaviour of the signals seems to be mirrored, obtaining a non physiological response to the apnoea task.

Another problem noticed during the use of the NIRS system designed concerns the probes positioning with the double-sided tape: it ruined the flexible holder after a certain number of recordings, so it was preferred to adopt a strip to keep the holder on the forehead (figure 7.15). In future it would be worth trying to change the structure of this element using a little more rigid plastic, thus not affected by the tape employment, and at the same time increasing the hollow in the middle of the holder to contrast the stiffness of the new model.

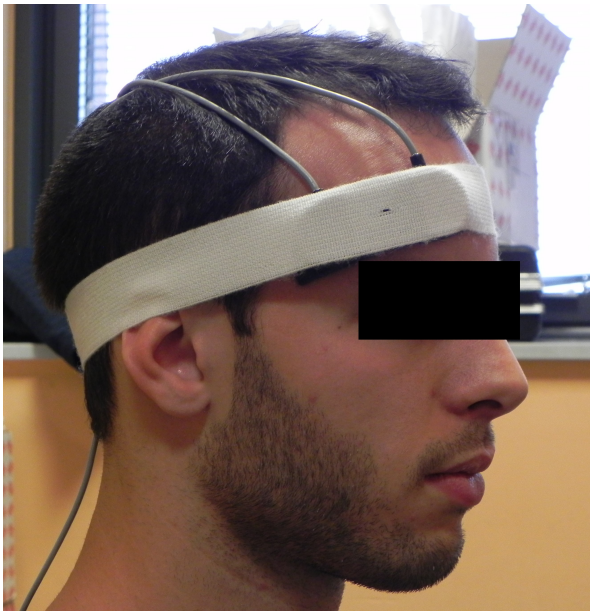

Figure 7.15: Positioning with Velcro strip

7.5 Final Steps and Conclusions

The final device developed could be improved in the future by adding one more channel in order to record at the same time from one hemisphere and the other, as there is an high variability in their responses to the stimuli and possible differences in intensity of the signals recorded from each one. Also the solution of the Lambert-Beer equations for the cytochrome-c-oxidase could be added, for making the system more informative from a biological point of view, and moreover a step of verification should be carried out with a commercial device to prove definitely the reliability of the NIRS device realized. Once this will be done, it could be finally possible to think about making the prototype a stand-alone device: the discussion on the autonomy desired is now introduced to demonstrate that with the configuration tested, transforming the device into a battery powered would be feasible. The consumption of the LEDs can be calculated in this way:

$$Q_{LED\_10ms} = I \cdot \Delta T = 0.045 \cdot 0.01 = 450\mu C \tag{7.1}$$

and considering the blinking frequency of 10 Hz, in one hour the consumption is of:

$$Q_{2LED\_1h} = Q_{LED\_10ms} \cdot 36000 \cdot 2 = 32.4C \tag{7.2}$$

The Q_{LED_10ms} has been multiplied for two to take into account two LEDs. The maximum of the microcontroller consumption is of a few hundreds of mW so:

$$Q_{microcontroller} = \frac{P}{V_{cc}} \cdot \Delta T = \frac{0.250}{3.3} \cdot 3600 = 272C \tag{7.3}$$

The final autonomy using a 3.7 V battery of 1.5 Ah is of about:

$$Autonomy = \frac{1.5 * 3600}{305} = 17h \tag{7.4}$$

This amount of hours without the need of recharging the device is a satisfying duration considering that NIRS recordings usually last for 30 minutes at most. With a battery of 3.7 V the $\pm$ 12 V to power the photodiode can be obtained for example using two capacitive DC-DC converters, but the circuitry may also be changed in order to be able to power it at 3.7 V, and this may be the optimal choice since the DC-DC converters are less efficient when not exploited at their maximum power.
Eventually, the NIRS system designed in this thesis for cerebral oxygenation monitoring has been proved to work fine with extremely low cost hardware components and a simple type of time-resolved approach, so, even if some steps still need to be carried out, the resulting prototype is considered compliant with the specification thought at the beginning.

Bibliography

[1] R Boushel, Henning Langberg, and Olesen. "Monitoring tissue oxygen availability with near infrared spectroscopy (NIRS) in health and disease". In: *Scandinavian journal of medicine & science in sports* 11.4 (2001), pp. 213–222.

[2] H-PF Brecht et al. "Accurate, noninvasive measurement of total hemoglobin concentration with optoacoustic technique". In: *Engineering in Medicine and Biology Society, 2004. IEMBS'04. 26th Annual International Conference of the IEEE*. Vol. 1. IEEE. 2004, pp. 375–376.

[3] Britton Chance et al. "Phase modulation system for dual wavelength difference spectroscopy of hemoglobin deoxygenation in tissues". In: *Time-Resolved Laser Spectroscopy in Biochemistry II*. Vol. 1204. International Society for Optics and Photonics. 1990, pp. 481–492.

[4] David T Delpy et al. "Estimation of optical pathlength through tissue from direct time of flight measurement". In: *Physics in Medicine & Biology* 33.12 (1988), p. 1433.

[5] DT Delpy et al. "Quantitation of pathlength in optical spectroscopy". In: *Oxygen Transport to Tissue XI*. Springer, 1989, pp. 41–46.

[6] Dental-Science. *Nerve supply of pterygopalatine fossa*. 2018. URL: `http://www.dental-science.com/pterygopalatine-fossa-anatomy-arterial-supply-venous-drainage-nerve-supply-radiology/`.

[7] Doctorlib.info. *Physiology review*. 2017. URL: `https://doctorlib.info/physiology/review/38.html`.

[8] John C Drummond, Roland R Lee, and James P Howell Jr. "Focal cerebral ischemia after surgery in the "beach chair" position: the role of a congenital variation of circle of Willis anatomy". In: *Anesthesia & Analgesia* 114.6 (2012), pp. 1301–1304.

[9] Arlene Duncan et al. "Measurement of cranial optical path length as a function of age using phase resolved near infrared spectroscopy". In: *Pediatric research* 39.5 (1996), p. 889.

[10] Sergio Fantini et al. "Frequency-domain multichannel optical detector for non-invasive tissue spectroscopy and oximetry". In: *Optical engineering* 34.1 (1995), pp. 32–43.

[11] Yoko Hoshi. "Functional near-infrared optical imaging: Utility and limitations in human brain mapping". In: *Psychophysiology* 40.4 (2003), pp. 511–520.

[12] Frans F Jobsis. "Noninvasive, infrared monitoring of cerebral and myocardial oxygen sufficiency and circulatory parameters". In: *Science* 198.4323 (1977), pp. 1264–1267.

[13] Jeremy Kam. *Raised intracranial pressure*. 2015. URL: `http://slideplayer.com/slide/5762836/`.

[14] Walt Kester et al. "Sensor signal conditioning". In: *Sensor Technology Handbook* (1999), pp. 31–136.

[15] Christina Kolyva et al. "Cytochrome c oxidase response to changes in cerebral oxygen delivery in the adult brain shows higher brain-specificity than haemoglobin". In: *Neuroimage* 85 (2014), pp. 234–244.

[16] P Lin, J Jovicich, and S Robinson. "CBF-CMRO2 Coupling in the Default Mode Network". In: *Proc. Intl. Soc. Mag. Reson. Med*. Vol. 17. 2009, p. 216.

[17] Jia-Ming Liu. *Photonic devices*. Cambridge University Press, 2009.

[18] *Low Power, Low Noise Precision FET Op Amp*. Analog Devices, 2009. URL: `https://www.analog.com/media/en/technical-documentation/data-sheets/AD795.pdf`.

[19] Judith H Meek et al. “Regional hemodynamic responses to visual stimulation in awake infants”. In: *Pediatric Research* 43.6 (1998), p. 840.

[20] John D Michenfelder and Richard A Theye. “Cerebral protection by thiopental during hypoxia”. In: *Anesthesiology* 39.5 (1973), pp. 510–517.

[21] Bahram Mokri. “The Monro–Kellie hypothesis applications in CSF volume depletion”. In: *Neurology* 56.12 (2001), pp. 1746–1748.

[22] Luis Orozco. “Optimizing Precision Photodiode Sensor Circuit Design”. In: *Application note MS-2624* (2014), pp. 1–5.

[23] Adelina Pellicer and del Carmen Bravo. “Near-infrared spectroscopy: a methodology-focused review”. In: *Seminars in fetal and neonatal medicine*. Vol. 16. 1. Elsevier. 2011, pp. 42–49.

[24] Planar diffused silicon Photodiode. *Photodiode Characteristics and Applications*.

[25] Hamamatsu Photonics. *Opto-semiconductor handbook-Chapter 02 Si photodiodes*.

[26] O-MH Richter and B Ludwig. “Cytochrome c oxidase—structure, function, and physiology of a redox-driven molecular machine”. In: *Reviews of physiology, biochemistry and pharmacology*. Springer, 2003, pp. 47–74.

[27] Peter Safar. “Cerebral resuscitation after cardiac arrest: a review.” In: *Circulation* 74.6 Pt 2 (1986), pp. IV138–53.

[28] Mohamad Sawan, Muhammad T Salam, and Le Lan. “Wireless recording systems: from noninvasive EEG-NIRS to invasive EEG devices”. In: *IEEE transactions on biomedical circuits and systems* 7.2 (2013), pp. 186–195.

[29] Felix Scholkmann et al. “A review on continuous wave functional near-infrared spectroscopy and imaging instrumentation and methodology”. In: *Neuroimage* 85 (2014), pp. 6–27.

[30] Vishay Semiconductors. “Silicon PIN Photodiode”. In: *BPW34, BPW34s, http://www.vishay. com/docs/81521/bpw34. pdf* (2012).

[31] Emily Shardlow and Alan Jackson. “Cerebral blood flow and intracranial pressure”. In: *Anaesthesia & Intensive Care Medicine* 12.5 (2011), pp. 220–223.

[32] Scott Prahl Steve Jacques. *Tabulated Molar Extinction Coefficient for Hemoglobin in Water*. 2018. URL: https://omlc.org/spectra/hemoglobin/summary.html.

[33] Gary Strangman et al. "Near-infrared spectroscopy and imaging for investigating stroke rehabilitation: test-retest reliability and review of the literature". In: *Archives of physical medicine and rehabilitation* 87.12 (2006), pp. 12–19.

[34] Alifia Tameem and Hari Krovvidi. "Cerebral physiology". In: *Continuing Education in Anaesthesia, Critical Care & Pain* 13.4 (2013), pp. 113–118.

[35] Arno Villringer et al. "Near infrared spectroscopy (NIRS): a new tool to study hemodynamic changes during activation of brain function in human adults". In: *Neuroscience letters* 154.1-2 (1993), pp. 101–104.

[36] Wanda Webb and Richard K Adler. *Neurology for the Speech-Language Pathologist-E-Book*. Elsevier Health Sciences, 2016.

[37] Martin Wolf, Marco Ferrari, and Valentina Quaresima. "Progress of near-infrared spectroscopy and topography for brain and muscle clinical applications". In: *Journal of biomedical optics* 12.6 (2007), p. 062104.